

# Mapping of topological properties of photonic lattices

---

Jajtić, Ema

Doctoral thesis / Disertacija

2022

Degree Grantor / Ustanova koja je dodijelila akademski / stručni stupanj: **University of Zagreb, Faculty of Science / Sveučilište u Zagrebu, Prirodoslovno-matematički fakultet**

Permanent link / Trajna poveznica: <https://um.nsk.hr/um:nbn:hr:217:558229>

Rights / Prava: [In copyright](#)/[Zaštićeno autorskim pravom.](#)

Download date / Datum preuzimanja: **2024-07-17**



Repository / Repozitorij:

[Repository of the Faculty of Science - University of Zagreb](#)





University of Zagreb

Faculty of Science  
Department of Physics

Ema Jajtić

# **MAPPING OF TOPOLOGICAL PROPERTIES OF PHOTONIC LATTICES**

DOCTORAL DISSERTATION

Zagreb, 2022.





University of Zagreb

Faculty of Science  
Department of Physics

Ema Jajtić

# **MAPPING OF TOPOLOGICAL PROPERTIES OF PHOTONIC LATTICES**

DOCTORAL DISSERTATION

Supervisor:  
prof. dr. sc. Hrvoje Buljan

Zagreb, 2022.





Sveučilište u Zagrebu

Prirodoslovno-matematički fakultet

Fizički odsjek

Ema Jajtić

**MAPIRANJE TOPOLOŠKIH SVOJSTAVA  
FOTONIČKIH REŠETKI**

DOKTORSKI RAD

Mentor:

prof. dr. sc. Hrvoje Buljan

Zagreb, 2022.



# Acknowledgements

Nature is full of wonders waiting to be discovered. To do it through the eyes of a physicist was a joy, one best experienced with others. I would like to thank my supervisor and mentor Hrvoje for joining me, and guiding me, on the path of discovery, and for his unwavering support in this little thing called life. Our path has led us from one side of the globe, where I thank Dario, Frane and Robert, to the other, where my gratitude lies with Shiqi, Xiujing and Zhigang. It was not only a road to discovery in physics, but also one of personal growth. Friends have carried me on this road when times were tough, and rejoiced with me when the times were good. For that I would like to thank them; Subhadip, Ali, Indranil, Bidisha, roommate Ana, office roommate Ana, Petar, Petra, Marija, Marcel and Iva. I would also like to thank my family; my sister Kristina and my mom and dad, Zdenka and Mirko, for being there for me when I needed it most. Thank you.

*This research is supported by the QuantiXLie Center of Excellence, a project co-financed by the Croatian Government and the European Union through the European Regional Development Fund - the Competitiveness and Cohesion Operational Programme (Grant KK.01.1.1.01.0004).*



# Abstract

**Keywords:** *topology, topological photonics, photonic lattices, topological insulators, higher-order topological insulators, bound states in continuum, Berry phase, Zak phase, Berry phase winding, Chern number, polarization, Dirac points, pseudospin, nonlinearity*

The study of topological properties of materials started in solid-state systems and was soon expanded to photonic systems. Today, topological photonics is one of the hottest areas of research in physics. In this thesis, we study topological properties and their mappings in photonic lattices.

In the first part of this thesis, we study the mapping of topological singularities from the momentum space to the real space. For this, we employ 2D photonic honeycomb and Lieb lattices that have topological singularities in the momentum space in the form of Dirac points. We show that the singularities in the honeycomb and the Lieb lattices can be mapped from the momentum space to the real space. Three ways to explain the mapping are developed: One via the conservation of the total angular momentum and the pseudospin-orbit interaction. Another is via the far-field dynamics during the propagation of laser light through the photonic lattice. The third way is via topology and the Berry phase winding. We show that the topological explanation is fundamental. Based on this, we give a proposal for how our theory can be exploited in a 3D Weyl lattice to map a synthetic Weyl monopole from the momentum space to the real space. In the second part of the thesis, we study the higher-order topological insulators that have corner states that are also bound states in continuum. We study the 2D SSH lattice which is a 2nd-order topological insulator that supports bulk states and topological edge and corner states. We use nonlinearity to couple these states with one another. We show that the corner states couple to the edge states, and not the bulk states, for both the self-focusing and the self-defocusing nonlinearity. We also calculate a topological invariant of the system; its polarization. There is a sharp jump in polarization between the topologically trivial and nontrivial phases. We show that the nonlinear system inherits the jump in polarization from the linear system, and that the polarization can be tuned by the strength of the nonlinearity.



# Contents

<b>1</b>	<b>Introduction</b>	<b>1</b>
1.0.1	Periodic Systems . . . . .	2
1.0.2	Tools of the trade . . . . .	4
1.0.3	Topological phases of matter . . . . .	7
1.0.4	Topological order . . . . .	8
1.0.5	Topological photonics . . . . .	10
1.0.6	Thesis outline . . . . .	11
<b>2</b>	<b>Mapping of topological singularities from the momentum space to the real space</b>	<b>13</b>
2.0.1	Topological singularities in the momentum space . . . . .	13
2.0.2	Degrees of freedom . . . . .	14
2.1	Pseudospin - an emergent degree of freedom . . . . .	15
2.1.1	Honeycomb lattice . . . . .	15
2.1.2	Pseudospin-1/2 system . . . . .	17
2.1.3	Lieb lattice . . . . .	19
2.1.4	Pseudospin-1 system . . . . .	20
2.2	Experimental evidence of topological charge conversion . . . . .	23
2.2.1	Setup for a photonic lattice . . . . .	23
2.2.2	Topological charge conversion in the honeycomb lattice . . . . .	25
2.2.3	Topological charge conversion in the Lieb lattice . . . . .	27
2.3	Pseudospin-orbit interaction . . . . .	29
2.3.1	Kinematical description of the topological charge conversion . . . . .	29
2.3.2	Kinematics in the honeycomb lattice . . . . .	31
2.3.3	Kinematics in the Lieb lattice . . . . .	32
2.4	Mapping of vortices from the momentum space to the real space . . . . .	34
2.4.1	Dynamics in the honeycomb lattice . . . . .	34
2.4.2	Dynamics in the Lieb lattice . . . . .	38
2.5	Topological origin of the momentum-to-real-space mapping . . . . .	42
2.5.1	Topological charges in the momentum space . . . . .	42
2.5.2	Topology of the honeycomb lattice . . . . .	43
2.5.3	Topology of the Lieb lattice . . . . .	44
2.5.4	Berry phase winding as a signature of the topological charge conversion . . . . .	45
2.5.5	Topological charge conversion in a stretched lattice . . . . .	47
2.5.6	Beyond conical intersections . . . . .	48

2.6	A proposal for a 3D system . . . . .	49
2.6.1	The Weyl lattice . . . . .	49
2.6.2	Mapping of the Weyl monopole from the momentum space to the real space . . . . .	49
2.7	Chapter conclusion . . . . .	52
<b>3</b>	<b>Nonlinear control of higher-order topological insulators</b>	<b>55</b>
3.0.1	Higher-order topology . . . . .	55
3.0.2	Higher order topological insulators in the linear regime . . . . .	56
3.0.3	Nonlinearity in higher-order topological insulators . . . . .	57
3.0.4	Bound states in the continuum . . . . .	58
3.0.5	Chapter outline . . . . .	59
3.1	2D Su-Schrieffer-Heeger model . . . . .	60
3.1.1	Continuous SSH model . . . . .	60
3.1.2	Discrete model . . . . .	61
3.1.3	Band structure in the SSH model . . . . .	62
3.1.4	Experimental realization of a 2D SSH lattice . . . . .	63
3.2	Simulations in the discrete model . . . . .	65
3.2.1	Self-focusing nonlinearity . . . . .	65
3.2.2	Self-defocusing nonlinearity . . . . .	67
3.2.3	Beating between corner modes and edge modes . . . . .	69
3.3	Numerical methods for the continuous model . . . . .	70
3.3.1	Beam propagation simulation . . . . .	70
3.3.2	Long-range propagation of BICs . . . . .	71
3.4	Nonlinear control of HOTIs . . . . .	72
3.4.1	Nonlinear control of HOTIs in the experiment . . . . .	72
3.4.2	Simulation of nonlinear control of HOTI . . . . .	72
3.4.3	Polarization calculation . . . . .	75
3.5	Chapter conclusion . . . . .	77
<b>4</b>	<b>Thesis summary</b>	<b>81</b>
<b>5</b>	<b>Prošireni sažetak</b>	<b>85</b>
5.1	Uvod . . . . .	85
5.1.1	Topološka fotonika . . . . .	86
5.2	Preslikavanje topoloških singulariteta iz impulsnog u realni prostor . . . . .	87
5.2.1	Topološki singulariteti u fotoničkim rešetkama . . . . .	87
5.2.2	Kinematika i dinamika preslikavanja topoloških naboja iz impulsnog u realni prostor . . . . .	88
5.2.3	Topologija preslikavanja singulariteta iz impulsnog u realni prostor . . . . .	89
5.3	Nelinearni topološki izolatori višeg reda . . . . .	90
5.3.1	Topološki izolatori višeg reda . . . . .	90
5.3.2	Fotonička 2D SSH rešetka . . . . .	91
5.3.3	Nelinearna kontrola topoloških izolatora višeg reda . . . . .	92

---

5.4 Zaključak . . . . .	93
<b>Bibliography</b>	<b>95</b>
<b>Supervisor information</b>	<b>105</b>
<b>Curriculum vitae</b>	<b>107</b>
<b>List of publications</b>	<b>109</b>



# List of Figures

1.1	A donut is a cup. . . . .	1
1.2	Energy spectrum of a 1D system with a Bloch band structure. . . . .	3
1.3	Chern number calculation . . . . .	6
1.4	A Topological insulator . . . . .	8
1.5	Higher-order topological insulator . . . . .	9
1.6	A Photonic lattice. . . . .	11
2.1	2D Honeycomb lattice. . . . .	15
2.2	Honeycomb lattice spectrum. . . . .	16
2.3	Honeycomb lattice approximate spectrum. . . . .	18
2.4	2D Lieb lattice. . . . .	20
2.5	Lieb lattice spectrum. . . . .	21
2.6	Lieb lattice approximate spectrum. . . . .	23
2.7	Illustration of the momentum-to-real-space mapping of topological singularities	24
2.8	Experimental setup for optical induction of photonic HCL and Lieb lattices in a photorefractive crystal. . . . .	25
2.9	Photonic honeycomb lattice. . . . .	26
2.10	Excitation of pseudospin components of the HCL . . . . .	27
2.11	Photonic Lieb lattice. . . . .	28
2.12	Excitation of pseudospin components of the Lieb lattice . . . . .	29
2.13	Pseudospin decomposition in the HCL . . . . .	32
2.14	Pseudospin decomposition in the Lieb lattice . . . . .	33
2.15	Profiles of the HCL g-functions . . . . .	37
2.16	Intensity of the HCL g-functions. . . . .	38
2.17	Profiles of the Lieb lattice g-functions. . . . .	42
2.18	Intensity of the Lieb lattice g-functions. . . . .	42
2.19	Evolution of pseudospin states in stretched lattices. . . . .	47
3.1	Higher order topological insulator. . . . .	56
3.2	2D SSH Lattice. . . . .	57
3.3	Spectrum of a 2D SSH lattice. . . . .	59
3.4	Illustration of the nonlinear control of a higher-order topological insulator. . . .	61
3.5	Linear 2D SSH band structure. . . . .	62
3.6	Experimental realization and probing of linear 2D photonic SSH lattice. . . . .	64

3.7	Calculated nonlinear band structure and corner state tuning under a self-focusing nonlinearity. . . . .	66
3.8	Calculated nonlinear band structure and corner state tuning under a self-defocusing nonlinearity. . . . .	67
3.9	Localization of corner states. . . . .	69
3.10	Numerical simulation of the long-distance propagation of the states in a photonic HOTI. . . . .	71
3.11	Experimental demonstration of the nonlinear control of a higher-order topological insulator. . . . .	73
3.12	Numerical simulation of the nonlinear control of a photonic higher-order topological insulator. . . . .	75
3.13	Polarization of the nonlinear 2D SSH system as a function of nonlinearity. . . .	77

# Chapter 1

## Introduction

*"A topologist is a person who can't tell the difference between a coffee cup and a donut."  
-unknown*

Nature is wonderful, and it comes in all shapes and sizes. It speaks to us, in the language of mathematics, and, when we talk back, we call that physics. In this language of ours, to study the shapes and sizes is to study the *phases of matter*. Steam is an example of a gaseous phase of water, ice of its solid phase. And one phase can transform into another in a process called a *phase transition*. When we study such phases of matter, oftentimes we do not concern ourselves with the finer details of how our system looks like; we can be interested only in its global properties. The area of mathematics that studies global properties of objects is called *topology*. Topology is, intuitively, best first presented through the equivalence of a donut and a coffee cup shown in Fig. 1.1. A donut has one hole and so does a coffee cup. One can

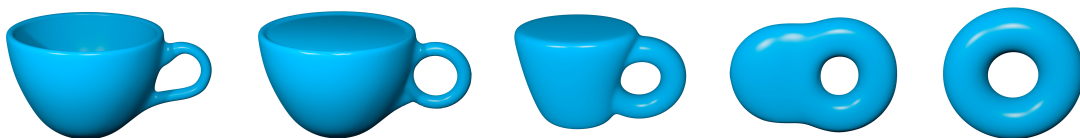


**Figure 1.1:** *A donut is a cup.* A coffee cup and a donut have the same topology. Both have one hole that is preserved under the continuous deformation from one to the other.

be transformed into the other via a continuous deformation, and, so, if we don't look at them too closely, they are one and the same. More rigorously, we say that the hole is a *topological property* that is preserved under a *continuous deformation* from a donut to a cup; both belong to the same *topological phase* of matter. In short, a donut and a cup have the same *topology*.

The study of topological phases of matter started in solid-state electronic systems. There, the experiments are performed, and the phenomena are observed, in the *real space*, but the properties of the system are studied in the *momentum space*. In particular, the topological properties of a system are revealed in the momentum space, so it is of great interest to study the momentum space, the real space and the relationship between them. The solid-state systems are oftentimes tedious to work with and are not as easily controllable as some others, e.g. the *photonic systems*, so we will look into how such a study can be performed in them. This is, of course, not only possible, but also preferable to studying the topological properties in the solid-state systems. Indeed, the field of *topological photonics* is now one of the hottest area of research in physics and has been like that since its inception over a decade ago.

In this thesis we will discuss how the study of topology started in the solid-state systems and how, and why, can these systems be replaced by photonic systems such as the *photonic lattices*. We will talk about the manifestations of the topological properties in the real space and the underlying theory in the momentum space and how they map from one space to the other. We will present various topological states, such as *edge states* and *corner states*, and the concepts of *topological insulators* and *topological invariants* that characterize them. Finally, we will introduce *nonlinearity* into our systems and study how it interacts with, and changes, the topology of the system.

## 1.0.1 Periodic Systems

To talk about topology in physics, we need to learn its language. Most often, we set out to talk about some kind of a system and the evolution of the state of a single particle in that system. To do that, we write down an evolution equation of a *single-particle* state  $\psi(\mathbf{r}, \mathbf{p}, t)$ :

$$H(\mathbf{r}, \mathbf{p}, t)\psi(\mathbf{r}, \mathbf{p}, t) = i\hbar\frac{\partial}{\partial t}\psi(\mathbf{r}, \mathbf{p}, t), \quad (1.1)$$

where  $\mathbf{r}$  is the position of the particle,  $\mathbf{p}$  is its momentum and  $H$  is the Hamiltonian that governs the time evolution of the state  $\psi(\mathbf{r}, \mathbf{p}, t)$ . The usual prescription for solving the equation is to pick an initial state, decompose it in a complete basis of the eigenstates  $\{\psi_n\}$  of the Hamiltonian with the corresponding eigenvalues  $\{E_n\}$ , and evolve it from there.

Apart from the obvious benefit of finding the solution to Eq. (1.1), there is additional merit in finding the eigenvalues and eigenstates of the Hamiltonian: It teaches us something about the physics of the problem. To start off, we can specify the shape of the Hamiltonian a little bit. At a given point in time, we are interested in systems that are *periodic* in space, e.g. lattices. Therefore, we are interested in time-independent Hamiltonians that are spatially periodic.

Mathematically, we express this as:

$$H(\mathbf{r} + \mathbf{R}, \mathbf{p}) = H(\mathbf{r}, \mathbf{p}), \quad (1.2)$$

where  $\mathbf{R} = \sum_i m_i \mathbf{a}_i$ ,  $m_i \in \mathbb{Z}$  is the direct lattice vector that defines the period of the system and  $\{\mathbf{a}_i\}$  is the set of lattice vectors. Because the Hamiltonian is spatially periodic, we can invoke the *Bloch theorem* [1] that states that the eigenstates  $\Psi_n$  of a periodic Hamiltonian can be separated into two parts; one that is a plane wave  $e^{i\mathbf{k}\cdot\mathbf{r}}$ , and another part, that is a periodic function  $u_{n,\mathbf{k}}(\mathbf{r})$ :

$$\Psi_{n,\mathbf{k}}(\mathbf{r}) = e^{i\mathbf{k}\cdot\mathbf{r}} u_{n,\mathbf{k}}(\mathbf{r}). \quad (1.3)$$

$u_{n,\mathbf{k}}(\mathbf{r})$  have the same period as the original Hamiltonian in Eq. (1.2), i.e.  $u_{n,\mathbf{k}}(\mathbf{r}) = u_{n,\mathbf{k}}(\mathbf{r} + \mathbf{R})$ , and are eigenstates of the Bloch Hamiltonian:

$$H_{\mathbf{k}} = e^{-i\mathbf{k}\cdot\mathbf{r}} H(\mathbf{r}, \mathbf{p}) e^{i\mathbf{k}\cdot\mathbf{r}}, \quad (1.4)$$

so that:

$$H_{\mathbf{k}} u_{n,\mathbf{k}}(\mathbf{r}) = E_{n,\mathbf{k}} u_{n,\mathbf{k}}(\mathbf{r}). \quad (1.5)$$

$E_{n,\mathbf{k}}$  is the *energy spectrum*,  $\mathbf{k}$  is known as *crystal momentum*, and  $n$  refers to the energy band in the energy spectrum in the momentum space. An energy spectrum with the Bloch band structure is shown in Fig. 1.2. For a given  $n$ , the eigenstate  $\Psi_{n,\mathbf{k}}$  is a continuous function of  $\mathbf{k}$ .

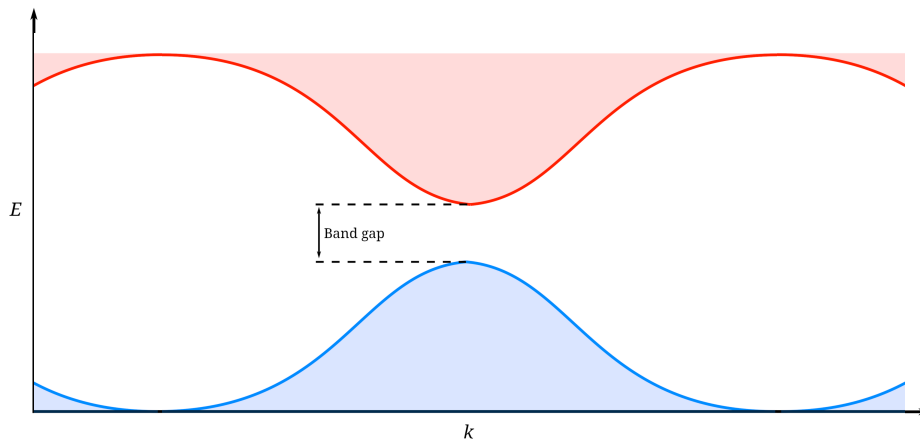


**Figure 1.2:** Energy spectrum of a 1D system with a Bloch band structure. The eigenenergies form energy bands that can, in general, be separated by a band gap. Topological properties of the system can depend on the presence of such a gap between the energy bands.

It is also a periodic function in the momentum space that is unique only over the *first Brillouin zone* defined by the reciprocal lattice vector  $\mathbf{K}$ , which is defined by  $\mathbf{K} \cdot \mathbf{R} = 2\pi N$ ,  $N \in \mathbb{N}$ , so that  $u_{n,\mathbf{k}} = u_{n,\mathbf{k}+\mathbf{K}}$ . Physics is contained in both the spectrum  $E_{n,\mathbf{k}}$  and in the geometrical shape of the eigenstates  $u_{n,\mathbf{k}}(\mathbf{r})$ . To study the topology of the eigenstates, we make use of concepts such as the *Berry connection*, *Berry curvature*, *Berry phase* [2, 3], and the *Chern number* [4]. Let us introduce them in the next subsection.

## 1.0.2 Tools of the trade

We are interested in systems where the Hamiltonian is dependent on a parameter, or a set of parameters, in a parameter space. In general, the Berry phase can be defined for any kind of parameter space, as long as the evolution of the parameter is slow enough so that the state of the system changes adiabatically [5]. We are, however, interested only in systems where the Hamiltonian is dependent on the crystal momentum  $\mathbf{k}$  and the eigenstates  $u_{n,\mathbf{k}}$  that change adiabatically over the first Brillouin zone. An eigenstate,  $u_{n,\mathbf{k}}$ , that evolves adiabatically over a closed path in the momentum space acquires a *dynamical* phase during the corresponding time:

$$\phi = -\frac{1}{\hbar} \int E_n(t) dt, \quad (1.6)$$

and a geometrical phase, called the *Berry phase*:

$$\gamma = \oint \mathcal{A}_n(\mathbf{k}) \cdot d\mathbf{k}, \quad (1.7)$$

where  $\mathcal{A}_n(\mathbf{k})$  is the *Berry connection*:

$$\mathcal{A}_n(\mathbf{k}) = i \langle u_{n,\mathbf{k}} | \nabla_{\mathbf{k}} | u_{n,\mathbf{k}} \rangle. \quad (1.8)$$

The definition of the Bloch states in Eq. (1.5) does not specify the overall phase of Bloch states  $u_{n,\mathbf{k}}$ . We can then freely choose the phase of the Bloch states, i.e. we can associate a phase  $\chi(\mathbf{k})$  with the eigenstates  $u_{n,\mathbf{k}}$  in terms of a phase factor, i.e. we can set  $e^{i\chi(\mathbf{k})} u_{n,\mathbf{k}}$ , without changing its definition in Eq. (1.5). Plugging this into Eq. (1.8), we find that the Berry connection is not gauge invariant and that it transforms as:

$$\mathcal{A}_n(\mathbf{k}) \mapsto \mathcal{A}_n(\mathbf{k}) - \nabla \chi(\mathbf{k}). \quad (1.9)$$

The Berry phase is, however, gauge invariant modulo  $2\pi$ , because an eigenstate  $u_{n,\mathbf{k}}$  must be single-valued at the start and at the end of its adiabatic evolution. Because the Berry connection

is not gauge invariant, it is useful to define a quantity, called the *Berry curvature*, that is gauge invariant:

$$\Omega_n(\mathbf{k}) = \nabla_{\mathbf{k}} \times \mathcal{A}_n(\mathbf{k}). \quad (1.10)$$

The Berry curvature in Eq. (1.10) is sometimes suggestively labeled as  $\mathcal{B}_n(\mathbf{k})$ , because, together with the Berry connection  $\mathcal{A}_n(\mathbf{k})$ , and Eq. (1.9), it is reminiscent of the magnetic field and the vector potential from classical electrodynamics. This can be exploited to obtain artificial magnetic fields in ultracold atomic gases [5]. We are, however, not interested in the generation of artificial gauge fields, but in the study of the topology of a given system. To that end, we are mostly concerned with whether the phase of the Bloch state is a continuous function. Whether it is, or it is not, depends on a class of quantities called *topological invariants*. One such quantity is the *Chern number*, calculated by integrating the Berry curvature over the first Brillouin zone (BZ) for a 2D system:

$$C_n = \frac{1}{2\pi} \int_{\text{BZ}} \Omega_n(k_x, k_y) d^2k. \quad (1.11)$$

By using the definition of the Berry curvature in Eq. (1.10) and the Stokes' theorem, we can recast the Chern number into a form of a line integral of the Berry connection along the boundary of the Brillouin zone ( $\partial S$ ):

$$C_n = \frac{1}{2\pi} \oint_{\partial S} \mathcal{A}_n(\mathbf{k}) \cdot d\mathbf{k}. \quad (1.12)$$

If the phase  $\chi$  of the eigenstate  $u_{n,\mathbf{k}}$  is continuous, so is the Berry connection, as per Eq. (1.9). Then, from Eq. (1.12), it follows that the Chern number is zero. We call this phase a *topologically trivial* phase. In contraposition, if the Chern number is not zero, the phase is not continuous. This phase is called a *topologically non-trivial* phase. It can also be shown that the Chern number takes integer values [6, 4]: Suppose we divide the Brillouin zone into two regions as in Fig. 1.3. Then we can divide the integral in Eq. (1.11) into two parts; one part over the region  $S$  and another over the region  $S'$ :

$$C_n = \frac{1}{2\pi} \int_S \Omega_n(k_x, k_y) d^2k + \frac{1}{2\pi} \int_{S'} \Omega_n(k_x, k_y) d^2k. \quad (1.13)$$

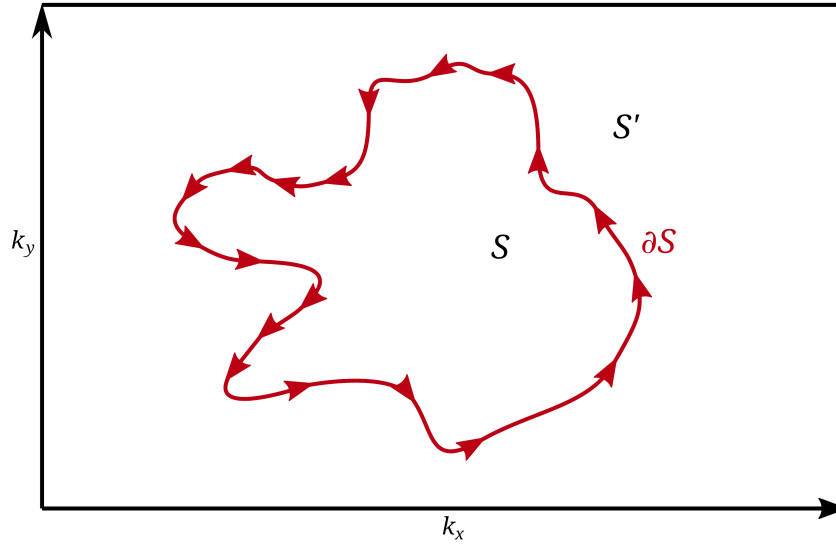


**Figure 1.3:** *Chern number calculation.* The Chern number is calculated in the 1st Brillouin zone. The Brillouin zone can be divided into two parts: One part encompasses the region  $S$  and the other the region  $S'$ . The two regions share a common boundary along which we perform the line integral used to calculate the Chern number.

Crucially, these two regions share a common boundary, so the Chern number turns out to be equal to the difference of the Berry phases in the two regions, divided by  $2\pi$ :

$$\begin{aligned} C_n &= \frac{1}{2\pi} \oint_{\partial S} \mathcal{A}_n(\mathbf{k}) \cdot d\mathbf{k} - \frac{1}{2\pi} \oint_{\partial S'} \mathcal{A}'_n(\mathbf{k}) \cdot d\mathbf{k} \\ &= \frac{1}{2\pi} (\gamma - \gamma'). \end{aligned} \quad (1.14)$$

The two Berry phases,  $\gamma$  and  $\gamma'$ , are calculated along the same loop, so their difference,  $\gamma - \gamma'$ , must be a multiple of  $2\pi$ . This, in turn, implies that the Chern number is an integer. Also, notice how we did not specify the shape of the integration regions  $S$  and  $S'$ . The Chern number stays constant under continuous deformations of the integration path and only discontinuities in the momentum space can change its value. For this reason, we call it a *topological invariant* and its topological origin was demonstrated in [7, 8].

There are, of course, other topological invariants such as the Euler characteristic [9], the winding number [10] etc. What they all have in common is that they reveal the topological properties of the systems we study. It is of great interest to study topologically non-trivial systems, to study how their topological phases change, how this relates to the system's topological invariants and how they manifest in observable physical phenomena. Now that we have learned the language of the topological quantum mechanics, and before we move onto the systems we

are interested in, we will present a brief overview of the study of topological phases of matter; of how it all started in solid-state physics and how it led to topological photonics.

### 1.0.3 Topological phases of matter

The research into topological phases of matter started in solid-state electronic systems with the discovery of the *integer quantum Hall effect* [11, 12]. There it was shown that the Hall conductance of a 2D electron gas, in a perpendicular magnetic field, comes in integer values of the fundamental constant  $e^2/h$  and that this is independent of the geometry of the device used in the experiment. The Hall conductance,  $\sigma_{xy}$ , was famously related to the Chern number [13]:

$$\sigma_{xy} = -\frac{e^2}{h} \sum_n C_n, \quad (1.15)$$

where  $C_n$  is the Chern number of the corresponding occupied Bloch band in the energy spectrum. This 2D electron gas, realized in a semiconductor, was the first example of a system where the momentum-space topology leads to observable physical phenomena. In general, materials that are insulators in the bulk, but support conductive states on their edges, are called *topological insulators* [14].

The *edge states* are best understood through the *bulk-boundary correspondence* [15, 16]: Suppose we have two materials each with a different topological invariant. Bloch bands of the bulk, that correspond to excited and unexcited states, form in the energy spectrum. Now suppose we bring the two materials into contact with each other along an edge. This gives us a new material with two different topological invariants on either side of the boundary. Because a topological invariant can not change under a continuous transformation, this implies that a discontinuous transformation happened, i.e. that the band gap has closed somewhere along the edge and that a conductive edge state appeared with an energy inside the band gap, as can be seen in Fig. 1.4.

The fundamental concept underlying the appearance of the edge states in various materials is a *breaking of symmetry*. In the case of two materials, with two different Chern numbers, if we were to make the transformation  $\mathbf{r} \mapsto -\mathbf{r}$ , we would get its mirror image, with the Chern numbers that have swapped values, i.e. it is the *spatial inversion symmetry* that is broken. Our search for topologically nontrivial states of matter, such as the edge states, then comes down to a search for systems with some kind of a symmetry and nontrivial topological invariants that characterize it.

In the integer quantum Hall effect, it is the *time reversal symmetry* that is broken due to the

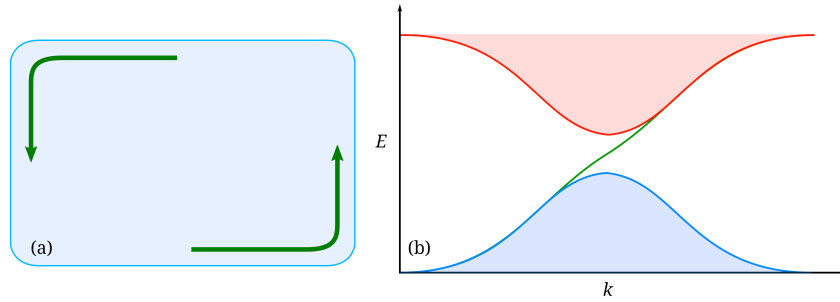


**Figure 1.4:** A Topological insulator. (a) An illustration of a topological insulator with localized unidirectional edge states. (b) Energy spectrum of a topological insulator. The edge state energy is located inside the band gap.

presence of a non-zero magnetic field. Under the transformation  $t \mapsto -t$ , the Lorentz force on the electrons changes its direction which in turn changes the direction of the conductive edge state and gives us the mirror image of the insulator. It is possible to introduce disorder into the system in the form of a random variation of the potential that produces the magnetic field. The strength of the magnetic field determines the size of the band gap. The fluctuations in the potential modify the energy bands, but as long as the disorder is not too large, and the band gap does not close, the edge states will not couple to the bulk states and will not change their direction. More rigorously; so long as the disorder does not change the topological invariants of the system, i.e. does not change the topology by closing the band gap, the edge states are *topologically protected*. It does not matter what the shape of the disorder is or where in the system it is applied, the only thing that matters is its strength. This robustness against disorder and backscattering was shown in detail in [17, 18, 19].

Any prospect for lossless and protected transport is of great fundamental interest, and of special interest for potential applications, so the discovery of topologically protected transport sparked great interest in topological physics. The research was mainly conducted in electronic systems, via the prescription given earlier: look for systems with topological invariants and a way to break their symmetries. Success was found with the discovery of the quantum spin Hall systems [20, 21], where topologically protected transport of spin states was achieved, and research into the topological phases in other solid-state systems soon followed [22, 23].

#### 1.0.4 Topological order

The systems mentioned thus far exhibit the bulk-boundary correspondence and are 2-dimensional. In general, they can be of any dimension  $d$  and, as long as the bulk-boundary correspondence is

obeyed, they will support bulk states, that are insulating, and topologically protected edge states that are conductive. The bulk states have the same dimension as the system itself. The edge states have a dimension by  $n = 1$  smaller than that of the system. Such topological insulators are then called the *first-order topological insulators*.

Topological insulators that support states with dimension  $(d - n)$ , and  $n > 1$ , have been predicted in [24, 25, 26, 27, 28] and experimentally observed in [29, 30, 31]. Such systems are called the *higher-order topological insulators*, or HOTIs for short. It is possible to paint a very intuitive picture of a HOTI using an example of a 2D finite-sized square-shaped topological insulator like the one depicted in Fig. (1.5). Such a system has three distinct classes of states with

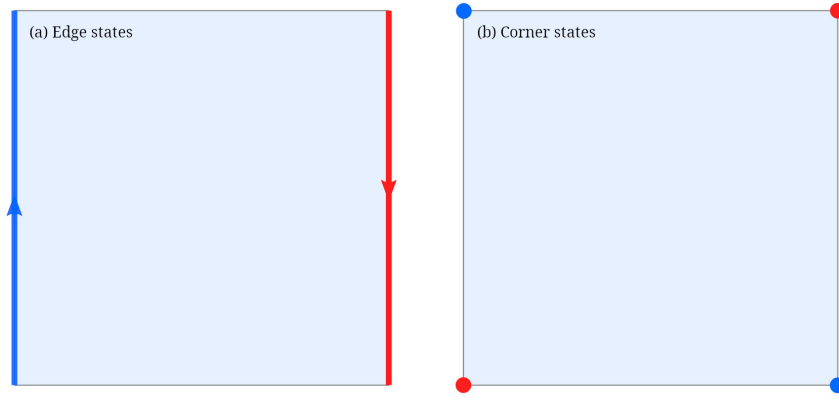


**Figure 1.5:** *Higher-order topological insulator.* A 2-dimensional HOTI supports both (a) the edge states, that are 1-dimensional, and (b) the corner states that are 0-dimensional.

different dimensions. Two we have encountered already; the bulk is 2-dimensional and is an insulator; the edges are 1-dimensional and support topologically protected transport. The third distinct class of states are the states localized in the corners with dimension  $(d - n) = 0$ . This, in turn, gives us the order  $n$  of our HOTI which is 2, so we call it a *second-order topological insulator*.

To describe the physics of a 1st-order topological insulator, the relevant quantity is the Chern number defined in Eq. (1.11) and related to Hall conductance via Eq. (1.15) in the integer quantum Hall effect. For the 2nd-order topological insulators, the relevant quantity is the Zak phase [32]:

$$\Theta_n = -\frac{1}{2\pi} \int_{BZ} \mathcal{A}_n(k_x, k_y) dk_x dk_y, \quad (1.16)$$

where  $\mathcal{A}_n(k_x, k_y)$  is the Berry connection of Eq. (1.8), and  $n$ , again, refers to the respective Bloch band in the momentum space. Related to the Zak phase is the polarization of the system,

via  $\Theta_n = 2\pi P_n$  [33, 34], so that the total polarization is:

$$P = \frac{1}{2\pi} \sum_n \Theta_n. \quad (1.17)$$

In electronic systems, the polarization is related to the dipole moment. Similar considerations can be made for the quadrupole and higher multipole electric moments [24]. The prescription for studying HOTIs stays the same as the one for traditional topological insulators; find a system with, preferably, non-trivial topology, identify the symmetries of the system, calculate the relevant topological invariants and relate them to observable physical quantities such as the polarization.

### 1.0.5 Topological photonics

The study of topological states of matter started in the solid-state systems, but the move onto photonic platforms soon followed. The key to make this possible was the observation by Haldane and Raghu that the topological band structure was a common property of waves propagating through a periodic medium, no matter if the waves are quantum or classical in nature [35, 36]. They studied electromagnetic waves that propagates through a *photonic crystal*. In essence, a photonic crystal is a dielectric material whose refractive index changes periodically. As such, a photonic crystal acts as a waveguide that supports one way propagation of electromagnetic energy. Because they are periodic, they exhibit the topological band structure, and, Haldane and Raghu have shown that they can, in principle, support unidirectional photonic edge states that are analogous to the edge states in the quantum Hall effect. The key for attaining the unidirectional edge states was the presence of magneto-optical media in the crystal that break the time-reversal symmetry and lead to non-trivial topological invariants. Soon after, a realistic proposal for a 2D magneto-optical photonic crystal in the microwave domain that supports unidirectional edge states was put forward [37] and experimentally realized [38]. In optical domain, an analogue of quantum spin Hall effect, using internal degrees of freedom of photons called *pseudospin*, soon followed [39, 40, 41]. With that, the field of topological photonics was born.

The systems obtained by propagation of electromagnetic waves through periodic photonic crystals we are most interested in are called *photonic lattices*. To get a photonic lattice, laser light is sent through a refractive crystal whose index of refraction varies periodically forming the lattice pattern as can be seen in Fig. (1.6). The photonic crystal is a 3D object with three well defined axes. The light propagates along one of the axes, which we denote as the  $z$ -axis. The lattice pattern is formed in the  $x - y$  plane perpendicular to the  $z$ -axis. The propagation of

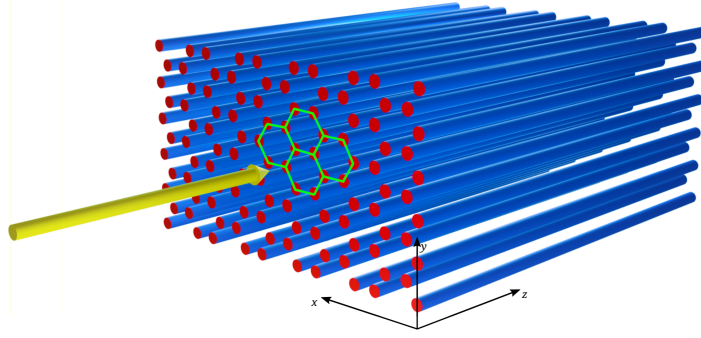


**Figure 1.6:** *A Photonic lattice.* Illustration of the idea behind the photonic lattices. Laser light is sent through a photorefractive crystal, in the  $z$ -direction, to form waveguides (blue) in the desired lattice pattern (red/green), in the  $x-y$  plane. The lattice can then be probed by a laser beam (yellow) in experiments.

light is then governed by the paraxial wave equation [42, 43, 44, 45]:

$$i \frac{\partial \Psi(x, y, z)}{\partial z} = -\frac{1}{2k_0} \nabla^2 \Psi(x, y, z) - \frac{k_0 \Delta n(x, y)}{n_0} \Psi(x, y, z) = H \Psi(x, y, z), \quad (1.18)$$

where  $x, y$  and  $z$  are the spatial coordinates,  $k_0$  is the wavevector,  $n_0$  the refractive index of the background medium,  $\Delta n(x, y)$  is the induced refractive index that forms the lattice and  $H$  is the Hamiltonian of the system. It is crucial to notice that the paraxial wave equation (2.3) has the form of a Schrödinger equation (1.1). Two things are then important: The first is that the  $z$  coordinate in the paraxial wave equation replaces the time  $t$  in the Schrödinger equation; so, in photonic lattices, the  $z$  coordinate plays the role of time and the lattice is formed in the  $x-y$  plane making it effectively a 2D system. The second thing is that the Hamiltonian that governs the propagation is periodic because the refractive index is periodically modulated. Because the Hamiltonian is periodic, the system exhibits the Bloch band structure and we can use the formalism of topological phases of matter we introduced earlier to study the topology in photonic systems.

## 1.0.6 Thesis outline

In this thesis we aim to study topology of 2D photonic lattices. In the first part, we study the topological properties of 2D honeycomb [45] and Lieb lattices [46] that have *topological singularities* in the momentum space. We observe experimentally that those singularities map from the momentum space to the real space during the propagation of laser light through the lattice. An explanation for the observed mapping is given in the context of conservation of

angular momentum via the pseudospin-orbit interaction [45], and the far-field dynamics are studied. Then we introduce systems where the angular momentum is not conserved and the pseudospin-orbit interaction picture breaks down, but the mapping persists, and we show that the fundamental reason for the mapping is topological in origin and rests on the fact that the topological singularity in the momentum space gives rise to a non-trivial topological invariant called the *Berry phase winding* which has observable effect in the real space [47]. Finally, we show how our theory of momentum-to-real space mapping can be applied to 3D topological singularities to obtain a synthetic Dirac-Weyl monopole [48, 49, 50] in the real space.

In the second part we continue to study the topology in the momentum space and its effects in the real space in HOTIs. We make use of the Su-Schrieffer–Heeger (SSH) model [51] which was first studied by Barišić, Labbé and Friedel [52, 53, 54]. A photonic 2D SSH lattice supports topologically protected corner states. These corner states are also *bound states in continuum* [55, 56, 57]. We introduce nonlinearity into the system that breaks the symmetry responsible for the topological protection of the corner states and observe experimentally that the corner states couple to the edge states, but, surprisingly, not to the bulk states. Then we turn to the study of the eigenvalue spectrum in the momentum space. We calculate the polarization of the system, show that it is tunable by the nonlinearity and we show that the topological properties are inherited from the linear system. The tunability of the system via the change in nonlinearity has potential applications in topology driven devices, while the interplay of nonlinearity and topology is of great fundamental interest in physics.

## Chapter 2

# Mapping of topological singularities from the momentum space to the real space

The work presented in this chapter has been published in:

- X. Liu, S. Xia, E. Jajtić, D. Song, D. Li, L. Tang, D. Leykam, J. Xu, H. Buljan & Z. Chen, Universal momentum-to-real-space mapping of topological singularities. *Nat Commun* **11**, 1586 (2020).

### 2.0.1 Topological singularities in the momentum space

One of the goals of this thesis is to study the topological properties of materials in the momentum space, in the real space and the relation between them. To that end, we employ systems whose structure gives rise to topological singularities in the momentum space, because they offer us a handy way to demonstrate a mapping from the momentum space to the real space. But, first, we need to explain what a singularity is, and, what makes a topological singularity *topological*. Suppose we have *an object* in *a space*. If that object is ill-behaved (e.g. not differentiable) at any point in space, we call that point *a singularity*. A *topological* singularity is a singularity that arises from the structure of the object, and, one that can not be done away with by a continuous deformation. A very intuitive example is, again, that of a donut. A donut has a hole and no amount of continuous deformations can close that hole. Sure, a continuous deformation can infinitely shrink it into a point, but it can not close it. Only a discontinuous transformation can close the hole, but then this is not a donut anymore, but topologically a completely different object. In the context of topological photonics, systems exhibiting topological singularities are the various forms of photonic lattices. The two lattices we employ to demonstrate a mapping of topological singularities from momentum space to real space are the *photonic honeycomb*

*lattice* [45, 58] and the *photonic Lieb lattice* [46]. There are two reasons for this. The first reason is that they have topological singularities in momentum space called the Dirac points [59, 4], and the second is that they exhibit a degree of freedom called *pseudospin* that emerges from their substructure and that we can exploit to demonstrate the mapping.

## 2.0.2 Degrees of freedom

Pseudospin is best introduced by an analogy with the spin that is an intrinsic property of quantum objects. Spin is a degree of freedom that satisfies the spin algebra:

$$[S_a, S_b] = 2i\epsilon_{abc}S_c, \quad (2.1)$$

where  $S_n$ ,  $n = x, y, z$ , are the spin matrices, and  $\epsilon_{abc}$  is the Levi-Civita tensor. In general, this is the algebra of an angular momentum. In particular, another degree of freedom that is of interest is the orbital angular momentum (OAM), denoted by  $L$ , with an equivalent algebra:

$$[L_a, L_b] = 2i\epsilon_{abc}L_c, \quad (2.2)$$

that can interact with the spin. The coupling of spin and orbital degrees of freedom is in many systems intertwined with the underlying topology of the space and the Berry phase [2, 60]. For instance, in condensed matter electronic systems, studies of spin-orbit interactions led to the discovery of topological insulators mentioned earlier [13, 11, 12]. There are also various related examples in optics and photonics [61]. There, the Berry phase optical elements in real space, such as the q-plates and metasurfaces support circularly polarized states of light, i.e. intrinsic spin, that can be transformed to optical vortices carrying orbital angular momentum [62, 63, 64]. For light propagating along a coiled ray trajectory, the dynamics is governed by the action of a monopole in the Berry curvature, which leads to the spin-Hall effect of light [65]. An analogous topological transport of sound waves has also been observed, thanks to the spin-redirection geometric phase [66]. When we discuss spin in optical systems, it is the light polarization or the photon spin that is usually considered as the spin degree of freedom [61, 67]. Similarly, in electronic systems it is the intrinsic electron spin [11, 20]. However, for light that propagates in structured photonic media, i.e. in the crystalline lattices, with microscopic degrees of freedom, the concept of pseudospin independent of any intrinsic particle property emerges [45, 58, 46, 68, 69, 70]. In a lattice, the pseudospin is introduced through the mathematical analogy between the sublattice degree of freedom and the electron spin in the Dirac equation. Unlike the electron spin, however, the pseudospin angular momentum is not associated with

any intrinsic property of particles, but rather arises from the substructure of space, i.e. from the sublattices, that the particles, or wave packets, live in.

## 2.1 Pseudospin - an emergent degree of freedom

### 2.1.1 Honeycomb lattice

In order to introduce pseudospin, we can make use of a photonic honeycomb lattice (HCL), which is the photonic equivalent of a graphene lattice in solid-state physics [71, 72, 73]. The honeycomb lattice is shown in Fig. 2.1. It is a 2D hexagonal lattice, with a very important

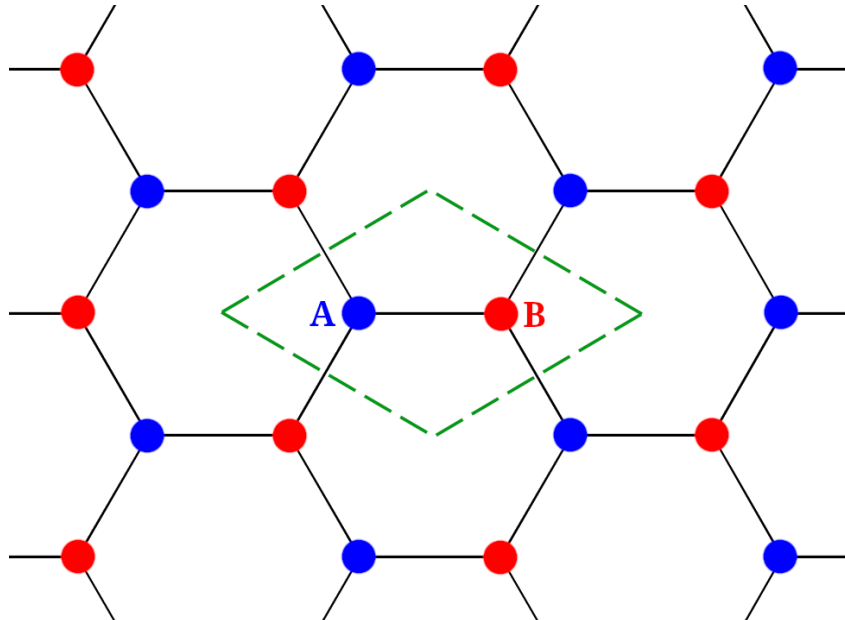


**Figure 2.1:** *2D Honeycomb lattice.* The hexagonal Honeycomb lattice consists of two triangular sublattices, A and B. The sites of the sublattice A are marked blue, and the sites of the sublattice B are marked red. The unit cell is marked by a dashed green line.

feature; it is composed of two triangular *sublattices* [42, 74], marked A and B in the figure. As with any other photonic lattice, the propagation of light is governed by the paraxial wave equation introduced earlier in Eq. (2.3), and repeated here for discussion purposes:

$$i\frac{\partial\Psi(x,y,z)}{\partial z} = H\Psi(x,y,z). \quad (2.3)$$

To work out the Hamiltonian  $H$ , such a system is often treated in the tight-binding approximation [59], where only the interaction between nearest neighbouring lattice sites is considered.

Crucially, because there are two sublattices, the corresponding Bloch Hamiltonian  $H_{\mathbf{k}}$  in the momentum space is a  $2 \times 2$  matrix [75]:

$$H_{\mathbf{k}} = -t \sum_{n=1}^3 \begin{pmatrix} 0 & \cos(\mathbf{k} \cdot \delta_n) - \sin(\mathbf{k} \cdot \delta_n) \\ \cos(\mathbf{k} \cdot \delta_n) + \sin(\mathbf{k} \cdot \delta_n) & 0 \end{pmatrix}, \quad (2.4)$$

where  $\delta_n$  are the nearest-neighbour vectors:

$$\delta_1 = \frac{a}{2}(\sqrt{3}, 1), \quad \delta_2 = \frac{a}{2}(-\sqrt{3}, 1), \quad \delta_3 = a(0, -1), \quad (2.5)$$

$\mathbf{k} = k_x \mathbf{x} + k_y \mathbf{y}$  is the crystal momentum,  $a$  is the distance between the neighbouring lattice sites and  $t$  is the hopping between them. To study the physics of the system, we need to look at the energy spectrum in the momentum space. We do that by finding the eigenvalues of the Hamiltonian in Eq. (2.4):

$$\beta_{\pm, \mathbf{k}} = \pm t \sqrt{3 + 2 \cos(\sqrt{3} k_y a) + 4 \cos(\sqrt{3} k_y a / 2) \cos(3 k_x a / 2)}. \quad (2.6)$$

In photonics, the eigenvalues are often denoted by  $\beta_{n, \mathbf{k}}$  and are called *propagation constants*. They have the opposite sign to energies  $E_{n, \mathbf{k}}$  in solid-state systems, i.e.  $\beta_{n, \mathbf{k}} = -E_{n, \mathbf{k}}$ . The propagation constants in the momentum space are shown in Fig. 2.2. Immediately we can

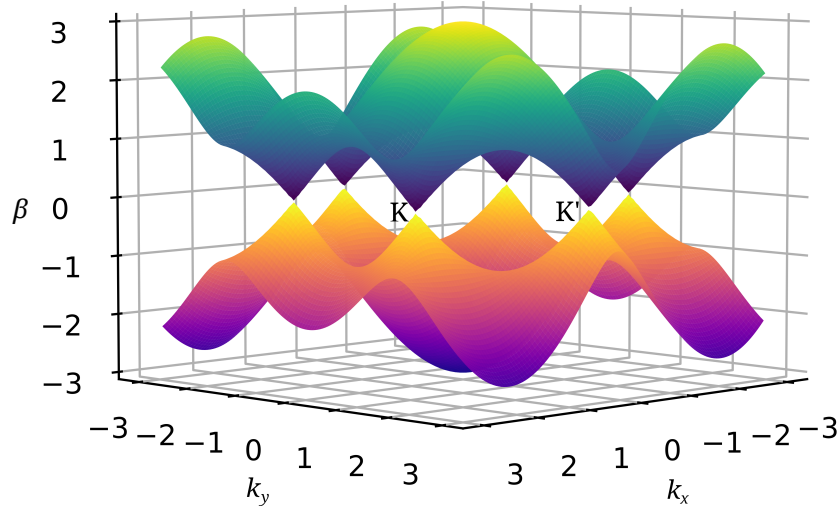


**Figure 2.2:** *Honeycomb lattice spectrum.* Because the honeycomb lattice consists of two sublattices, it has two bands in the energy spectrum in the momentum space. The two bands touch at the Dirac points. Two inequivalent Dirac points are marked by K and K'. The parameters  $t$  and  $a$  are taken as unity.

notice a couple of features that merit further discussion. First is that the energy spectrum has

the Bloch band structure. Second is that there are exactly two bands because the Hamiltonian is a  $2 \times 2$  matrix, which itself is a consequence of the fact that the honeycomb lattice consists of two sublattices. Third is that the two lattices touch at certain points. These points are located in the corners of the 1st Brillouin zone and are called the *Dirac points*. There are two inequivalent Dirac points marked with  $\mathbf{K}$  and  $\mathbf{K}'$ . These Dirac points are the topological singularities [76] that we are interested in.

### 2.1.2 Pseudospin-1/2 system

To study the topology of the system, it is sufficient to limit ourselves to the vicinity of the Dirac points; far away from the singularities, the topology is trivial. In the vicinity of a Dirac point, we can linearize the Hamiltonian in Eq. (2.4). Without loss of generality, we can pick one of the two points, so we set  $\mathbf{k} \mapsto \mathbf{k} + \mathbf{K}$ , where  $\mathbf{K}$  is the reciprocal lattice vector, introduced in the subsection 1.0.1, to get:

$$H_{\mathbf{k}+\mathbf{K}} \approx \frac{\kappa}{2} \begin{pmatrix} 0 & k_x + ik_y \\ k_x - ik_y & 0 \end{pmatrix}, \quad (2.7)$$

where  $\kappa = 3at/2$ . The eigenvalues of this Hamiltonian are:

$$\beta_{n,\mathbf{k}} = n \frac{\kappa}{2} \sqrt{k_x^2 + k_y^2} = n \frac{\kappa}{2} k, \quad (2.8)$$

where  $n = \pm 1$  denotes the band number. The eigenvalues are linear in  $k = \sqrt{k_x^2 + k_y^2}$ , as can be seen in Fig. 2.3. The corresponding eigenstates are:

$$\Psi_{n,\mathbf{k}} = \frac{1}{\sqrt{2}} \begin{pmatrix} n \\ e^{i\varphi_{\mathbf{k}}} \end{pmatrix}, \quad (2.9)$$

where  $\varphi_{\mathbf{k}}$  is defined by  $k_x + ik_y = ke^{i\varphi_{\mathbf{k}}}$ . The form  $e^{i\varphi_{\mathbf{k}}}$  is reminiscent of a topological singularity in the form of a vortex [77] in the momentum space and will play a prominent role in describing the mapping of topological singularities from the momentum space to the real space.

The Hamiltonian in Eq. (2.7) can be rewritten in the form:

$$H_{\mathbf{k}} = \kappa \mathbf{S} \cdot \mathbf{k}, \quad (2.10)$$

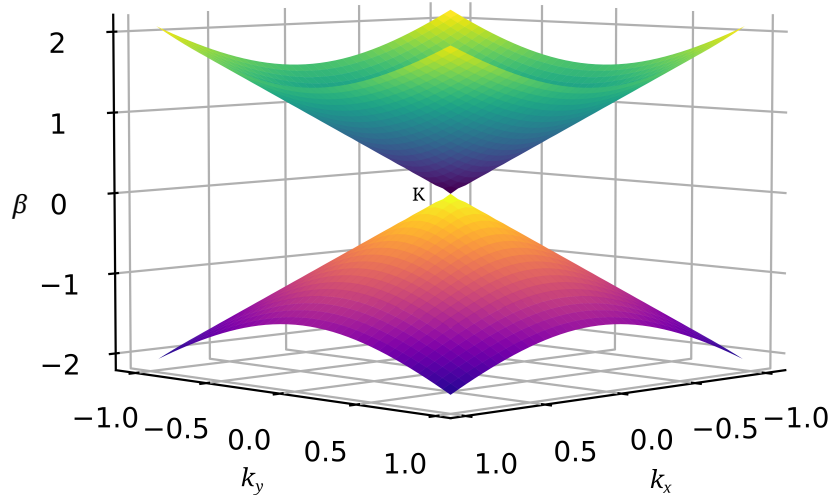


**Figure 2.3:** *Honeycomb lattice approximate spectrum.* Propagation constants of the honeycomb lattice in the vicinity of the Dirac point take the shape of a cone. The Dirac point at the conical intersection is marked with  $\mathbf{K}$ . The parameter  $\kappa$  is equal to  $3/2$ .

where we have dropped  $\mathbf{K}$  because we can always move the origin of the coordinate system so that  $\mathbf{K} = 0$ , and where  $\mathbf{S} = \boldsymbol{\sigma}/2 = (\boldsymbol{\sigma}_x \mathbf{x} + \boldsymbol{\sigma}_y \mathbf{y})/2$ , and  $\boldsymbol{\sigma}_x$  and  $\boldsymbol{\sigma}_y$  are the Pauli matrices:

$$\boldsymbol{\sigma}_x = \begin{pmatrix} 0 & 1 \\ 1 & 0 \end{pmatrix}, \boldsymbol{\sigma}_y = \begin{pmatrix} 0 & -i \\ i & 0 \end{pmatrix}. \quad (2.11)$$

$S_x = \boldsymbol{\sigma}_x/2$  and  $S_y = \boldsymbol{\sigma}_y/2$ , together with  $S_z$ ;

$$S_z = \frac{1}{2}\boldsymbol{\sigma}_z = \frac{1}{2} \begin{pmatrix} 1 & 0 \\ 0 & -1 \end{pmatrix}, \quad (2.12)$$

satisfy the spin algebra in Eq. (2.1). The diagonal elements of the Hamiltonian are 0, so this Hamiltonian is equivalent to the Hamiltonian of a massless spin-1/2 particle. An important distinction needs to be made here: We are not working with atoms, but with photonic lattices. As mentioned earlier, this spin-like degree of freedom is not the real electron spin, or even the light polarization or the photon spin that are usually associated with the spin-like degree of freedom in optical systems. Instead, this degree of freedom is a feature of the lattice itself, and we call it *pseudospin*. The pseudospin emerges from the structure of the lattice itself; if there were no sublattices, there would be no pseudospin. The  $z$ -component of the pseudospin,  $S_z$ , is of special interest because it is diagonal, with eigenvalues  $s = +1/2$  and  $s = -1/2$ . The

eigenvalues  $s$  and eigenstates  $\chi_{S,s}$  are defined by:

$$S_z \chi_{S,s} = s \chi_{S,s}. \quad (2.13)$$

The eigenstate

$$\chi_{\frac{1}{2},\frac{1}{2}} = \begin{pmatrix} 1 \\ 0 \end{pmatrix} \quad (2.14)$$

is called the *pseudospin up*. It corresponds to the eigenvalue  $s = 1/2$  and it is associated with the sublattice A. The eigenstate

$$\chi_{\frac{1}{2},-\frac{1}{2}} = \begin{pmatrix} 0 \\ 1 \end{pmatrix} \quad (2.15)$$

is called the *pseudospin down*, corresponds to the eigenvalue  $s = -1/2$  and it is associated with the sublattice B. These eigenstates form a complete basis  $\{\chi_{\frac{1}{2},\frac{1}{2}}, \chi_{\frac{1}{2},-\frac{1}{2}}\}$  in which all the other states of the system can be expanded. E.g., the eigenstates in Eq. (2.9) of the Hamiltonian in Eq. (2.7) can be expanded in this basis:

$$\Psi_{n,\mathbf{k}} = \frac{1}{\sqrt{2}} n \chi_{\frac{1}{2},\frac{1}{2}} + \frac{1}{\sqrt{2}} e^{i\phi_{\mathbf{k}}} \chi_{\frac{1}{2},-\frac{1}{2}}, \quad (2.16)$$

Here, it is important to notice that there is a vortex ( $e^{i\phi_{\mathbf{k}}}$ ) in the momentum space in one of the pseudospin components that could potentially be mapped to the real space with a proper excitation. It is also important to notice that, because the pseudospin satisfies the usual spin algebra in Eq. (2.1), an interaction between the pseudospin degrees of freedom and the orbital degrees of freedom can be expected.

### 2.1.3 Lieb lattice

A similar analysis to the one performed for the honeycomb lattice can be performed for the Lieb lattice shown in Fig. 2.4. It is a 2D square lattice with three sublattices, denoted by A, B and C. To get the Hamiltonian, we, again, employ the tight-binding approximation [78]:

$$H_{\mathbf{k}} = -2t \begin{pmatrix} 0 & \cos k_x & 2 \cos k_x \cos k_y \\ \cos k_x & 0 & \cos k_y \\ 2 \cos k_x \cos k_y & \cos k_y & 0 \end{pmatrix}, \quad (2.17)$$

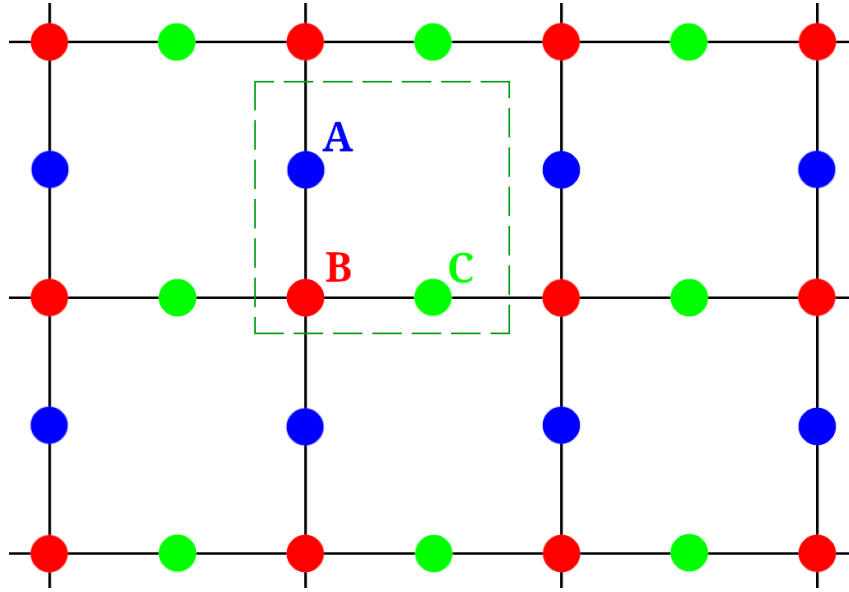


**Figure 2.4:** 2D Lieb lattice. The Lieb lattice consists of three sublattices, A, B and C. The sublattice A is marked blue, B is marked red and C is marked green. The unit cell is marked by a dashed green line.

where  $t$  is the hopping and  $\mathbf{k}$  is the crystal momentum, and the distance between the neighboring lattice sites  $a$  is immediately set to 1. The Hamiltonian is a  $3 \times 3$  matrix because there are three sublattices, and so there are three corresponding Bloch bands in the propagation constant spectrum given by:

$$\beta_{n,\mathbf{k}} = 0, \pm 2t \sqrt{\cos^2 k_x + \cos^2 k_y}. \quad (2.18)$$

The propagation constant spectrum is shown in Fig. 2.5. In the corners of the 1st Brillouin zone, we have four equivalent Dirac-like points, denoted by  $\mathbf{M}$ , that are of special interest in the context of mapping of topological singularities from the momentum space to the real space.

### 2.1.4 Pseudospin-1 system

Again, we expand the Hamiltonian around a Dirac-like point to the first order in  $\mathbf{k}$ , by setting  $\mathbf{k} \mapsto \mathbf{k} + \mathbf{M}$ , where  $\mathbf{M}$  is the reciprocal lattice vector [78]:

$$H_{\mathbf{k}+\mathbf{M}} = \kappa \begin{pmatrix} 0 & k_x & 0 \\ k_x & 0 & k_y \\ 0 & k_y & 0 \end{pmatrix}, \quad (2.19)$$

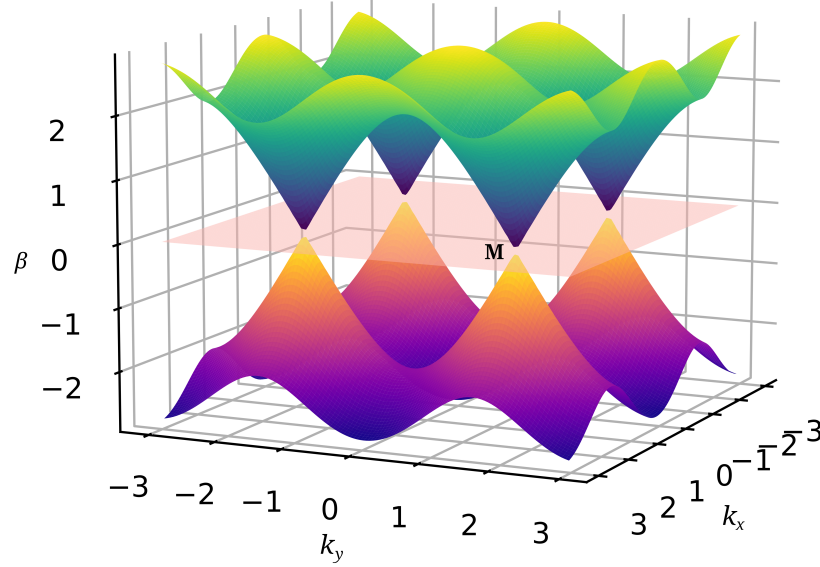


**Figure 2.5:** Lieb lattice spectrum. Because the Lieb lattice consists of three sublattices, there are three energy bands, one of them flat, in the momentum space. The bands touch at the Dirac-like points. The Dirac-like point is marked by M. The parameters  $t$  and  $a$  are taken as unity.

where  $\kappa = 2t$ . This Hamiltonian can also be expressed in terms of the pseudospin:

$$H_{\mathbf{k}} = \kappa \mathbf{S} \cdot \mathbf{k}, \quad (2.20)$$

where  $\mathbf{S} = S_x \mathbf{x} + S_y \mathbf{y}$  are:

$$S_x = \begin{pmatrix} 0 & 1 & 0 \\ 1 & 0 & 0 \\ 0 & 0 & 0 \end{pmatrix}, \quad S_y = \begin{pmatrix} 0 & 0 & 0 \\ 0 & 0 & 1 \\ 0 & 1 & 0 \end{pmatrix}. \quad (2.21)$$

Together with  $S_z$ :

$$S_z = \begin{pmatrix} 0 & 0 & -i \\ 0 & 0 & 0 \\ i & 0 & 0 \end{pmatrix}, \quad (2.22)$$

they close the pseudospin-1 algebra. It is important to notice here that  $S_z$  is not diagonal, so one sublattice can not be associated with one pseudospin. However, there are still three pseudospins because there are three sublattices. We can diagonalize  $S_z$  and work in the basis of

its eigenvectors:

$$S_z \chi_{S,s} = s \chi_{S,s}. \quad (2.23)$$

Then, the eigenvalues are  $s = -1, 0, 1$  and associated eigenvectors are:

$$\chi_{1,-1} = \frac{1}{\sqrt{2}} \begin{pmatrix} i \\ 0 \\ 1 \end{pmatrix}, \chi_{1,0} = \begin{pmatrix} 0 \\ 1 \\ 0 \end{pmatrix}, \chi_{1,1} = \frac{1}{\sqrt{2}} \begin{pmatrix} -i \\ 0 \\ 1 \end{pmatrix}. \quad (2.24)$$

In order to study the Lieb lattice in the vicinity of the Dirac-like point, we need to find the eigenvalues and the eigenvectors of the Hamiltonian in Eq. (2.19):

$$\begin{aligned} \Psi_{0,\mathbf{k}} &= \frac{1}{k} \begin{pmatrix} -k_y \\ 0 \\ k_x \end{pmatrix}, \text{ for } \beta_{0,\mathbf{k}} = 0, \\ \Psi_{\pm 1,\mathbf{k}} &= \frac{1}{k\sqrt{2}} \begin{pmatrix} k_x \\ \pm k \\ k_y \end{pmatrix}, \text{ for } \beta_{\pm 1,\mathbf{k}} = \pm \kappa k, \end{aligned} \quad (2.25)$$

where  $k \equiv \sqrt{k_x^2 + k_y^2}$ . The eigenvalues in the vicinity of the Dirac-like point are shown in Fig. 2.6. The spectrum is very similar to the spectrum of the honeycomb lattice in the vicinity of the Dirac point, that is shown in the figure 2.3. One big difference is the one additional band, that is flat and that corresponds to the eigenvalue 0. With  $k_x + ik_y = ke^{i\phi_{\mathbf{k}}}$ , we can expand the eigenmodes of the Hamiltonian in the basis of the eigenvectors of  $S_z$ ,  $\{\chi_{1,1}, \chi_{1,0}, \chi_{1,-1}\}$ :

$$\Psi_{0,\mathbf{k}} = \frac{e^{i\phi_{\mathbf{k}}}}{\sqrt{2}} \chi_{1,-1} + \frac{e^{-i\phi_{\mathbf{k}}}}{\sqrt{2}} \chi_{1,1}, \quad (2.26)$$

$$\Psi_{\pm 1,\mathbf{k}} = \pm \frac{1}{\sqrt{2}} \chi_{1,0} - ie^{i\phi_{\mathbf{k}}} \chi_{1,-1} + ie^{-i\phi_{\mathbf{k}}} \chi_{1,1}. \quad (2.27)$$

Again, there are vortices in the pseudospin components in the momentum space, that can be exploited to demonstrate the mapping of topological singularities from the momentum space to the real space. The idea is the following: We shoot a laser beam at the lattice in such a way that it excites one of the pseudospin components. We let the light propagate and check if there appear any vortices in the output in the real space, because that would mean that the vortices were mapped from the momentum space to the real space.

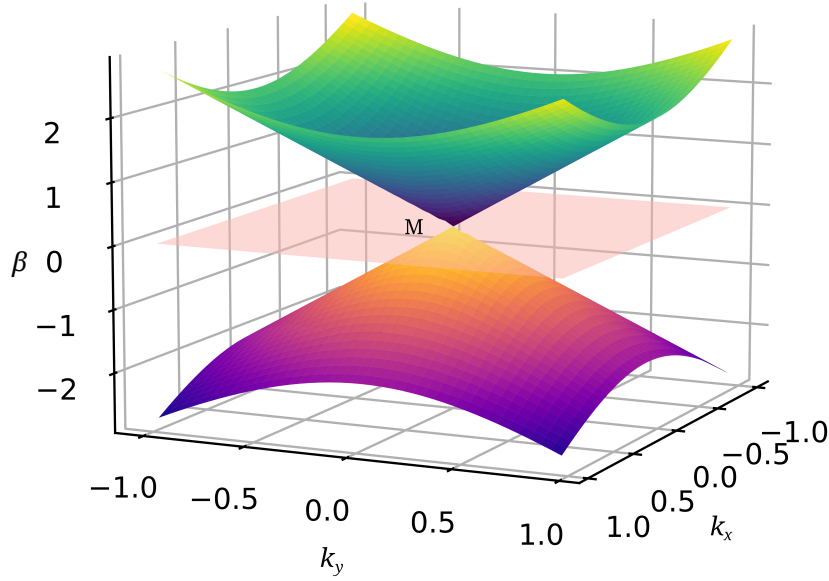


**Figure 2.6:** *Lieb lattice approximate spectrum.* Propagation constant spectrum of the Lieb lattice in the vicinity of the Dirac-like point has the shape of a cone. The Dirac-like point, located at the conical intersection, is marked with M. The parameter  $\kappa$  is 2.

Now that the stage has been set, we can move onto the experiment, performed on the honeycomb and the Lieb lattices in particular, and then the theoretical explanation for a Hamiltonian in Eq. (2.10) in general.

## 2.2 Experimental evidence of topological charge conversion

### 2.2.1 Setup for a photonic lattice

For excitations around conical intersections in both lattices, the dynamics are governed by the Hamiltonian of the form:

$$H = \kappa(S_x k_x + S_y k_y). \quad (2.28)$$

The eigenmodes of the Hamiltonian,  $H\Psi_{n,\mathbf{k}} = \beta_{n,\mathbf{k}}\Psi_{n,\mathbf{k}}$ , are organized in  $2S + 1$  bands, labeled by  $n$ , and they touch at the Dirac point. The idea behind the excitation is illustrated in Fig. 2.7. We use three vortex beams, each with an initial orbital angular momentum, also called a topological charge,  $l = 1$  or  $l = -1$ , momentum-matched to the conical intersection points for the HCL, and spatially structured so as to excite only one of the pseudospin eigenstates, either  $\chi_{1/2,1/2}$  or  $\chi_{1/2,-1/2}$ . For the Lieb lattice, we use four vortex beams to excite one of the

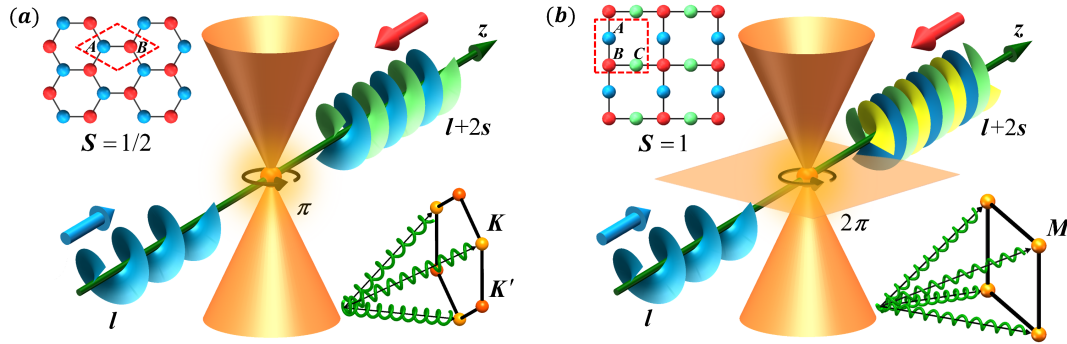


**Figure 2.7:** Illustration of the momentum-to-real-space mapping of topological singularities. (a) A pseudospin-1/2 honeycomb lattice, with two sublattices, A and B, is excited with three vortex beams, each with a topological charge  $l$ . (b) A pseudospin-1 Lieb lattice with three sublattices, A, B and C, is excited with four vortex beams. These vortex beams excite modes around the conical intersections at the corners of the Brillouin zone shown in the lower right inset. The arrows circulating around the conical intersections illustrate the winding of the Berry phase which we will show to be  $\pi$  in the honeycomb lattice and  $2\pi$  in the Lieb lattice).

pseudospin eigenstates  $\chi_{1,-1}, \chi_{1,0}$  or  $\chi_{1,1}$ . The experimental setup used to generate optically induced photonic lattices is illustrated in Fig. 2.8. A vortex beam is a laser beam that has the form [77]:

$$\psi \propto e^{im\phi} e^{-r^2} \quad (2.29)$$

and looks like a donut, as can be seen in the inset of Fig. 2.8. This choice of the excitation is very much deliberate because the eigenmodes of the Hamiltonian have vortices in the momentum space that we want to convert to the real space. Both the HCL and the Lieb lattices are created by sending a laser beam with modulated intensity pattern through a 20mm-long, negatively biased, photorefractive SBN crystal, which turns into a beam with a refractive index pattern, i.e. into the lattice, under the action of nonlinearity [45]. For the HCL, an amplitude mask is used, which turns the input beam into a triangular lattice beam, as illustrated in the inset of path 1 in Fig. 2.8. When a voltage is applied along the crystal, the lattice beam experiences a self-defocusing nonlinearity which transforms the triangular intensity pattern into the HCL index potential [45]. The spatial light modulator (SLM) is loaded with a desired phase pattern for three vortex beams, all with the same topological charge  $l$ . The probe beam forms a donut-shaped triangular lattice pattern with a net topological charge that is also equal to  $l$ . In the momentum space, the directions of three vortex beams are matched to the three Dirac points in the first Brillouin zone. In the real space, the triangular intensity pattern is matched to A

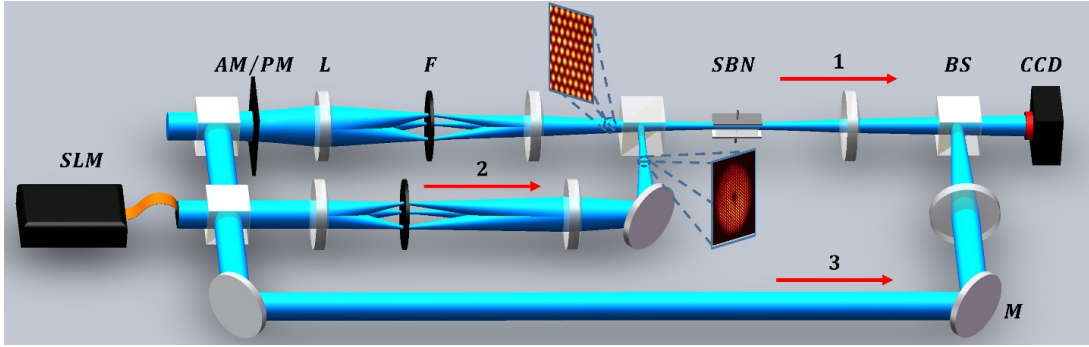


**Figure 2.8:** Experimental setup for optical induction of photonic HCL and Lieb lattices in a photorefractive crystal. SLM is the spatial light modulator. AM and PM are the amplitude mask and the phase mask. L is a lens, F is the Fourier filter, BS is a beam splitter, SBN is the strontium-barium-niobite crystal and M is a mirror. The path 1 corresponds to the ordinarily-polarized lattice-induction beam after the amplitude/phase modulation. The path 2 corresponds to the extraordinarily-polarized probe beam, i.e. the interference of multi-vortex beams created by the SLM. The path 3 corresponds to the reference beam, that is used to measure the output phase, and that is also extraordinarily-polarized. The inset in the path 1 shows a triangular (square) lattice beam pattern used to “write” the honeycomb (Lieb) photonic lattice. The inset in the path 2 shows the intensity pattern of the vortex probe beam that has the well known donut shape.

or B sublattice to selectively excite the two pseudospin states. A slightly different technique is used for the Lieb lattice. A phase mask, in this case, an SLM, is used to generate two square lattice beams with different periods;  $9\mu\text{m}$  and  $18\mu\text{m}$ . Then, the two induced index lattices are superimposed to form the Lieb lattice under the self-defocusing nonlinearity [79]. For probing, four vortex beams with same topological charge  $l$  are employed, which form a donut-shaped square lattice pattern with a net topological charge  $l$ . However, because  $S - z$  is not diagonal for pseudospin-1, the three Lieb sublattices, A, B and C do not correspond to the three pseudospin states  $\chi_{1,-1}$ ,  $\chi_{1,0}$  and  $\chi_{1,1}$ . The four vortex beams are matched to the four Dirac-like M points in the corners of 1st Brillouin zone with different phase windings. To excite the pseudospin state  $\chi_{1,0}$ , the square lattice pattern of the probe beam is matched only to the B sublattice, with a  $\pi$  phase difference between the nearest excited sites. On the other hand, to excite the pseudospin states  $\chi_{1,-1}$  and  $\chi_{1,1}$ , the square lattice pattern is matched to excite simultaneously A and C sublattices but with an opposite phase winding in a  $\pi/2$  phase step.

### 2.2.2 Topological charge conversion in the honeycomb lattice

A typical HCL lattice obtained in the experiment is shown in the Fig. 2.9. It is established with the multi-beam optical induction technique [80, 81]. The lattice remains invariant throughout

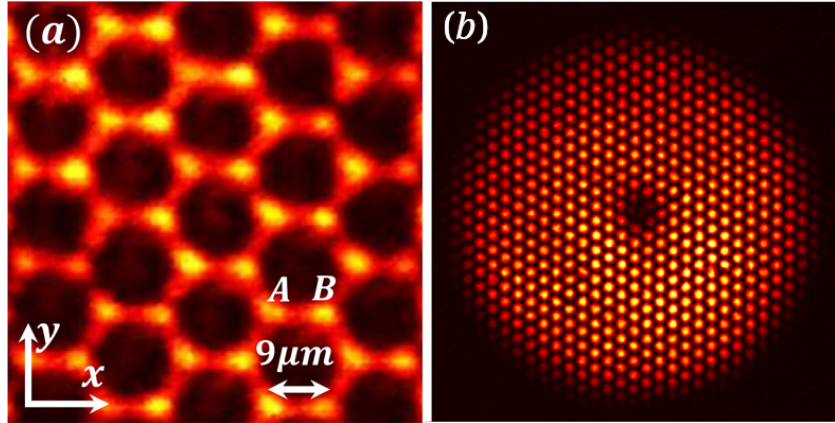


**Figure 2.9:** Photonic honeycomb lattice. (a) An optically induced honeycomb lattice. (b) The input pattern of a vortex-bearing triangular lattice beam used for selective excitation of the pseudospin states.

the crystal with a nearest neighbor spacing of  $9\mu\text{m}$ . The lattice is probed by a donut-shaped triangular lattice beam, for which the orbital angular momentum (OAM)  $l$  and pseudospin  $s$  are optimally aligned. Pseudospin component with  $s = 1/2$  is probed by a beam carrying OAM  $l = 1$ . The input is shown in the Fig. 2.9. The results for the excitation of the pseudospin component  $s = 1/2$  by a beam with  $l = 1$  are shown in the top row of Fig. 2.10. To better see the phase structure of the probe beam at the input, before the pseudospin-orbit interaction takes place, interferograms are obtained for the whole superimposed beam (all three of them together) shown in Fig. 2.10(a). The interferogram for one of the components is also shown in Fig. 2.10(b). Exactly one fork is visible in the interferogram, indicating that the topological charge is  $l = 1$ . Also, in the inset, in the lower right corner, the donut profile of the input beam is shown. In Fig. 2.10(c), the interferogram of the whole superimposed beam (all 3 of them) at the output is shown, while in Fig. 2.10(d), the interferogram of only one of the three output beams is shown. At the output, two forks are clearly visible, which means there are two vortices, i.e. that the topological charge at the output is  $l = 2$ . This indicates that there has been conversion of topological charge following the rule  $l \mapsto l + 2s$ . The forks have the same orientation, which means the vortices are of the same helicity, as indicated by the white arrows. In the lower right corner is the profile of the output beam, which is once again, a donut. In this case, the donut is somewhat deformed as compared to the input because this vortex is now a higher-order vortex which tends to disintegrate into multiple singly-charged vortices during propagation in an inhomogeneous medium [81]. In the bottom row of Fig. 2.10, we see the results for when the pseudospin component with  $s = -1/2$  is probed by a beam carrying topological charge  $l = -1$ . The first interferogram is that of the whole superimposed beams at the input. The second is that of only one of the beams. At the input, there is one fork, this time in the opposite

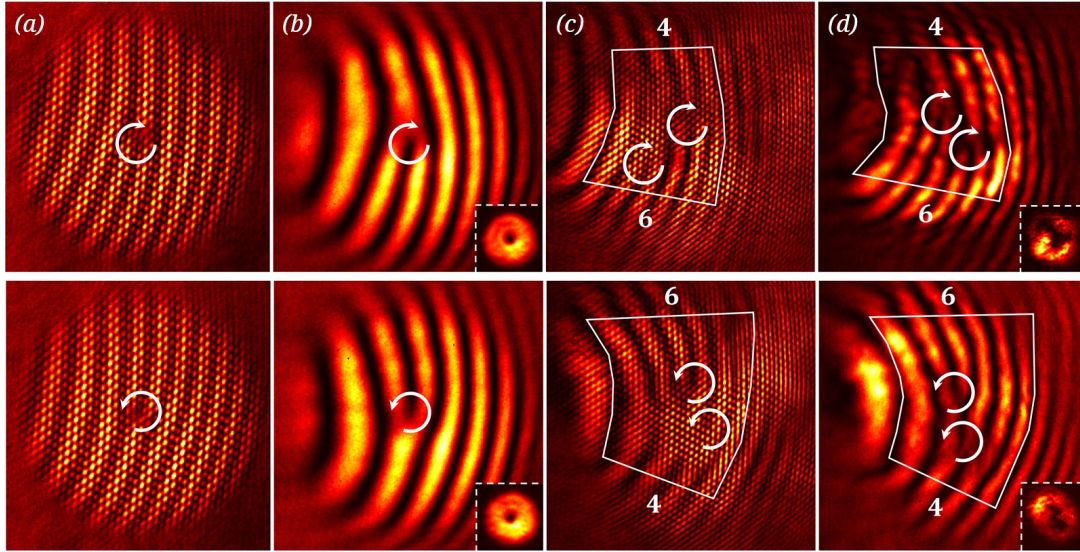


**Figure 2.10:** Excitation of pseudospin components of the HCL. In the top (bottom) row is the initial excitation of  $s = 1/2$  ( $s = -1/2$ ) pseudospin state with vortex beams of initial topological charge  $l = 1$  ( $l = -1$ ). Interferograms of (a), (b) the input and (c),(d) the output with a tilted reference beam showing topological charge conversion from 1 (-1) to 2 (-2). (a), (c) The interferogram from the whole beam, and, (b), (d) the corresponding interferograms from one of the spectral components. The number of fringes in the marked region illustrates the net topological charge at the output in (c), (d), which is by 1 (-1) more than at the input (a), (b). White curved arrows mark the position and helicity of the vortices. Insets in (b) and (d) show singly and doubly-charged vortex intensity patterns obtained at input and output, respectively.

direction, indicating that the topological charge is  $l = -1$ . In the lower right corner, there is an intensity profile of the beam in the shape of a donut. The third interferogram is that of the superimposed beams at the output, and the fourth is that of only one of the beams. Clearly, there are two forks, and, therefore two vortices, with helicities in the opposite direction of the helicities in the case  $s = 1/2$ . This means that the topological charge at the output is  $l = -2$ . In the lower right corner, there is again a deformed donut characteristic of higher order vortices. Again, we have topological charge conversion following the rule  $l \mapsto l + 2s$ .

### 2.2.3 Topological charge conversion in the Lieb lattice

A typical experiment with the Lieb lattice is shown in Fig. 2.11. The lattice is established again by optical induction in the 20-mm-long crystal, with a nearest neighbor spacing of  $9 \mu\text{m}$ . A square lattice beam in the shape of a donut is created by interfering four singly-charged vortex beams. To excite a given pseudospin state, the probing square lattice is matched either to the

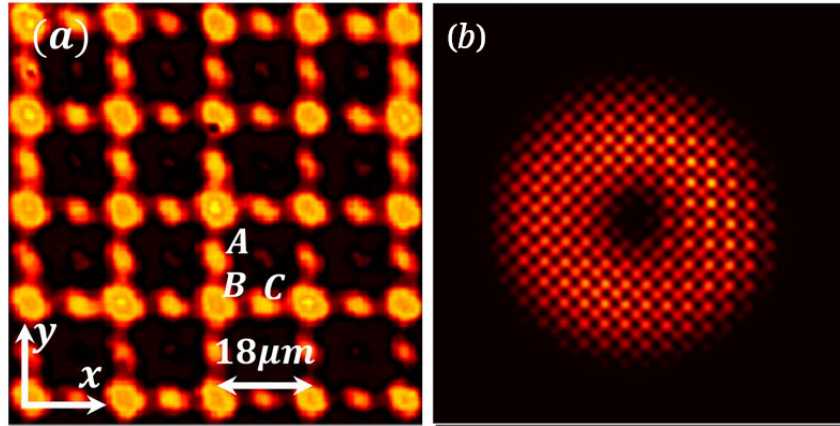


**Figure 2.11:** Photonic Lieb lattice. (a) An optically induced Lieb lattice. (b) The input pattern of a vortex-bearing square lattice beam used to excite the pseudospin states of the Lieb lattice.

B sublattice, for the  $s = 0$  pseudospin state, or the A and C sublattices with appropriate phase relation, for the  $s = 1$  and  $s = -1$  pseudospin states. Again, we first excite one of the pseudospin component,  $s = 1$  with a beam carrying topological charge  $l = 1$ , which is shown in the top row of Fig. 2.12. Here we can see the interferograms of the input with one vortex, and an output with 3 vortices. So, the topological charge has changed from 1 to 3, i.e., it also follows the rule  $l \mapsto l + 2s$ . We also excite the other pseudospin component with  $s = -1$  with a beam carrying topological charge  $l = -1$ . This can be seen in the bottom row of Fig. 2.12. At the input, there is, again, one vortex, and at the output, there are three. All the vortices have the opposite helicity than the ones from the case for  $s = 1$ ,  $l = 1$ , owing to the change in sign. Clearly, the topological charge changes from  $-1$  to  $-3$  in this case. This also follows the rule  $l \mapsto l + 2s$ .

In this section, we have seen that we can induce topological charge conversion in honeycomb and Lieb lattices with a properly designed excitation. We were also able to work out a rule for the conversion that reads:

$$l \mapsto l + 2s. \quad (2.30)$$

In the following sections we will show that this rule holds for a general hamiltonian of the form:

$$H = \kappa \mathbf{S} \cdot \mathbf{k}. \quad (2.31)$$

In the following sections, we will show that there is a fundamental topological origin for this conversion, calculate a corresponding topological invariant called the Berry phase winding, and derive a general rule for the conversion. To do this, we can start by looking at the kinematics of

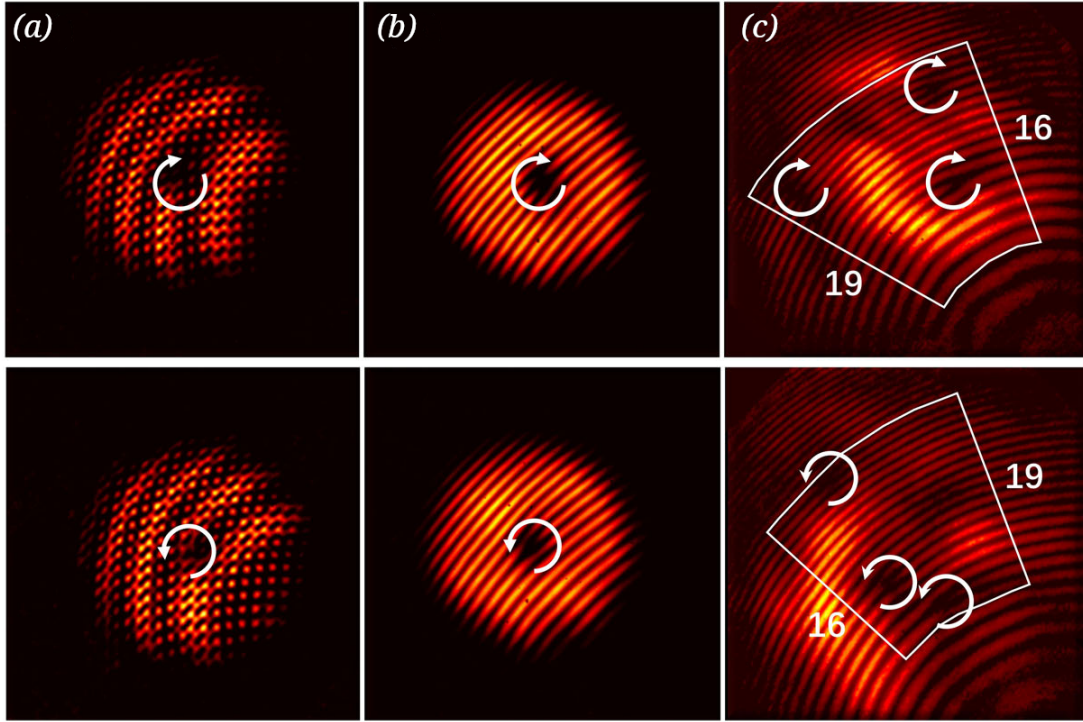


**Figure 2.12:** Excitation of pseudospin components of the Lieb lattice. The top (bottom) row shows a selective excitation of the A and C sublattices with an appropriate phase relation optimized for pseudospin state  $s = 1$  ( $s = -1$ ) by vortex beams carrying an initial topological charge  $l = 1$  ( $l = -1$ ). The interferograms of the input (a), (b) and the output (c) show a topological charge conversion from 1 to 3 (top) and from  $-1$  to  $-3$  (bottom).

the problem and the decomposition into pseudospin components.

## 2.3 Pseudospin-orbit interaction

### 2.3.1 Kinematical description of the topological charge conversion

In the previous section, we have seen that a conversion of topological charge happens when we excite the HCL or the Lieb lattice in the vicinity of a conical intersection point with a vortex beam. In this section we will provide a kinematical explanation for these observations. It is useful to restate the problem we are aim to solve: For excitations in the vicinity of conical intersection points, the dynamics is governed by the Hamiltonian

$$H = \kappa(S_x k_x + S_y k_y) = \kappa \mathbf{S} \cdot \mathbf{k} \quad (2.32)$$

where  $S_i$  are the components of the pseudospin angular momentum operator  $\mathbf{S}$ , which obey the angular momentum commutation relations:

$$[S_a, S_b] = i\epsilon_{abc}S_c, \quad (2.33)$$

where  $\epsilon_{abc}$  is the Levi-Civita tensor and  $a, b, c \in \{1, 2, 3\}$ . The constant  $\kappa$  depends on the specific properties of the lattice. The eigenstates of the pseudospin are given by:

$$S^2\chi_{s,s} = S(S+1)\chi_{s,s}, \quad (2.34)$$

$$S_z\chi_{s,s} = s\chi_{s,s}, \quad (2.35)$$

where the uppercase  $S$  is the total pseudospin and the lowercase  $s$  is the projection of the pseudospin on the  $z$ -axis. It is important to note that we perform the experiment for the HCL and Lieb lattices that are pseudospin-1/2 and pseudospin-1 system in particular, but this Hamiltonian describes a system of any half-integer or integer pseudospin in general, so, the theoretical explanation will also hold *in general*. The probe beam carries a topological charge  $l$ , i.e., it carries orbital angular momentum  $\mathbf{L} = \mathbf{r} \times \mathbf{k}$ , whose projection on the  $z$ -axis is  $l$ , with its own equivalent commutation relations:

$$[L_a, L_b] = i\epsilon_{abc}L_c. \quad (2.36)$$

Because the Hamiltonian has the form of  $\propto \mathbf{S} \cdot \mathbf{k}$ , a pseudospin-orbit interaction is to be expected. The following commutation relations hold:

$$[S_a, L_b] = [S_a, k_b] = 0, \quad (2.37)$$

because  $\mathbf{S}$  and  $\mathbf{L}$  (or  $\mathbf{k}$ ) live in different vector spaces, and, by using the definition for  $\mathbf{L}$ , it is easy to show that:

$$[k_a, L_b] = i\epsilon_{abc}k_c. \quad (2.38)$$

We are interested in how the total angular momentum  $\mathbf{J} = \mathbf{L} + \mathbf{S}$  behaves. Because both the pseudospin and the orbital angular momentum are in the  $z$ -direction, it is enough to check how the projection of the total angular momentum on the  $z$  axis,  $J_z$ , behaves. To do that, we look at

the commutator  $[H, J_z]$ :

$$\begin{aligned} \frac{1}{\kappa} [H, J_z] &= [(S_x k_x + S_y k_y), L_z + S_z] = \\ &= S_x [k_x, L_z] + [S_x, L_z] k_x + S_y [k_y, L_z] \\ &+ [S_y, L_z] k_y + S_x [k_x, S_z] + [S_x, S_z] k_x + S_y [k_y, S_z] + [S_y, S_z] k_y. \end{aligned} \quad (2.39)$$

By using Eq. (2.33) and Eq. (2.36–2.38), we have:

$$\frac{1}{\kappa} [H, J_z] = -iS_x k_y + 0 + iS_y k_x + 0 + 0 - iS_y k_x + 0 + iS_x k_y = 0, \quad (2.40)$$

i.e.  $[H, J_z] = 0$ , which means that the total angular momentum is conserved. The initial excitation in all experiments is comprised of a single value of  $l$  and  $s$ , and the optimally aligned initial condition implies a maximal value of  $|l + s|$ . Because the total angular momentum is conserved, and because we know the initial values of  $l$  and  $s$  (because we chose them), we can work out the values  $l'$  and the  $s'$ :

$$l + s = l' + s'. \quad (2.41)$$

At the output, the usual selection rule  $s' \in [-S, S]$  applies, i.e. all the values of  $s'$  between  $-S$  and  $S$  are permitted. From that we can work out the topological charge  $l' = l + s - s'$  at the output.

### 2.3.2 Kinematics in the honeycomb lattice

For the HCL; if, at the input, we excite the pseudospin component  $s = 1/2$  with a beam carrying  $l = 1$ , at the output, both  $s' = 1/2$  and  $s' = -1/2$  are permitted. For the  $s' = 1/2$  component, the topological charge will be  $s' = 1 + 1/2 - 1/2 = 1$ , i.e., for this component, the topological charge stays the same. For the  $s' = -1/2$  component, the topological charge will be  $s' = 1 + 1/2 - (-1/2) = 2$ , i.e. for this component, the topological charge in the pseudospin component that was not excited, increases by 1. Later, by looking at the dynamics of the problem, we will see that this increase comes from the mapping of a vortex from the momentum space to the real space and that it has a topological origin. But for now, let us give the breakdown of the topological charge conversion for other cases. The cases for the honeycomb lattice are shown in Fig. 2.13. The experimental observations are further corroborated by numerical simulations based on the paraxial wave equation (2.3). We excite the pseudospin states  $s = 1/2$  and  $s = -1/2$  by an input beam with topological charge  $l = 1$  covering sublattices A

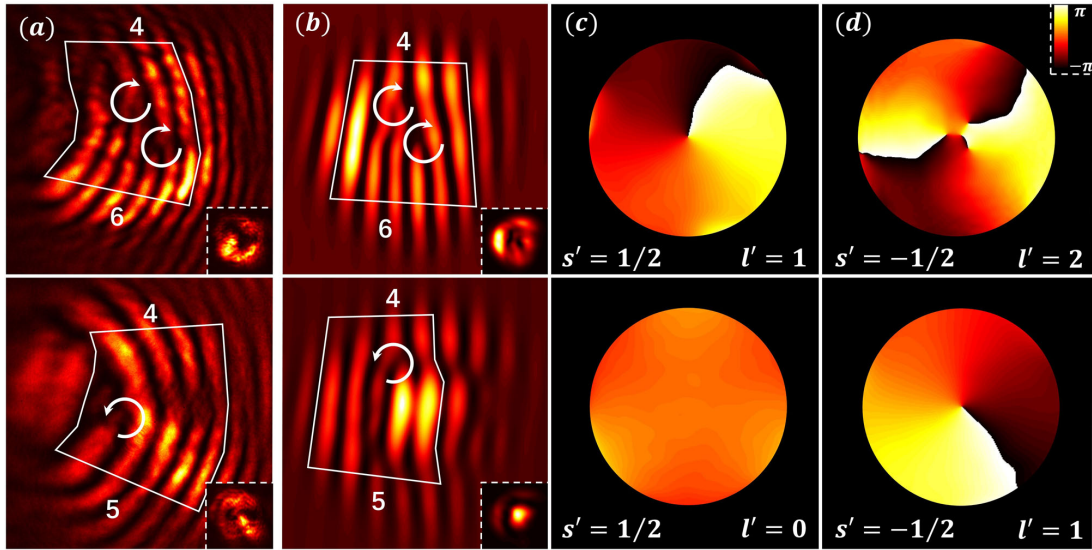


**Figure 2.13:** *Pseudospin decomposition in the HCL.* In the top row, the pseudospin state  $s = 1/2$  is selectively excited by an initial beam that carries the topological charge  $l = 1$ . In the bottom row, the pseudospin state  $s = -1/2$  is selectively excited by an initial beam carries the same topological charge  $l = 1$ . In (a), we have the output interferogram from the experiment, and in (b), the corresponding results from the simulation. (c) and (d) show the evolved phase structure for each of the pseudospin components. The topological charge increases (decreases) by 1 in the initially unexcited component as can be seen in the top (bottom) panel of (d). The topological charge in the initially excited component remains intact can be seen in (c). The insets in the lower right corner in (a) and (b) are the corresponding intensity patterns. The donut corresponds to  $l \neq 0$  component. A central bright spot corresponds to the  $l = 0$  component.

and B, respectively. In numerical simulations, the output field is decomposed into each pseudospin component. From the phase structure of each component, the difference is clear: If the  $s = 1/2$  component is initially excited, the unexcited,  $s' = -1/2$ , component is converted into an  $l' = 2$  vortex. In contrast, if the  $s = -1/2$  is initially excited, the vorticity in the unexcited,  $s' = 1/2$ , component disappears, i.e.  $l' = 0$ . The vorticity of the initially excited component always remains unchanged. Note that the output intensity patterns in the lower right insets of Fig. 2.13 have a subtle difference between the two cases of excitation: the donut is preserved in the top panels when both components maintain a vortex, but deforms into a bright central spot in bottom panels when vortex annihilation occurs in one of the components.

### 2.3.3 Kinematics in the Lieb lattice

In Fig. 2.14, we show experimental and numerical results for the Lieb lattice obtained by the initial excitation of the pseudospin states  $s = 1$ ,  $s = 0$ , and  $s = -1$  with an input beam with

topological charge  $l = 1$ , and we examine how the phase evolves for the three decomposed pseudospin components. If we excite the  $s = 1$  component, the topological charge emerging

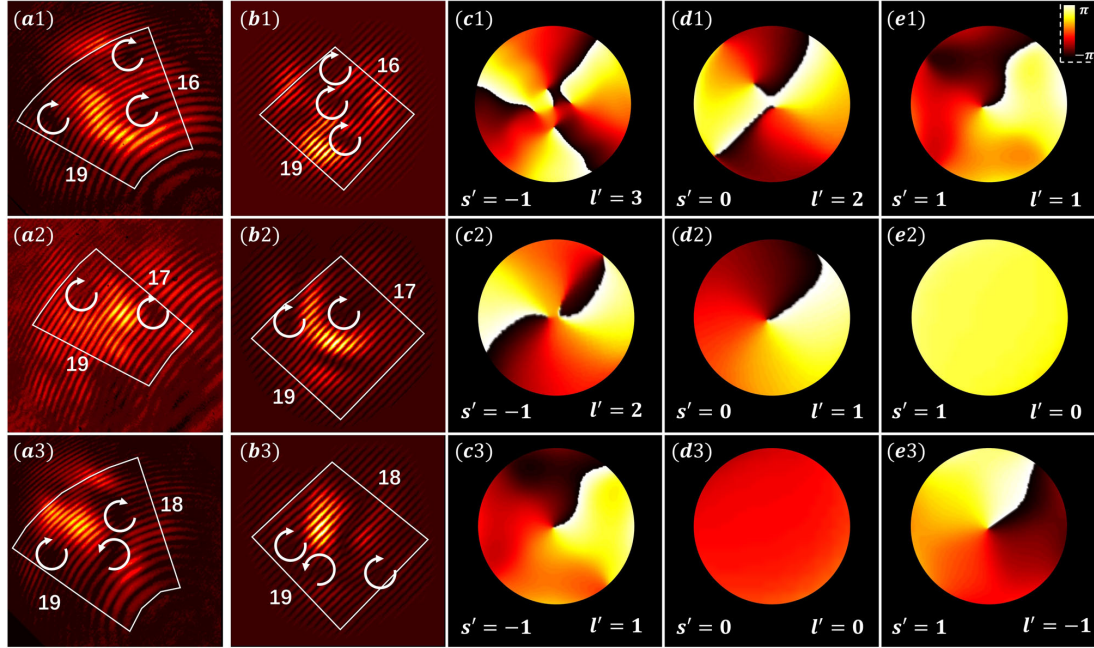


**Figure 2.14:** *Pseudospin decomposition in the Lieb lattice.* Results from the experiment and the simulation for initial excitations of the pseudospin states  $s = 0$  in (a1)–(e1),  $s = 1$  in (a2)–(e2) and  $s = -1$  in (a3)–(e3), by four input beams of topological charge  $l = 1$  are shown. Output interferograms from (a) the experiment and (b) the simulation show different topological charge conversions under different excitation conditions. (c)–(e) show the output phase structure of the probe beam, numerically decomposed for each pseudospin component  $s'$ , where corresponding output vorticity  $l'$  has been identified in each component. In all of the cases, each pseudospin component obeys Eq. (2.41).

in the  $s' = -1$  pseudospin component is  $l' = 3$ . This case corresponds to optimally aligned excitation in Fig. 2.12. For the other two cases,  $s = 0$ , and  $s = -1$ , which are not optimally aligned, the initial vortex is transformed into multiple vortices with a net topological charge of 2 (the middle row in Fig. 2.14) or 1 (the bottom row in Fig. 2.14). Again, the increase in the topological charge happens in the unexcited components, and, again, by looking at the dynamics of the problem, we will see that this increase comes from the mapping of a vortex from the momentum space to the real space. Similar studies, with an input beam with a topological charge  $l = -1$ , lead to the same conversion rule. One more peculiar detail is worth mentioning here: The pseudospin components of the Lieb lattice are not diagonal in the sublattice basis, and, so, they do not have a trivial correspondence to a particular sublattice, as is the case for the pseudospin-1/2 HCL. In fact, the physics of pseudospin-orbit interaction in Lieb lattices is, in one aspect, richer than that of polarization-based spin-orbit interaction: Here we have also

excited the  $s = 0$  pseudospin state which is inadmissible for the helicity of photons due to its zero mass.

## 2.4 Mapping of vortices from the momentum space to the real space

### 2.4.1 Dynamics in the honeycomb lattice

Up to this point, we have discussed topological charge conversion in the honeycomb and the Lieb lattices and explained the results kinematically via the conservation of angular momentum. The observed phenomenon can also be explained dynamically. The idea is to solve the propagation equation (2.3) by expanding the initial excitation  $\psi_{l,s}$  in the eigenmodes of the Hamiltonian  $H = \kappa \mathbf{S} \cdot \mathbf{k}$  given by Eq. (2.9):

$$\psi_{n,\mathbf{k}} = \frac{1}{\sqrt{2}} \left( n \chi_{S=\frac{1}{2},s=\frac{1}{2}} + e^{i\varphi_{\mathbf{k}}} \chi_{S=\frac{1}{2},s=-\frac{1}{2}} \right), \quad (2.42)$$

where the  $\chi_{S,s}$  are the eigenstate of  $S_z$ , and then to evolve it with the propagation constants given by Eq. (2.8):

$$\beta_{n,\mathbf{k}} = n \frac{\kappa}{2} k, \quad (2.43)$$

where  $n = \pm 1$ . Because we set  $k_x + ik_y = ke^{i\varphi_{\mathbf{k}}}$ , i.e. we have switched to the polar coordinate system in the momentum space, the form of the eigenmodes given by Eq. (2.42) is especially suitable because it clearly shows there is a vortex in one of the pseudospin components in the momentum space. The complex amplitude of the electric field of the initial excitation is:

$$\psi_{l,s}(r, \varphi_{\mathbf{r}}, z = 0) = \psi_0 r^l e^{il\varphi_{\mathbf{r}}} \exp\left(-\frac{r^2}{a_0^2}\right) \chi_{S,s}, \quad (2.44)$$

where  $\psi_0$  is the normalization constant,  $x + iy = re^{i\varphi_{\mathbf{r}}}$ , and  $a_0$  is the width of the laser beam in the real space. We can rewrite the initial excitation in terms of variables in the momentum space by using a Fourier transform:

$$\psi_{l,s}(r, \varphi_{\mathbf{r}}, z = 0) = \psi_0 \int d^2k \frac{1}{\sqrt{A}} \chi_{S,s} f_l(\mathbf{k}) e^{i\mathbf{k} \cdot \mathbf{r}}, \quad (2.45)$$

where  $A$  is the area of one hexagonal plaque of the HCL in the real space and the integral is taken over the whole momentum space. The function  $f_l(\mathbf{k})$  depends on the transverse profile and the phase structure of the initial excitation and it is equal to:

$$f(\mathbf{k}) = (k_x + ik_y)^l \exp\left(-\frac{k_x^2 + k_y^2}{k_F^2}\right) = k^l e^{il\varphi_{\mathbf{k}}} \exp\left(-\frac{k^2}{k_F^2}\right), \quad (2.46)$$

where  $k_F$  defines the width of the beam in the momentum space. For a given  $l$ , there are two possible initial excitations;  $\Psi_{l,s=\frac{1}{2}}$ , which denotes that we have excited the pseudospin up by a beam with topological charge  $l$ , and  $\Psi_{l,s=-\frac{1}{2}}$ , which denotes that we have excited the pseudospin down with the topological charge  $l$ . These initial excitations can be written as a superposition of the eigenmodes of the Hamiltonian:

$$\Psi_{l,s=\frac{1}{2}}(r, \varphi_{\mathbf{r}}, z=0) = \sum_n \int d^2k \langle \Psi_{n,\mathbf{k}} | \Psi_{l,s=\frac{1}{2}}(r, \varphi_{\mathbf{r}}, z=0) \rangle \Psi_{n,\mathbf{k}}, \quad (2.47)$$

$$\Psi_{l,s=-\frac{1}{2}}(r, \varphi_{\mathbf{r}}, z=0) = \sum_n \int d^2k \langle \Psi_{n,\mathbf{k}} | \Psi_{l,s=-\frac{1}{2}}(r, \varphi_{\mathbf{r}}, z=0) \rangle \Psi_{n,\mathbf{k}}. \quad (2.48)$$

The scalar products of the initial wavepacket with the eigenmodes are easily evaluated:

$$\langle \Psi_{n,\mathbf{k}} | \Psi_{l,s=\frac{1}{2}}(r, \varphi_{\mathbf{r}}, z=0) \rangle = \Psi_0 \frac{n}{\sqrt{2}} f_l(\mathbf{k}), \quad (2.49)$$

$$\langle \Psi_{n,\mathbf{k}} | \Psi_{l,s=-\frac{1}{2}}(r, \varphi_{\mathbf{r}}, z=0) \rangle = \Psi_0 \frac{e^{-i\varphi_{\mathbf{k}}}}{\sqrt{2}} f_l(\mathbf{k}). \quad (2.50)$$

The initial states are then:

$$\Psi_{l,s=\frac{1}{2}}(r, \varphi_{\mathbf{r}}, z=0) = \Psi_0 \sum_n \int d^2k \frac{1}{2\sqrt{A}} \begin{pmatrix} 1 \\ ne^{i\varphi_{\mathbf{k}}} \end{pmatrix} e^{i\mathbf{k}\cdot\mathbf{r}} f_l(\mathbf{k}), \quad (2.51)$$

$$\Psi_{l,s=-\frac{1}{2}}(r, \varphi_{\mathbf{r}}, z=0) = \Psi_0 \sum_n \int d^2k \frac{1}{2\sqrt{A}} \begin{pmatrix} ne^{-i\varphi_{\mathbf{k}}} \\ 1 \end{pmatrix} e^{i\mathbf{k}\cdot\mathbf{r}} f_l(\mathbf{k}). \quad (2.52)$$

The eigenmodes in the honeycomb lattice evolve dynamically, each one with its own propagation constant  $\beta_{n,\mathbf{k}} = n\kappa k/2$ :

$$\Psi_{l,s=\frac{1}{2}}(r, \varphi_{\mathbf{r}}, z) = \Psi_0 \sum_n \int d^2k \frac{1}{2\sqrt{A}} \begin{pmatrix} 1 \\ ne^{i\varphi_{\mathbf{k}}} \end{pmatrix} e^{i\mathbf{k}\cdot\mathbf{r} - in\beta_0 k z} f_l(\mathbf{k}), \quad (2.53)$$

$$\Psi_{l,s=-\frac{1}{2}}(r, \varphi_{\mathbf{r}}, z) = \Psi_0 \sum_n \int d^2k \frac{1}{2\sqrt{A}} \begin{pmatrix} ne^{-i\varphi_{\mathbf{k}}} \\ 1 \end{pmatrix} e^{i\mathbf{k}\cdot\mathbf{r} - in\beta_0 k z} f_l(\mathbf{k}), \quad (2.54)$$

where  $\beta_0 = \kappa/2$ . After a sufficiently long time of propagation, we get the far field dynamics. Without loss of generality, we can assume that we have excited pseudospin  $s = 1/2$ ; the analysis is the same for the other component. The trick is to expand the spinor in Eq. (2.53) in terms of the pseudospin eigenstates  $\chi_{S,s}$ . The evolving complex amplitude of the electric field is then given by:

$$\begin{aligned} \Psi_{l,s=\frac{1}{2}}(r, \varphi_{\mathbf{r}}, z) &= \frac{\Psi_0}{2\sqrt{A}} \sum_{n=\pm 1} \int d^2k f_l(\mathbf{k}) \chi_{\frac{1}{2}, \frac{1}{2}} e^{i\mathbf{k}\cdot\mathbf{r} - in\beta_0 kz} + \\ &+ \frac{\Psi_0}{2\sqrt{A}} \sum_{n=\pm 1} \int d^2k n e^{i\varphi_{\mathbf{k}}} f_l(\mathbf{k}) \chi_{\frac{1}{2}, -\frac{1}{2}} e^{i\mathbf{k}\cdot\mathbf{r} - in\beta_0 kz} \end{aligned} \quad (2.55)$$

After taking the sum over the band index  $n = \pm 1$ , we get:

$$\begin{aligned} \Psi_{l,s=\frac{1}{2}}(r, \varphi_{\mathbf{r}}, z) &= \frac{\Psi_0}{\sqrt{A}} \int_0^{2\pi} \int_0^\infty d\varphi_{\mathbf{k}} k dk f_l(\mathbf{k}) \chi_{\frac{1}{2}, \frac{1}{2}} e^{i\mathbf{k}\cdot\mathbf{r}} \cos(\beta_0 kz) + \\ &\frac{-\Psi_0}{\sqrt{A}} \int_0^{2\pi} \int_0^\infty d\varphi_{\mathbf{k}} k dk f_l(\mathbf{k}) e^{i\varphi_{\mathbf{k}}} \chi_{\frac{1}{2}, -\frac{1}{2}} e^{i\mathbf{k}\cdot\mathbf{r}} i \sin(\beta_0 kz). \end{aligned} \quad (2.56)$$

After substituting  $f(\mathbf{k})$  and  $\mathbf{k} \cdot \mathbf{r} = kr \cos(\varphi_{\mathbf{k}} - \varphi_{\mathbf{r}})$ , we get:

$$\begin{aligned} \Psi_{l,s=\frac{1}{2}}(r, \varphi_{\mathbf{r}}, z) &= \frac{\Psi_0}{\sqrt{A}} \chi_{\frac{1}{2}, \frac{1}{2}} \int_0^{2\pi} \int_0^\infty d\varphi_{\mathbf{k}} dk k^{l+1} e^{il\varphi_{\mathbf{k}}} e^{-\frac{k^2}{k_F^2}} e^{ikr \cos(\varphi_{\mathbf{k}} - \varphi_{\mathbf{r}})} \cos(\beta_0 kz) + \\ &\frac{-\Psi_0}{\sqrt{A}} \chi_{\frac{1}{2}, -\frac{1}{2}} \int_0^{2\pi} \int_0^\infty d\varphi_{\mathbf{k}} dk k^{l+1} e^{il\varphi_{\mathbf{k}}} e^{-\frac{k^2}{k_F^2}} e^{i\varphi_{\mathbf{k}}} e^{ikr \cos(\varphi_{\mathbf{k}} - \varphi_{\mathbf{r}})} i \sin(\beta_0 kz) \end{aligned} \quad (2.57)$$

One final, and most important trick, is to change the variable of integration from  $\varphi_{\mathbf{k}}$  to  $\varphi = \varphi_{\mathbf{k}} - \varphi_{\mathbf{r}}$  to get:

$$\begin{aligned} \Psi_{l,s=\frac{1}{2}} &= \frac{\Psi_0}{\sqrt{A}} e^{il\varphi_{\mathbf{r}}} \chi_{\frac{1}{2}, \frac{1}{2}} \int_0^{2\pi} \int_0^\infty d\varphi dk k^{l+1} e^{il\varphi} e^{-k^2/k_F^2} e^{ikr \cos(\varphi)} \cos(\beta_0 kz) + \\ &\frac{-\Psi_0}{\sqrt{A}} e^{i(l+1)\varphi_{\mathbf{r}}} \chi_{\frac{1}{2}, -\frac{1}{2}} \int_0^{2\pi} \int_0^\infty d\varphi dk k^{l+1} e^{i(l+1)\varphi} e^{-k^2/k_F^2} e^{ikr \cos(\varphi)} i \sin(\beta_0 kz) \end{aligned}, \quad (2.58)$$

which shows us that the topological charge in the excited component stayed the same, while the increase in topological charge,  $l \mapsto l + 2s = l + 2 \cdot 1/2 = l + 1$  occurred in the unexcited component of the pseudospin. Notice how the additional topological charge  $l + 1$  appeared in the real space, i.e. that it has the form  $(l + 1)\varphi_{\mathbf{r}}$ , because it was mapped from the momentum space; from  $1 \cdot \varphi_{\mathbf{k}}$ . It is also extremely important to notice that this happened in the unexcited component because that means that the increase of the topological can only possibly be explained via a mapping of a topological singularity from the momentum space to the real space,

a fact we will show by calculating the Berry phase winding in the following section. To clarify the mathematical structure of the output, we introduce the *g-functions* defined by:

$$g_{\frac{1}{2},\frac{1}{2}}^{(l)}(r,z) = \frac{\Psi_0}{\sqrt{A}} \int_0^{2\pi} \int_0^\infty d\varphi dk k^{l+1} e^{il\varphi} e^{-k^2/k_F^2} e^{ikr\cos(\varphi)} \cos(\beta_0 kz) \quad (2.59)$$

$$g_{\frac{1}{2},-\frac{1}{2}}^{(l)}(r,z) = \frac{-\Psi_0}{\sqrt{A}} \int_0^{2\pi} \int_0^\infty d\varphi dk k^{l+1} e^{i(l+1)\varphi} e^{-k^2/k_F^2} e^{ikr\cos(\varphi)} i \sin(\beta_0 kz), \quad (2.60)$$

which contain the radial and z-dependence of the optical field. This leads us to:

$$\Psi_{l,s=\frac{1}{2}}(\mathbf{r},z) = e^{il\varphi_r} \chi_{\frac{1}{2},\frac{1}{2}} g_{\frac{1}{2},\frac{1}{2}}^{(l)}(r,z) + e^{i(l+1)\varphi_r} \chi_{\frac{1}{2},-\frac{1}{2}} g_{\frac{1}{2},-\frac{1}{2}}^{(l)}(r,z), \quad (2.61)$$

where it is now obvious that the topological charge increased by 1 in the unexcited pseudospin component according to the rule:

$$l \mapsto l + 2s, \quad (2.62)$$

$s = 1/2$ . The profiles of the *g-functions* are shown in Fig. 2.15. Each is the profile of a donut.

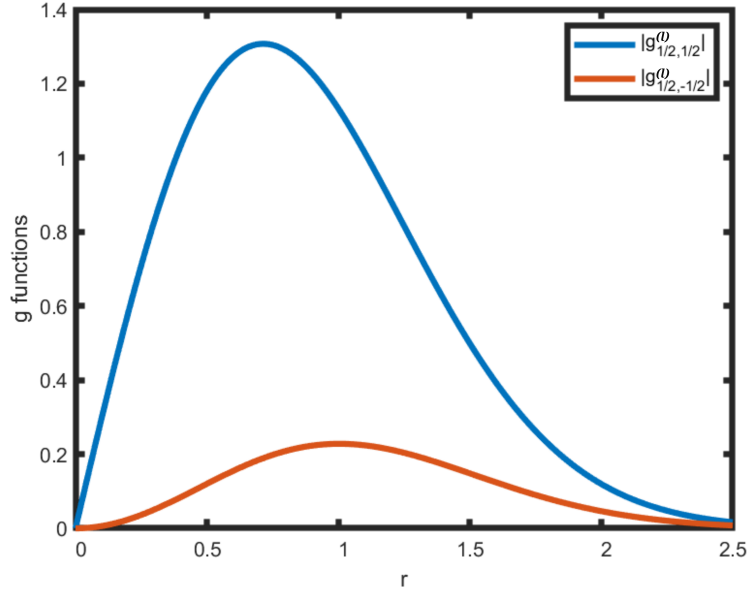


**Figure 2.15:** Profiles of the HCL *g-functions*. The total beam intensity, obtained numerically, at the output has a donut-shaped structure as expected for conical diffraction. The parameters  $\Psi_0$ ,  $A$ ,  $k_F$  and  $\kappa$  are taken as unity,  $l = 1$  and  $z = 0.2$ .

The intensity of the *g-functions* is shown in Fig. 2.16.

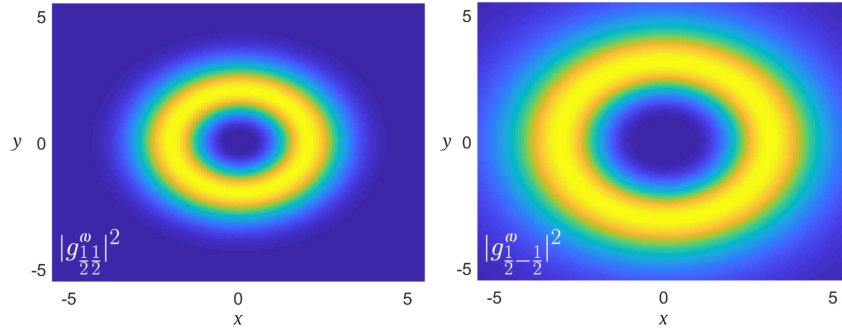


**Figure 2.16:** Intensity of the HCL  $g$ -functions. The intensities of both of the  $g$ -functions have the shape of a donut. Numerically we can infer that, because the  $g$ -function  $g_{\frac{1}{2}, \frac{1}{2}}$  has  $l = 1$  and the  $g$ -function  $g_{\frac{1}{2}, -\frac{1}{2}}$  has  $l + 1 = 2$ , the donut on the left is smaller than the donut on the right.

## 2.4.2 Dynamics in the Lieb lattice

In the previous section, we have analyzed the dynamics of the honeycomb lattice. In this section, we repeat a similar analysis for the Lieb lattice. The Hamiltonian has the same form,  $H = \mathbf{S} \cdot \mathbf{k}$ . The eigenstates are given by Eq. (2.26), which we repeat here:

$$\Psi_{0, \mathbf{k}} = \frac{e^{i\varphi_{\mathbf{k}}}}{\sqrt{2}} \chi_{1, -1} + \frac{e^{-i\varphi_{\mathbf{k}}}}{\sqrt{2}} \chi_{1, 1}, \quad (2.63)$$

$$\Psi_{\pm 1, \mathbf{k}} = \pm \frac{1}{\sqrt{2}} \chi_{1, 0} - ie^{i\varphi_{\mathbf{k}}} \chi_{1, -1} + ie^{-i\varphi_{\mathbf{k}}} \chi_{1, 1}. \quad (2.64)$$

where  $\chi_{S, s}$  are now the eigenstates of  $S_z$  for a pseudospin-1 system. The corresponding eigenvalues are:

$$\beta_{n, \mathbf{k}} = n\kappa k, \quad (2.65)$$

for  $n = 0, \pm 1$  and  $k = \sqrt{k_x^2 + k_y^2}$ . The initial excitation is given by:

$$\Psi_{l, S}(r, \varphi_{\mathbf{r}}, z = 0) = \Psi_0 \int d^2k \frac{1}{\sqrt{A}} \chi_{S, s} f_l(\mathbf{k}) e^{i\mathbf{k} \cdot \mathbf{r}}, \quad (2.66)$$

where  $f_l(\mathbf{k}) = k^l \exp(il\varphi_{\mathbf{k}}) \exp(-k^2/k_F^2)$  is the same like the one in the case of the honeycomb lattice and  $A$  is the area of one square plaque of the Lieb lattice. For a given  $l$ , there are three possible initial conditions;  $\Psi_{l, s=1}$ ,  $\Psi_{l, s=-1}$  and  $\Psi_{l, s=0}$ . Again, without loss of generality, we can

focus on only one of them, and we can expand it in the eigenstates of the Hamiltonian:

$$\Psi_{l,s=1}(r, \Phi_{\mathbf{r}}, z=0) = \sum_n \int d^2k \langle \Psi_{n,\mathbf{k}} | \Psi_{l,s=1}(r, \Phi_{\mathbf{r}}, z=0) \rangle \Psi_{n,\mathbf{k}} \quad (2.67)$$

The scalar products are easily worked out by plugging in the expressions for the eigenmodes and the initial excitation:

$$\langle \Psi_{0,\mathbf{k}} | \Psi_{l,s=1}(r, \Phi_{\mathbf{r}}, z=0) \rangle = \Psi_0 \frac{1}{\sqrt{2}} f_l(\mathbf{k}) e^{i\Phi_{\mathbf{k}}}, \quad (2.68)$$

$$\langle \Psi_{\pm 1,\mathbf{k}} | \Psi_{l,s=1}(r, \Phi_{\mathbf{r}}, z=0) \rangle = \Psi_0 \frac{-i}{2} f_l(\mathbf{k}) e^{i\Phi_{\mathbf{k}}}. \quad (2.69)$$

The initial state is then:

$$\begin{aligned} \Psi_{l,s=1}(r, \Phi_{\mathbf{r}}, z=0) &= \int d^2k \left( \Psi_0 \frac{1}{\sqrt{2}} f_l(\mathbf{k}) e^{i\Phi_{\mathbf{k}}} \right) \frac{1}{\sqrt{A}} \frac{1}{k} \begin{pmatrix} -k_y \\ 0 \\ k_x \end{pmatrix} e^{i\mathbf{k}\cdot\mathbf{r}} + \\ &+ \sum_{n=\pm 1} \int d^2k \left( \Psi_0 \frac{-i}{2} f_l(\mathbf{k}) e^{i\Phi_{\mathbf{k}}} \right) \frac{1}{\sqrt{A}} \frac{1}{k\sqrt{2}} \begin{pmatrix} k_x \\ nk \\ k_y \end{pmatrix} e^{i\mathbf{k}\cdot\mathbf{r}}. \end{aligned} \quad (2.70)$$

The eigenmodes evolve dynamically with the propagation constant  $n\kappa$ :

$$\begin{aligned} \Psi_{l,s=1}(r, \Phi_{\mathbf{r}}, z) &= \int d^2k \left( \Psi_0 \frac{1}{\sqrt{2}} f_l(\mathbf{k}) e^{i\Phi_{\mathbf{k}}} \right) \frac{1}{\sqrt{A}} \frac{1}{k} \begin{pmatrix} -k_y \\ 0 \\ k_x \end{pmatrix} e^{i\mathbf{k}\cdot\mathbf{r}} + \\ &+ \sum_{n=\pm 1} \int d^2k \left( \Psi_0 \frac{-i}{2} f_l(\mathbf{k}) e^{i\Phi_{\mathbf{k}}} \right) \frac{1}{\sqrt{A}} \frac{1}{k\sqrt{2}} \begin{pmatrix} k_x \\ nk \\ k_y \end{pmatrix} e^{i\mathbf{k}\cdot\mathbf{r} - in\kappa kz}. \end{aligned} \quad (2.71)$$

In order to make progress, the trick we use in this case is:

$$\frac{k_y}{k} = \frac{e^{i\Phi_{\mathbf{k}}} - e^{-i\Phi_{\mathbf{k}}}}{2i}, \quad \frac{k_x}{k} = \frac{e^{i\Phi_{\mathbf{k}}} + e^{-i\Phi_{\mathbf{k}}}}{2}. \quad (2.72)$$

By using this, we get:

$$\begin{aligned} \Psi_{l,s=1}(r, \varphi_{\mathbf{r}}, z) &= \int d^2k \left( \Psi_0 \frac{1}{\sqrt{2}} f_l(\mathbf{k}) e^{i\varphi_{\mathbf{k}}} \right) \frac{1}{\sqrt{A}} \begin{pmatrix} -\frac{e^{i\varphi_{\mathbf{k}}} - e^{-i\varphi_{\mathbf{k}}}}{2i} \\ 0 \\ \frac{e^{i\varphi_{\mathbf{k}}} + e^{-i\varphi_{\mathbf{k}}}}{2} \end{pmatrix} e^{i\mathbf{k} \cdot \mathbf{r}} + \\ &+ \sum_{n=\pm 1} \int d^2k \left( \Psi_0 \frac{-i}{2} f_l(\mathbf{k}) e^{i\varphi_{\mathbf{k}}} \right) \frac{1}{\sqrt{A}} \frac{1}{\sqrt{2}} \begin{pmatrix} \frac{e^{i\varphi_{\mathbf{k}}} + e^{-i\varphi_{\mathbf{k}}}}{2} \\ n \\ \frac{e^{i\varphi_{\mathbf{k}}} - e^{-i\varphi_{\mathbf{k}}}}{2i} \end{pmatrix} e^{i\mathbf{k} \cdot \mathbf{r} - in\kappa kz} \end{aligned} \quad (2.73)$$

Next, the column matrices are expressed in terms of the pseudospin eigenstates:

$$\begin{aligned} \begin{pmatrix} -\frac{e^{i\varphi_{\mathbf{k}}} - e^{-i\varphi_{\mathbf{k}}}}{2i} \\ 0 \\ \frac{e^{i\varphi_{\mathbf{k}}} + e^{-i\varphi_{\mathbf{k}}}}{2} \end{pmatrix} &= \frac{e^{i\varphi_{\mathbf{k}}}}{2} \begin{pmatrix} i \\ 0 \\ 1 \end{pmatrix} + \frac{e^{-i\varphi_{\mathbf{k}}}}{2} \begin{pmatrix} -i \\ 0 \\ 1 \end{pmatrix} = \frac{e^{i\varphi_{\mathbf{k}}}}{\sqrt{2}} \chi_{1,-1} + \frac{e^{-i\varphi_{\mathbf{k}}}}{\sqrt{2}} \chi_{1,1}, \\ \begin{pmatrix} \frac{e^{i\varphi_{\mathbf{k}}} + e^{-i\varphi_{\mathbf{k}}}}{2} \\ n \\ \frac{e^{i\varphi_{\mathbf{k}}} - e^{-i\varphi_{\mathbf{k}}}}{2i} \end{pmatrix} &= \begin{pmatrix} 0 \\ n \\ 0 \end{pmatrix} + \frac{e^{i\varphi_{\mathbf{k}}}}{2i} \begin{pmatrix} i \\ 0 \\ 1 \end{pmatrix} - \frac{e^{-i\varphi_{\mathbf{k}}}}{2i} \begin{pmatrix} -i \\ 0 \\ 1 \end{pmatrix} = n\chi_{1,0} + \frac{e^{i\varphi_{\mathbf{k}}}}{\sqrt{2}i} \chi_{1,-1} - \frac{e^{-i\varphi_{\mathbf{k}}}}{\sqrt{2}i} \chi_{1,1}. \end{aligned} \quad (2.74)$$

Then we collect the terms with the same pseudospin eigenstates:

$$\begin{aligned} \Psi_{l,s=1}(r, \varphi_{\mathbf{r}}, z) &= \int d^2k \left( \left( \Psi_0 \frac{-i}{2} f_l(\mathbf{k}) e^{i\varphi_{\mathbf{k}}} \right) \left( \frac{1}{\sqrt{A}} \frac{1}{\sqrt{2}} e^{i\mathbf{k} \cdot \mathbf{r}} \right) 2i(-1) \sin(\kappa kz) \right) \chi_{1,0} + \\ &+ \int d^2k \left( \left( \Psi_0 \frac{1}{\sqrt{2}} f_l(\mathbf{k}) e^{i\varphi_{\mathbf{k}}} \right) \left( \frac{1}{\sqrt{A}} e^{i\mathbf{k} \cdot \mathbf{r}} \right) \frac{e^{i\varphi_{\mathbf{k}}}}{\sqrt{2}} + \right. \\ &+ \left. \left( \Psi_0 \frac{-i}{2} f_l(\mathbf{k}) e^{i\varphi_{\mathbf{k}}} \right) \left( \frac{1}{\sqrt{A}} \frac{1}{\sqrt{2}} e^{i\mathbf{k} \cdot \mathbf{r}} \right) \frac{e^{i\varphi_{\mathbf{k}}}}{\sqrt{2}i} 2 \cos(\kappa kz) \right) \chi_{1,-1} + \\ &+ \int d^2k \left( \left( \Psi_0 \frac{1}{\sqrt{2}} f_l(\mathbf{k}) e^{i\varphi_{\mathbf{k}}} \right) \left( \frac{1}{\sqrt{A}} e^{i\mathbf{k} \cdot \mathbf{r}} \right) \frac{e^{-i\varphi_{\mathbf{k}}}}{\sqrt{2}} - \right. \\ &- \left. \left( \Psi_0 \frac{-i}{2} f_l(\mathbf{k}) e^{i\varphi_{\mathbf{k}}} \right) \left( \frac{1}{\sqrt{A}} \frac{1}{\sqrt{2}} e^{i\mathbf{k} \cdot \mathbf{r}} \right) \frac{e^{-i\varphi_{\mathbf{k}}}}{\sqrt{2}i} 2 \cos(\kappa kz) \right) \chi_{1,1}. \end{aligned} \quad (2.75)$$

We can use  $1 - \cos(2x) = 2 \sin^2(x)$  and  $1 + \cos(2x) = 2 \cos^2(x)$  to get:

$$\begin{aligned} \Psi_{l,s=1}(r, \varphi_r, z) &= \frac{\Psi_0}{\sqrt{A}} \int_0^{2\pi} \int_0^\infty d\varphi_{\mathbf{k}} k dk f_l(\mathbf{k}) \chi_{1,1} e^{i\mathbf{k}\cdot\mathbf{r}} \cos^2\left(\frac{\kappa kz}{2}\right) + \\ &+ \frac{\Psi_0}{\sqrt{A}} \int_0^{2\pi} \int_0^\infty d\varphi_{\mathbf{k}} k dk f_l(\mathbf{k}) e^{2i\varphi_{\mathbf{k}}} \chi_{1,-1} e^{i\mathbf{k}\cdot\mathbf{r}} \sin^2\left(\frac{\kappa kz}{2}\right) + \\ &+ \frac{-\Psi_0}{\sqrt{2A}} \int_0^{2\pi} \int_0^\infty d\varphi_{\mathbf{k}} k dk f_l(\mathbf{k}) e^{i\varphi_{\mathbf{k}}} \chi_{1,0} e^{i\mathbf{k}\cdot\mathbf{r}} \sin(\kappa kz). \end{aligned} \quad (2.76)$$

Now we plug in  $f(\mathbf{k})$  and perform a change in variables  $\mathbf{k} \cdot \mathbf{r} = kr \cos(\varphi_{\mathbf{k}} - \varphi_r)$  to get:

$$\begin{aligned} \Psi_{l,s=1} &= e^{il\varphi_r} \chi_{1,1} \frac{\Psi_0}{\sqrt{A}} \int_0^{2\pi} \int_0^\infty d\varphi dk k^{l+1} e^{il\varphi} e^{-k^2/k_F^2} e^{ikr \cos(\varphi)} \cos^2\left(\frac{\kappa kz}{2}\right) + \\ &+ e^{i(l+2)\varphi_r} \chi_{1,-1} \frac{\Psi_0}{\sqrt{A}} \int_0^{2\pi} \int_0^\infty d\varphi dk k^{l+1} e^{i(l+2)\varphi} e^{-k^2/k_F^2} e^{ikr \cos(\varphi)} \sin^2\left(\frac{\kappa kz}{2}\right) + \\ &+ e^{i(l+1)\varphi_r} \chi_{1,0} \frac{-\Psi_0}{\sqrt{2A}} \int_0^{2\pi} \int_0^\infty d\varphi dk k^{l+1} e^{i(l+1)\varphi} e^{-k^2/k_F^2} e^{ikr \cos(\varphi)} \sin(\kappa kz). \end{aligned} \quad (2.77)$$

We can, again, define the  $g$ -functions:

$$\begin{aligned} g_{1,1}^{(l)}(r, z) &= \frac{\Psi_0}{\sqrt{A}} \int_0^{2\pi} \int_0^\infty d\varphi dk k^{l+1} e^{il\varphi} e^{-\frac{k^2}{k_F^2}} e^{ikr \cos(\varphi)} \cos^2\left(\frac{\kappa kz}{2}\right) \\ g_{1,0}^{(l)}(r, z) &= \frac{-\Psi_0}{\sqrt{2A}} \int_0^{2\pi} \int_0^\infty d\varphi dk k^{l+1} e^{i(l+1)\varphi} e^{-\frac{k^2}{k_F^2}} e^{ikr \cos(\varphi)} \sin(\kappa kz), \\ g_{1,-1}^{(l)}(r, z) &= \frac{\Psi_0}{\sqrt{A}} \int_0^{2\pi} \int_0^\infty d\varphi dk k^{l+1} e^{i(l+2)\varphi} e^{-\frac{k^2}{k_F^2}} e^{ikr \cos(\varphi)} \sin^2\left(\frac{\kappa kz}{2}\right). \end{aligned} \quad (2.78)$$

And then we arrive at the final expression:

$$\Psi_{l,s=1} = e^{il\varphi_r} \chi_{1,1} g_{1,1}^{(l)} + e^{i(l+1)\varphi_r} \chi_{1,0} g_{1,0}^{(l)} + e^{i(l+2)\varphi_r} \chi_{1,-1} g_{1,-1}^{(l)}, \quad (2.79)$$

where we can see that the topological charge stayed the same in the excited pseudospin component, but it increased in the unexcited components by a maximum value of  $l + 2s$ ,  $s = 1$ . The profiles of the  $g$ -functions are shown in Fig. 2.17. The intensities of the  $g$ -functions are shown in Fig. 2.18, where we can see that the size of the donut increases with the increase in  $l$ , as is expected for vortex beams.

In this section we have shown the mapping of topological charge from the momentum space to the real space for the honeycomb and Lieb lattices that follows the rule  $l \mapsto l + 2s$ . In the next section, we will show that this mapping has a topological origin and that this mapping happens

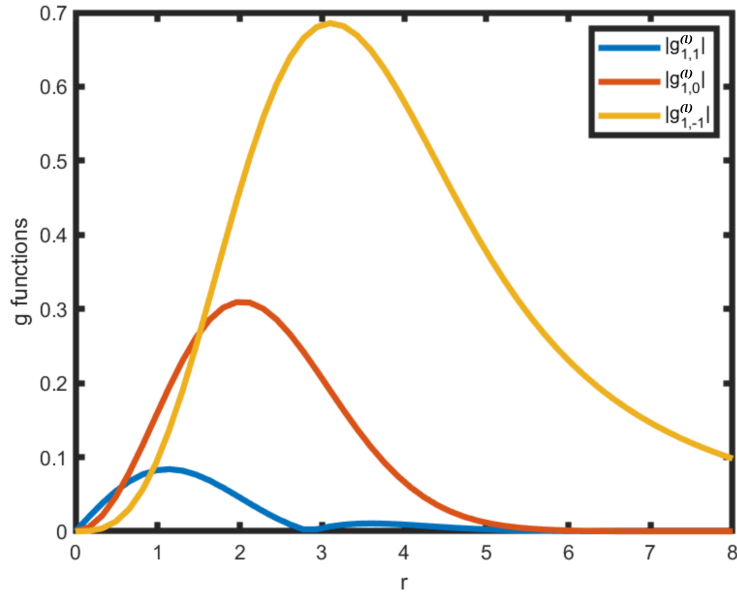


**Figure 2.17:** Profiles of the Lieb lattice  $g$ -functions. The profile shows that the Lieb lattice  $g$ -functions are donut shaped. The parameters  $\psi_0$ ,  $A$ ,  $k_F$ ,  $l = 1$  and  $\kappa$  are taken as unity, and  $z = 0.2$ .

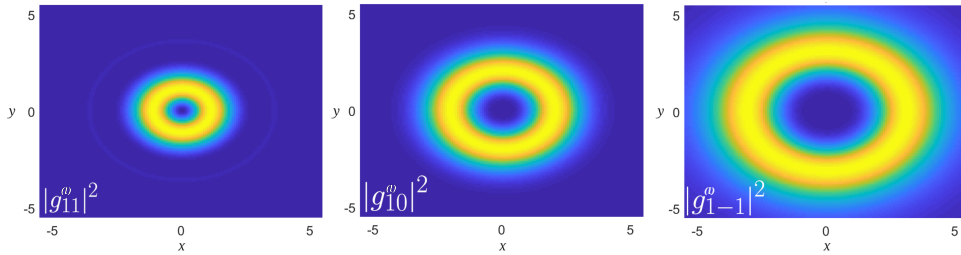


**Figure 2.18:** Intensity of the Lieb lattice  $g$ -functions. All of the  $g$ -functions are donut-shaped. Numerically we can infer that the size of the donuts increases with  $l$ .

for a general Hamiltonian of the form  $H = \kappa \mathbf{S} \cdot \mathbf{k}$ .

## 2.5 Topological origin of the momentum-to-real-space mapping

### 2.5.1 Topological charges in the momentum space

So far, we have discussed the topological charge conversion in the honeycomb and Lieb lattices and explained the results kinematically, via the conservation of angular momentum, and dynamically, by expanding the initial excitation in eigenmodes of the Hamiltonian. However,

there is a fundamental topological mechanism beyond the charge conversion that was observed in the experiment. The results for the honeycomb and the Lieb lattice of the previous section tie directly into it, so let us repeat them here in one place: At the output, in the far field, the complex amplitudes of the electric field are:

$$\Psi_{l,s=\frac{1}{2}}(\mathbf{r}, z) = e^{il\phi_r} \chi_{\frac{1}{2}, \frac{1}{2}} g_{\frac{1}{2}, \frac{1}{2}}^{(l)}(r, z) + e^{i(l+1)\phi_r} \chi_{\frac{1}{2}, -\frac{1}{2}} g_{\frac{1}{2}, -\frac{1}{2}}^{(l)}(r, z), \quad (2.80)$$

for the honeycomb lattice, and:

$$\Psi_{l,s=1} = e^{il\phi_r} \chi_{1,1} g_{1,1}^{(l)}(r, z) + e^{i(l+1)\phi_r} \chi_{1,0} g_{1,0}^{(l)}(r, z) + e^{i(l+2)\phi_r} \chi_{1,-1} g_{1,-1}^{(l)}(r, z), \quad (2.81)$$

for the Lieb lattice. When a single pseudospin component is excited, the momentum space vortices in the other components are mapped from the momentum to real space, giving rise to the topological charge conversion. Now, we will show that the difference in the topological charges of pseudospin components in the momentum space is related to the Berry phase winding around the Dirac point.

## 2.5.2 Topology of the honeycomb lattice

The HCL has a topological singularity at the Dirac point: the Berry phase acquired as one traverses a loop around the Dirac point is  $\pi$ ; the Dirac point can be considered as a flux tube, i.e., a topological singularity of the Berry curvature [76]. Our experiments essentially reveal how the excitations of the modes around the singularity are mapped into the far field dynamics. To see that clearly, we revisit the calculation of the Berry phase in the honeycomb lattice. An eigenstate close to the conical intersection in the honeycomb lattice is given by Eq. (2.9):

$$\Psi_{n,\mathbf{k}} = \frac{1}{\sqrt{2}} \begin{pmatrix} n \\ e^{i\phi_{\mathbf{k}}} \end{pmatrix}, \quad (2.82)$$

and  $n = \pm 1$ . As we adiabatically circle around the Dirac point, the acquired Berry phase can be calculated by using the Eq. (1.7):

$$\gamma = -i \oint \langle \Psi_{n,\mathbf{k}} | \nabla_{\mathbf{k}} | \Psi_{n,\mathbf{k}} \rangle \cdot d\mathbf{k} = \quad (2.83)$$

$$= -i \frac{1}{2} \oint (n e^{-i\varphi_{\mathbf{k}}}) \frac{\partial}{\partial \varphi_{\mathbf{k}}} \begin{pmatrix} n \\ e^{i\varphi_{\mathbf{k}}} \end{pmatrix} d\varphi_{\mathbf{k}} = \quad (2.84)$$

$$= -i \frac{1}{2} \oint (n e^{-i\varphi_{\mathbf{k}}}) \begin{pmatrix} 0 \\ ie^{i\varphi_{\mathbf{k}}} \end{pmatrix} d\varphi_{\mathbf{k}} = \quad (2.85)$$

$$= \frac{1}{2} \oint (0 + 1) d\varphi_{\mathbf{k}} = \quad (2.86)$$

$$= \frac{1}{2} \int_0^{2\pi} d\varphi_{\mathbf{k}} = \pi \equiv w\pi, \quad (2.87)$$

where  $w = 1$  is a topological invariant called the Berry phase winding. The Berry phase arises from the specific phase relation in the momentum space between the pseudospin components of the eigenstates. There is a vortex, i.e. a topological charge in the momentum space in one of the pseudospin components; more precisely, the difference in topological charges in the momentum space of the two components is one. In the previous section, we have seen that this vortex is mapped from the momentum space to the real space during propagation. Thus, what we observed in our experiments is the topological singularity of the honeycomb lattice mapped from the momentum to the real space.

### 2.5.3 Topology of the Lieb lattice

For the Lieb lattice, we can perform a similar calculation as the one for the honeycomb lattice. The eigenstates of the Lieb lattice are given in the Eq. (2.26), but this form is unsuitable for the calculation of the Berry phase because they are ill-defined for  $k \rightarrow 0$ , because of the division by  $k$ . Instead, we need to find the eigenstates of the Hamiltonian before the approximation in the vicinity of the Dirac point, and then perform the limit  $k \rightarrow 0$ . These eigenstates are:

$$\Psi_{\pm 1, \mathbf{k}} = \frac{1}{\sqrt{2}} \begin{pmatrix} e^{-i\varphi_{\mathbf{k}}} \\ \pm 1 \\ -ie^{-i\varphi_{\mathbf{k}}} \end{pmatrix}. \quad (2.88)$$

The Berry phase is then:

$$\gamma = -i \oint \left\langle \Psi_{n,\mathbf{k}} \left| \frac{\partial}{\partial \varphi_{\mathbf{k}}} \right| \Psi_{n,\mathbf{k}} \right\rangle d\varphi_{\mathbf{k}} = \quad (2.89)$$

$$= \frac{-i}{2} \oint (e^{i\varphi_{\mathbf{k}}} \pm 1 e^{i\varphi_{\mathbf{k}}}) \frac{\partial}{\partial \varphi_{\mathbf{k}}} \begin{pmatrix} e^{-i\varphi_{\mathbf{k}}} \\ \pm 1 \\ -ie^{-i\varphi_{\mathbf{k}}} \end{pmatrix} d\varphi_{\mathbf{k}} = \quad (2.90)$$

$$= \frac{-i}{2} \oint (e^{i\varphi_{\mathbf{k}}} \pm 1 e^{i\varphi_{\mathbf{k}}}) \begin{pmatrix} -ie^{-i\varphi_{\mathbf{k}}} \\ 0 \\ e^{-i\varphi_{\mathbf{k}}} \end{pmatrix} = -i \oint id\varphi_{\mathbf{k}} = 2\pi \equiv w\pi, \quad (2.91)$$

where the Berry phase winding is now  $w = 2$ . The eigenstate  $\Psi_{0,\mathbf{k}}$  differs from the eigenstates  $\Psi_{\pm 1,\mathbf{k}}$  by a negative sign in one of the components, so it can easily be seen that the Berry phase is trivial, and, therefore, not interesting in this case. Nevertheless, we can see that the topological charge conversion by 2 in the Lieb lattice, of the previous section, comes from the maximum difference between the pseudospin components of the momentum space and that it is related to the Berry phase winding  $w = 2$ .

#### 2.5.4 Berry phase winding as a signature of the topological charge conversion

The finding that the topological charge conversion has a fundamental topological origin in the Berry phase winding holds for any pseudospin  $S$  in systems governed by the Hamiltonian  $H = \kappa \mathbf{S} \cdot \mathbf{k}$ . Every eigenstate of the Hamiltonian can be expanded in the basis of pseudospin as:

$$\Psi_{n,\mathbf{k}} = \sum_{s=-S}^S \langle \chi_{S,s} | \Psi_{n,\mathbf{k}} \rangle \chi_{S,s} \quad (2.92)$$

The coefficients  $\langle \chi_{S,s} | \Psi_{n,\mathbf{k}} \rangle$  can be found by rewriting the Hamiltonian as:

$$H = \kappa k \left( S_+ e^{-i\varphi_{\mathbf{k}}} + S_- e^{i\varphi_{\mathbf{k}}} \right), \quad (2.93)$$

where  $S_{\pm} = S_x \pm iS_y$ . Then we have:

$$\begin{aligned} \beta_{n,\mathbf{k}} \langle \chi_{S,s} | \Psi_{n,\mathbf{k}} \rangle &= \langle \chi_{S,s} | H | \Psi_{n,\mathbf{k}} \rangle = \\ &= \frac{\kappa}{2} k \left( \sqrt{(S-s)(S+s+1)} \langle \chi_{S,s+1} | \Psi_{n,\mathbf{k}} \rangle e^{-i\phi_{\mathbf{k}}} + \right. \\ &\quad \left. + \sqrt{(S+s)(S-s+1)} \langle \chi_{S,s-1} | \Psi_{n,\mathbf{k}} \rangle e^{i\phi_{\mathbf{k}}} \right). \end{aligned} \quad (2.94)$$

There is a clear phase relationship between different pseudospin components of the eigenstates: The difference in the topological charges, i.e. the vortices, of the neighboring pseudospin components in the momentum space is 1. E.g., if we look at the Eq. (2.94), we can see that the topological charge associated with the pseudospin component  $\chi_{S,s}$  is  $l = 0$ , while the topological charge associated with its neighboring pseudospin component  $\chi_{S,s+1}$  is  $l = -1$ , i.e. their difference is  $0 - (-1) = 1$ . The total topological charge conversion is then equal to the maximum difference in topological charges of the pseudospin components. When a single pseudospin component is excited, the topological charges of the unexcited components in the momentum space are mapped to real space, which is the fundamental mechanism behind topological charge conversions observed in our experiments. The Berry phase around the Dirac point is  $w\pi$ . The topological invariant  $w$ , i.e. the Berry phase winding is also the maximal difference between the topological charges of pseudospin components in the momentum space. For the honeycomb lattice,  $w = 1$ ; and for the Lieb lattice,  $w = 2$ . For the studied honeycomb and the Lieb lattices, the rule:

$$l \mapsto l + 2s, \quad (2.95)$$

which holds only for optimally aligned excitations, can then be expressed as a more general rule:

$$l \mapsto l \pm w \quad (2.96)$$

where  $+w$  is for the case  $l > 0$  and  $-w$  is for the case  $l < 0$ . It turns out that this latter expression for the conversion rule, which contains the topological quantity  $w$ , is more fundamental than the one containing pseudospin  $s$ , as can be seen on the following examples.

### 2.5.5 Topological charge conversion in a stretched lattice

Consider a conical intersection described by the Hamiltonian:

$$H_s = \kappa_x S_x k_x + \kappa_y S_y k_y, \quad (2.97)$$

where the angular momentum is not conserved for  $k_x \neq k_y$  due to the lack of rotational symmetry. This Hamiltonian describes a stretched lattice. In the case of  $\kappa_x = \kappa_y$ , this Hamiltonian reverts back to  $H = \kappa \mathbf{S} \cdot \mathbf{k}$  for lattices that are not stretched. An inspection of the eigenstates of  $H_s$  for pseudospin  $S = 1/2$  and  $S = 1$  shows that the momentum space vortices become elliptical but preserve their topological charge. For the stretched honeycomb lattice ( $S = 1/2$ ), the winding of the Berry phase around the Dirac point is protected, until the stretching is sufficiently large so that the inequivalent Dirac points merge and a gap opens [82, 83, 84]. After this transition the Berry phase vanishes and the topological charge conversion no longer occurs. In Fig. 2.19, we show numerical simulations for an optimally aligned initial condition in the stretched honeycomb and the stretched Lieb lattice. The nearest neighbor spacing for the HCL and the

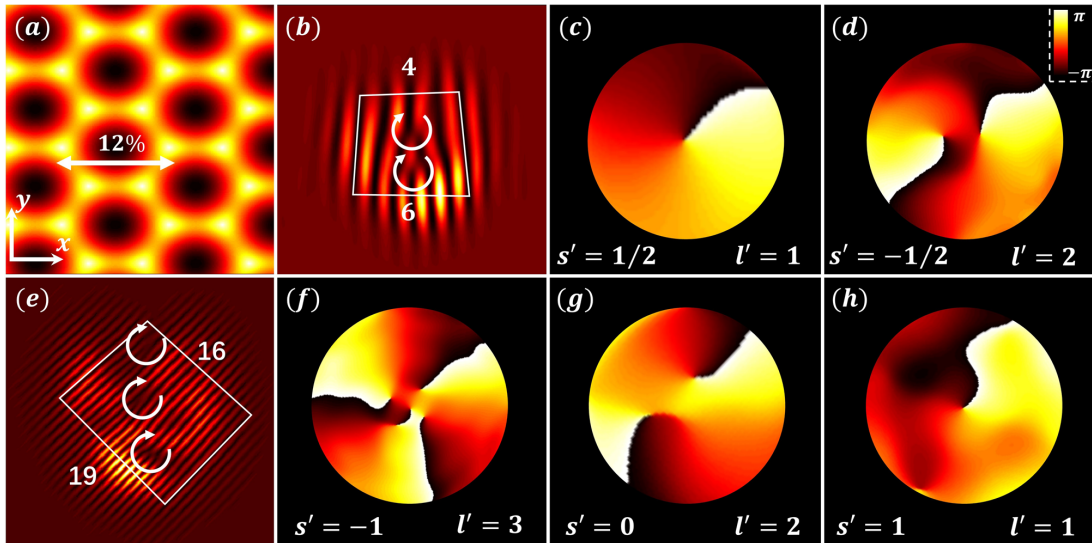


**Figure 2.19:** Evolution of pseudospin states in stretched lattices. The stretched lattices lack the rotational symmetry around the conical intersections, so the total angular momentum is not conserved. The top row corresponds to a stretched HCL, with an initial excitation  $l = 1$ ,  $s = 1/2$ . The bottom row corresponds to a stretched Lieb lattice, with an initial excitation  $l = 1$ ,  $s = 1$ . (a) A 12% horizontally stretched HCL. (b), (e) Interferograms of the output beams, which clearly indicate the topological conversion from  $l$  to  $l + 2s$  (or  $l \pm w$ ). This is underpinned by the phase structure of the pseudospin components at the output illustrated in (c), (d) and (f)–(h) for the two lattices.

Lieb lattice is  $9 \mu\text{m}$ , and they are stretched by 12% and 15%, respectively. The conversion of the

topological charge from  $l$  to  $l \pm w$  holds even when the angular momentum  $J_z$  is not conserved, which indicates that the mapping of the topological charges from the momentum space to the real space is a fundamental process with a topological origin.

### 2.5.6 Beyond conical intersections

Because the observed mapping is fundamentally a topological phenomenon, it can thereby occur in other systems besides those with the conical intersections in the honeycomb and the Lieb lattices. Here we demonstrate the validity of our interpretation using two different band structures. The first one is the Hamiltonian:

$$H_m = \begin{pmatrix} 0 & (k_x - ik_y)^m \\ (k_x + ik_y)^m & 0 \end{pmatrix} = k^m \begin{pmatrix} 0 & e^{-im\varphi_{\mathbf{k}}} \\ e^{im\varphi_{\mathbf{k}}} & 0 \end{pmatrix}. \quad (2.98)$$

For  $m = 1$ , this is just the regular honeycomb lattice that we already discussed. But, the band structure for  $m = 2$  corresponds to the bilayer graphene and has a parabolic band-touching point, and for  $m > 2$ , it corresponds to other variants of band touching. It is straightforward to see that all the previous calculations for the HCL hold, even when we replace  $e^{i\varphi_{\mathbf{k}}}$  with  $e^{im\varphi_{\mathbf{k}}}$ . And, so, it is clear that the Berry phase in the case of the Hamiltonian in Eq. (2.98), is  $m\pi$ , where the Berry phase winding is now  $w = m$ , and the topological charge conversion rule  $l \mapsto l \pm w$  persists. However, the expression  $l \mapsto l + 2s$  that relies on the angular momentum is no longer applicable because  $[H, J_z] \neq 0$  for  $m \neq 1$ . Another example is the Hamiltonian  $H_0 = k\sigma_z$ , where the eigenstates of the Hamiltonian itself are the spinors:

$$\chi_{\frac{1}{2}, \frac{1}{2}} = \begin{pmatrix} 1 \\ 0 \end{pmatrix}, \chi_{\frac{1}{2}, -\frac{1}{2}} = \begin{pmatrix} 0 \\ 1 \end{pmatrix}, \quad (2.99)$$

which are also the eigenstates of  $\sigma_z$ . They are constant in  $\varphi_{\mathbf{k}}$  and so we can immediately see that the Berry phase winding is 0, because of the differentiation with the respect to  $\varphi_{\mathbf{k}}$  in the calculation. Because the Hamiltonian commutes with the  $z$ -component of the pseudospin operator  $\sigma_z$ , when we excite one of the pseudospins, there will be no energy transfer to the other component during evolution, and therefore there will be no topological charge conversion, again consistent with  $l \mapsto l \pm w = l + 0 = l$ . Considering these examples, where the pseudospin plays no role, a more general interpretation of our experimental observations should be formulated by the winding of the Berry phase as the topological quantity, rather than just the pseudospin.

## 2.6 A proposal for a 3D system

### 2.6.1 The Weyl lattice

So far, we have shown how a mapping of topological singularities from the momentum space to the real space works in 2D systems. Next, we expand our results beyond the 2D platform. Our experiments and theoretical considerations are performed in 2D lattices. However, analogous considerations can be made for 3D Hamiltonians. An interesting example is that of a Weyl Hamiltonian:

$$H_{\text{Weyl}} = \boldsymbol{\sigma} \cdot \mathbf{k} = \sigma_x k_x + \sigma_y k_y + \sigma_z k_z. \quad (2.100)$$

The Weyl Hamiltonian has been experimentally realized in the Brillouin zone of specially designed optical and condensed matter structures [48, 49]. This Hamiltonian gives rise to a synthetic magnetic monopole in the momentum space [50] with a topological charge  $l = 1$ . The eigenvalues of the Hamiltonian are:

$$\beta_{n,\mathbf{k}} = n \frac{\kappa}{2} \sqrt{k_x^2 + k_y^2 + k_z^2}, \quad n = \pm 1. \quad (2.101)$$

The corresponding eigenmodes are:

$$\Psi_{+1,\mathbf{k}} = \begin{pmatrix} \cos\left(\frac{\theta_{\mathbf{k}}}{2}\right) e^{-i\phi_{\mathbf{k}}} \\ \sin\left(\frac{\theta_{\mathbf{k}}}{2}\right) \end{pmatrix}, \quad \Psi_{-1,\mathbf{k}} = \begin{pmatrix} \sin\left(\frac{\theta_{\mathbf{k}}}{2}\right) e^{-i\phi_{\mathbf{k}}} \\ -\cos\left(\frac{\theta_{\mathbf{k}}}{2}\right) \end{pmatrix}, \quad (2.102)$$

where  $k$ ,  $\theta_k$  and  $\phi_k$  are now the spherical coordinates. This is a pseudospin-1/2 system, so the eigenstates are,  $\chi_{S=1/2,s=1/2}$  and  $\chi_{S=1/2,s=-1/2}$ , just like for the honeycomb lattice.

### 2.6.2 Mapping of the Weyl monopole from the momentum space to the real space

To map the topological charge from the momentum space to the real space, we excite the modes in the vicinity of the Weyl point. Suppose that initially we excite an arbitrary pseudospin state, denoted by  $(\alpha, \beta)$ , by a rotationally symmetric Gaussian-like distribution,  $f(\mathbf{k}) = f(k)$ :

$$\Psi_{0,\alpha\beta}(\mathbf{r}, t = 0) = \sum_n \int d^3k \langle \Psi_{n,\mathbf{k}} | \Psi_{0,\alpha\beta} \rangle \Psi_{n,\mathbf{k}}, \quad (2.103)$$

where  $\Psi_0$  is a normalization constant and  $V$  is the volume of the system. The procedure is then just like the one we used for the honeycomb and the Lieb lattice. We start by expanding the initial excitation over the eigenstates of the Weyl Hamiltonian:

$$\Psi_{0,\alpha\beta}(\mathbf{r}, t = 0) = \sum_n \int d^3k \langle \Psi_{n,\mathbf{k}} | \Psi_{0,\alpha\beta} \rangle \Psi_{n,\mathbf{k}}. \quad (2.104)$$

The relevant scalar products are:

$$\langle \Psi_{+1,\mathbf{k}} | \Psi_{0,\alpha\beta} \rangle = \Psi_0 f(k) \left( \alpha \cos\left(\frac{\theta_{\mathbf{k}}}{2}\right) e^{i\varphi_{\mathbf{k}}} + \beta \sin\left(\frac{\theta_{\mathbf{k}}}{2}\right) \right), \quad (2.105)$$

$$\langle \Psi_{-1,\mathbf{k}} | \Psi_{0,\alpha\beta} \rangle = \Psi_0 f(k) \left( \alpha \sin\left(\frac{\theta_{\mathbf{k}}}{2}\right) e^{i\varphi_{\mathbf{k}}} - \beta \cos\left(\frac{\theta_{\mathbf{k}}}{2}\right) \right). \quad (2.106)$$

The evolution is then:

$$\begin{aligned} \Psi_{0,\alpha\beta}(\mathbf{r}, t) &= \Psi_0 \int d^3k \frac{1}{\sqrt{V}} e^{i\mathbf{k}\cdot\mathbf{r}} f(k) \times \\ &\times \left[ \left( \alpha \cos\left(\frac{\theta_{\mathbf{k}}}{2}\right) e^{i\varphi_{\mathbf{k}}} + \beta \sin\left(\frac{\theta_{\mathbf{k}}}{2}\right) \right) \begin{pmatrix} \cos\left(\frac{\theta_{\mathbf{k}}}{2}\right) e^{-i\varphi_{\mathbf{k}}} \\ \sin\left(\frac{\theta_{\mathbf{k}}}{2}\right) \end{pmatrix} e^{i\omega_0 t} + \right. \\ &\left. + \left( \alpha \sin\left(\frac{\theta_{\mathbf{k}}}{2}\right) e^{i\varphi_{\mathbf{k}}} - \beta \cos\left(\frac{\theta_{\mathbf{k}}}{2}\right) \right) \begin{pmatrix} \sin\left(\frac{\theta_{\mathbf{k}}}{2}\right) e^{-i\varphi_{\mathbf{k}}} \\ -\cos\left(\frac{\theta_{\mathbf{k}}}{2}\right) \end{pmatrix} e^{-i\omega_0 t} \right], \quad (2.107) \end{aligned}$$

where  $\omega_0 = \kappa k/2$ . It is safe to assume we have excited the pseudospin component  $\chi_{1/2,1/2}$ , i.e., that  $\alpha = 1$  and  $\beta = 0$ . Then we get:

$$\begin{aligned} \Psi_{0,\alpha\beta}(\mathbf{r}, t) &= \Psi_0 \int d^3k \frac{1}{\sqrt{V}} e^{i\mathbf{k}\cdot\mathbf{r}} f(k) \times \\ &\times \left[ \alpha \cos\left(\frac{\theta_{\mathbf{k}}}{2}\right) e^{i\varphi_{\mathbf{k}}} \begin{pmatrix} \cos\left(\frac{\theta_{\mathbf{k}}}{2}\right) e^{-i\varphi_{\mathbf{k}}} \\ \sin\left(\frac{\theta_{\mathbf{k}}}{2}\right) \end{pmatrix} e^{i\omega_0 t} + \right. \\ &\left. + \alpha \sin\left(\frac{\theta_{\mathbf{k}}}{2}\right) e^{i\varphi_{\mathbf{k}}} \begin{pmatrix} \sin\left(\frac{\theta_{\mathbf{k}}}{2}\right) e^{-i\varphi_{\mathbf{k}}} \\ -\cos\left(\frac{\theta_{\mathbf{k}}}{2}\right) \end{pmatrix} e^{-i\omega_0 t} \right]. \quad (2.108) \end{aligned}$$

We can collect the terms with the same pseudospin components:

$$\Psi_{0,\frac{1}{2}}(\mathbf{r}, t) = \Psi_0 \int d^3k \frac{1}{\sqrt{V}} e^{i\mathbf{k}\cdot\mathbf{r}} f(k) \times \quad (2.109)$$

$$\times \left\{ \sin(\theta_{\mathbf{k}}) \begin{pmatrix} 0 \\ 1 \end{pmatrix} e^{i\varphi_{\mathbf{k}}} i \sin(\omega_0 t) + \begin{pmatrix} 1 \\ 0 \end{pmatrix} \left[ e^{i\omega_0 t} \cos^2\left(\frac{\theta_{\mathbf{k}}}{2}\right) + e^{-i\omega_0 t} \sin^2\left(\frac{\theta_{\mathbf{k}}}{2}\right) \right] \right\}. \quad (2.110)$$

If the initial excitation is a Gaussian:

$$f(k) = \exp\left(-\frac{k^2}{k_F^2}\right), \quad (2.111)$$

we get:

$$\Psi_{0,\frac{1}{2}}(\mathbf{r}, t) = \Psi_0 \int d^3k \frac{1}{\sqrt{V}} e^{i\mathbf{k}\cdot\mathbf{r}} \left(-\frac{k^2}{k_F^2}\right) \times \left\{ \sin(\theta_{\mathbf{k}}) \begin{pmatrix} 0 \\ 1 \end{pmatrix} e^{i\varphi_{\mathbf{k}}} i \sin(\omega_0 t) + \begin{pmatrix} 1 \\ 0 \end{pmatrix} \left[ e^{i\omega_0 t} \cos^2\left(\frac{\theta_{\mathbf{k}}}{2}\right) + e^{-i\omega_0 t} \sin^2\left(\frac{\theta_{\mathbf{k}}}{2}\right) \right] \right\}. \quad (2.112)$$

Now we can substitute in:

$$\mathbf{k} \cdot \mathbf{r} = kr \sin \theta_{\mathbf{k}} \sin \theta_r \cos(\varphi_{\mathbf{k}} - \varphi_r) + kr \cos \theta_{\mathbf{k}} \cos \theta_r, \quad (2.113)$$

and perform the change in variables  $\varphi = \varphi_{\mathbf{k}} - \varphi_r$  to get:

$$\Psi_{0,\frac{1}{2}}(r, \theta_r, \varphi_r, t) = \chi_{\frac{1}{2}, \frac{1}{2}} g_{\frac{1}{2}, \frac{1}{2}}(r, \theta_r, t) + e^{i\varphi_r} \chi_{\frac{1}{2}, -\frac{1}{2}} g_{\frac{1}{2}, -\frac{1}{2}}(r, \theta_r, t), \quad (2.114)$$

where the  $g$ -functions are defined by:

$$g_{\frac{1}{2}, -\frac{1}{2}}(r, \theta_r, t) = \quad (2.115)$$

$$\int_0^\infty dk \int_0^\pi k \sin \theta_{\mathbf{k}} d\theta_{\mathbf{k}} \int_0^{2\pi} kd\varphi \frac{\Psi_0}{\sqrt{V}} e^{i(kr \sin \theta_{\mathbf{k}} \sin \theta_r \cos \varphi + kr \cos \theta_{\mathbf{k}} \cos \theta_r)} e^{-\frac{k^2}{k_F^2} \sin \theta_{\mathbf{k}}} e^{i\varphi} i \sin(\omega_0 t),$$

$$g_{\frac{1}{2}, \frac{1}{2}}(r, \theta_r, t) = \quad (2.116)$$

$$\int_0^\infty dk \int_0^\pi k \sin \theta_{\mathbf{k}} d\theta_{\mathbf{k}} \int_0^{2\pi} kd\varphi \frac{\Psi_0}{\sqrt{V}} e^{i(kr \sin \theta_{\mathbf{k}} \sin \theta_r \cos \varphi + kr \cos \theta_{\mathbf{k}} \cos \theta_r)} \times e^{-\frac{k^2}{k_F^2}} \left[ e^{i\omega_0 t} \cos^2\left(\frac{\theta_{\mathbf{k}}}{2}\right) + e^{-i\omega_0 t} \sin^2\left(\frac{\theta_{\mathbf{k}}}{2}\right) \right].$$

This result is equivalent to the result for the honeycomb lattice. Here too, the pseudospin component  $\chi_{S=1/2, s=1/2}$  is excited, this time with a Gaussian beam with  $l = 0$ . There is a topological charge  $l$  in the pseudospin components in the momentum space as can be seen in Eq. (2.102). Also, during the propagation, the vortex in the unexcited component maps from the momentum space to the real space as can be seen in Eq. (2.114). If we excite an arbitrary pseudospin state  $\alpha\chi_{S=1/2, s=1/2} + \beta\chi_{S=1/2, s=-1/2}$  with a Gaussian-like distribution we will obtain a vortex field with a topological charge identical to the charge of the Weyl monopole at the output because the Weyl Hamiltonian is 3D rotationally invariant, i.e. because  $[\mathbf{J}, H_{\text{Weyl}}] = 0$ . The resulting vorticity will point in the direction of the initial pseudospin. In this way, with a properly designed initial excitation, a mapping of topological properties of the Weyl monopole to topological charges in the real space can be achieved. This type of dynamics in 3D Weyl systems could be achieved in ultracold atomic gases [85], and it could be related to an experiment where an electron beam, scattered from a magnetic monopole, experienced a conversion into an electron vortex [86].

## 2.7 Chapter conclusion

In this chapter we have demonstrated the universal mapping of topological singularities in the momentum space, from the momentum space, to measurable topological entities in the real space. The experiments were carried out in the photonic honeycomb and Lieb lattices. The mapping can be theoretically explained via the pseudospin-orbit interaction, the angular momentum conservation and the nontrivial winding of the Berry phase. We have demonstrated that the underlying mechanism for the mapping is fundamentally topological in origin, and that it follows the general rule  $l \mapsto l \pm w$ , where  $l$  is the topological charge and  $w$  is the Berry phase winding. Apart from the honeycomb and Lieb lattices, we have shown that it also occurs in the stretched lattices where the angular momentum is not conserved, and for parabolic band touching and other nonconical intersections. We have also predicted that the same mechanism exists in 3D Weyl lattices where synthetic magnetic monopoles play the role of topological singularities. This opens up many interesting questions. For instance: Is it possible to create vortices of Bose–Einstein condensates [87] by a topological conversion from the synthetic magnetic monopoles in ultracold atomic gases? How could the mechanism explored here be adapted for a topological conversion with photons in a photonic Dirac monopole field [88]? Is the spin angular momentum that comes from the light polarization indispensable in the spin-to-orbital angular momentum conversion, as commonly thought, or are the pseudospin and the topological conversion what is essential, even in the conventional settings based on the optical

phase elements [62, 64]? What other mechanisms are possible where the topological properties of the bands can be directly mapped from the momentum to the real space in experiments? Can other topological entities, such as the vortex knots and the nodal chains [89, 90, 91], be directly mapped from the momentum space to the real space or vice versa, or can they be mapped onto a synthetic space [92, 93]?

These findings and the questions that arise from them make a compelling argument for how important the mapping of topological properties is for the fundamentals of topology.



# Chapter 3

## Nonlinear control of higher-order topological insulators

The work presented in this chapter has been published in:

- Z. Hu, D. Bongiovanni, D. Jukić, E. Jajtić, S. Xia, D. Song, J. Xu, R. Morandotti, H. Buljan & Z. Chen, Nonlinear control of photonic higher-order topological bound states in the continuum. *Light Sci Appl* **10**, 164 (2021).

### 3.0.1 Higher-order topology

In the previous chapter we have seen how the topological properties are mapped from the momentum space to the real space. In this chapter we continue our inquiry into topological properties of materials. In the introduction to this thesis, we have already touched upon a most peculiar class of systems called the *higher order topological insulators* or HOTIs for short. It is in this chapter that we will study the topological properties of HOTIs. An illustration of a typical HOTI is shown in Fig. 3.1. The defining property of the traditional topological insulators is the fact that they have insulating states in the bulk and conductive states on their edges. HOTIs support other topological states, such as the corner states that can be seen in the illustration in Fig. 3.1. The 'higher-order' part of the acronym refers to the dimensionality of the localized topological state. E.g. the difference in dimension of the bulk and edge state is 1, but the difference in dimension between the bulk and the corner state is 2, i.e. the difference is one order higher. Like any other *topological* insulators, HOTIs possess symmetries responsible for topological protection. Usually those are the chiral symmetry and various crystalline symmetries[56]. The discovery of HOTIs expanded on the concept of topological phase protected by symmetry and on the understanding of the traditional topological insulators. In turn, this

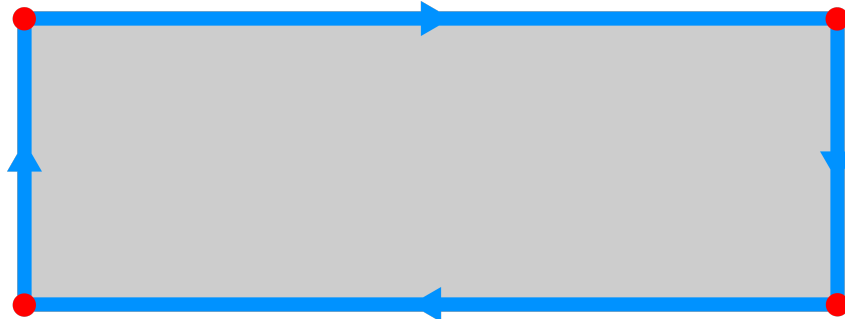


**Figure 3.1:** *Higher order topological insulator.* An Illustration of a 2D HOTI that supports bulk states, edge states and corner states. Such a HOTI has nonconductive bulk states, colored gray in the figure, the topologically protected unidirectional edge modes, here colored blue, and topologically protected localized corner modes, here in red.

has prompted new research into HOTIs in condensed matter physics, electric circuits, acoustics, and photonics [33, 55, 94, 95, 96, 97, 98, 99, 100, 101, 102, 103, 104, 105, 106, 107, 108, 109]. From the fundamental aspect, HOTIs are interesting because of the phenomena such as the higher-order band topology in the twisted Moiré superlattices [110], the topological lattice disclinations [111], and the Majorana bound states [112] and their non-trivial braiding [113]. For applications, they are used in the robust photonic crystal nanocavities [114] and for the low-threshold topological corner state lasing [105, 115].

### 3.0.2 Higher order topological insulators in the linear regime

In general, the HOTIs support  $(d - n)$ -dimensional states at the edges of  $d$ -dimensional lattices with  $n$  no less than 2 [4, 116]. In particular, we are interested in 2-dimensional HOTIs. In addition to the bulk states, that are 2-dimensional, and the edge states, that are 1-dimensional, and that appear in traditional topological insulators, the 2D HOTIs also support *corner states*, that are 0-dimensional, and that propagate unidirectionally. A great example of a 2D HOTI is the 2D *Su–Schrieffer–Heeger (SSH) lattice* [34] shown in Fig. 3.2. The 2D SSH lattice is a square lattice that has two types of bonds called the *intracell* coupling, denoted by  $t$ , and *intercell* coupling, denoted by  $t'$ . Depending on the ratio of the intra- and intercell coupling, the lattice can be in a topologically trivial or topologically nontrivial phase as we will see in the following sections. It is very convenient to introduce a *dimerization* parameter  $c = t - t'$ . For  $c < 0$ , i.e.  $t < t'$ , the lattice is in a topologically nontrivial phase. For  $c > 0$ , it is topologically trivial. Also, at the first glance at the lattice, it is obvious the lattice poses symmetries. In fact, it has two symmetries. It has the chiral symmetry, which means that it looks the same, and that it behaves the same, as its mirror image. It also has the rotational  $C_{4v}$  symmetry,

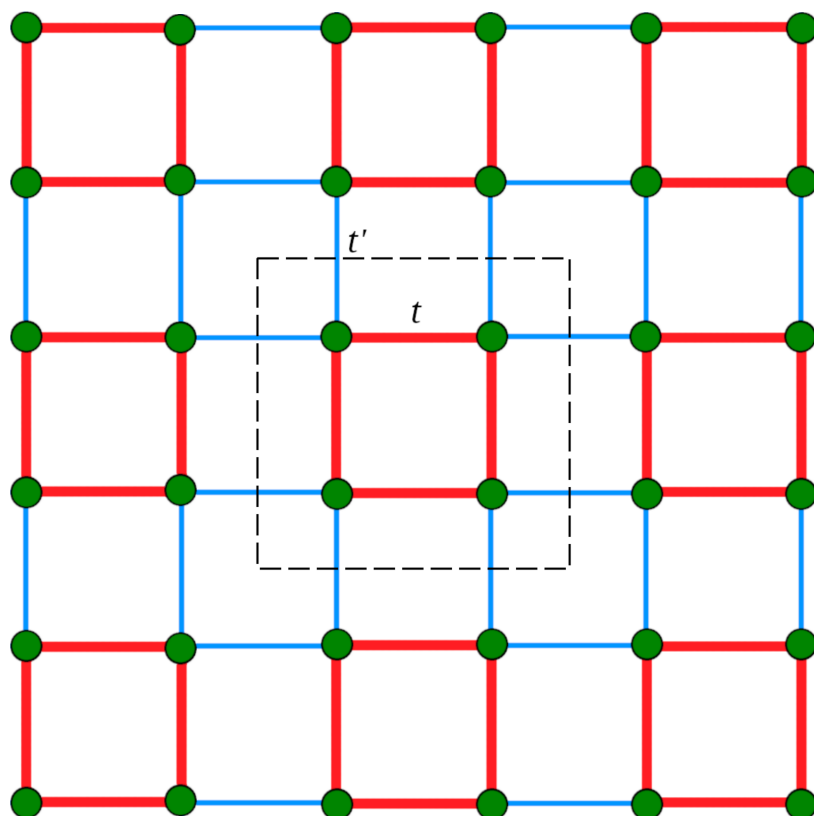


**Figure 3.2:** 2D SSH lattice. The bonds between two nearest neighbouring sites are characterized by two different coupling strengths. The intracell coupling is marked with  $t$  and the intercell coupling is marked with  $t'$ . The lattice is topologically trivial in the case  $t > t'$  and topologically nontrivial in the case  $t < t'$ . The unit cell is marked with a dashed black line.

which is just a fancy way of saying that it looks and behaves the same way if it is rotated by  $90^\circ$ . These symmetries are responsible for the topological protection of the 2nd-order localized states, i.e. the corner states. These states were observed in various synthetic structures [96, 97, 98], including the photonic crystals [100, 101].

### 3.0.3 Nonlinearity in higher-order topological insulators

One of the most important questions in the context of topological insulators is how to change their topological properties. The way to do it is by breaking the relevant symmetries. Then the question is how to do it. One idea is to introduce *nonlinearity* into the system. The combination of topology and nonlinearity leads to a number of fundamental questions, some of which have been addressed in the study of the 1st-order nonlinear topological photonic systems [117]. The examples include the nonlinear topological solitons and the edge states, the nonlinearity-

induced topological phase transitions, the nonlinear topological frequency conversion, and the nonlinear tuning of non-Hermitian topological states [118, 119, 120, 121, 122, 123, 124, 125]. So far, the study of HOTIs has mainly been restricted to the linear regime. However, unexpected phenomena arise when nonlinearity is taken into account in a HOTI systems [126, 127, 128]. Experiments have already been implemented in nonlinear electric circuits [126] and in photonic structures [129, 130, 131]. Our system of choice is, of course, a photonic lattice. In particular, the 2D SSH photonic lattice. The lattice is obtained by writing it into a photorefractive crystal. When a beam propagates through the crystal, it can change its refractive index. This in turn induces a nonlinear response. The nonlinearity can be *self-focusing* or *self-defocusing*. In case of a self-focusing nonlinearity, the beam narrows, and, in the case of a self-defocusing nonlinearity, the beam broadens. We aim to exploit both of these types of nonlinearity in order to change the topological properties of our lattice.

### 3.0.4 Bound states in the continuum

In the context of HOTIs, a phenomena of particular interest, is that of the *bound states in the continuum* (BICs) [55, 56, 57]. BICs are localized states, topological in nature [132, 133, 134], that have eigenvalues in the continuum of extended states, which may result from various mechanisms [133, 134, 135, 136]. In order to understand the connection between HOTIs and BICs, we need to look at the energy spectrum. A typical energy spectrum of a HOTI with BICs is shown in Fig. 3.3. In particular, this is the energy spectrum of a 2D SSH lattice. From the figure, we can differentiate between three types of states. The bulk states are in blue and there is a band gap in-between them. Inside the band gap, we can find the edge states in green. In the middle, a blue strip of states in the *continuum* is visible. Among them are four states marked red. These are the *corner states in the continuum*. In general, in HOTIs with BICs, the corner states appear *right at the center* of the eigenvalue spectrum. They are the zero-energy modes, and they appear in the continuum, and not in the gap, in contrast to other types of HOTIs [102, 104, 137]. These BICs have infinite lifetimes and are fully localized to the corner despite being embedded in the bulk band, but they become “leaky” when the required symmetries are broken [56, 57]. In other words, it is possible to couple the corner states to the other states. Nonlinearity can be used to break the required symmetries and thus enable coupling of light in to or out of these localized corner states, or it can be used to facilitate their interaction. This makes nonlinear HOTI systems with corner states that are also BICs attractive for potential applications.

A nonlinear second-order photonic topological insulators in a Kagome lattice have been reported [138], however, the presence of topologically nontrivial corner states is a topic of debate [102, 106, 104, 139, 140]. In any case, corner modes that are also BICs do not exist in

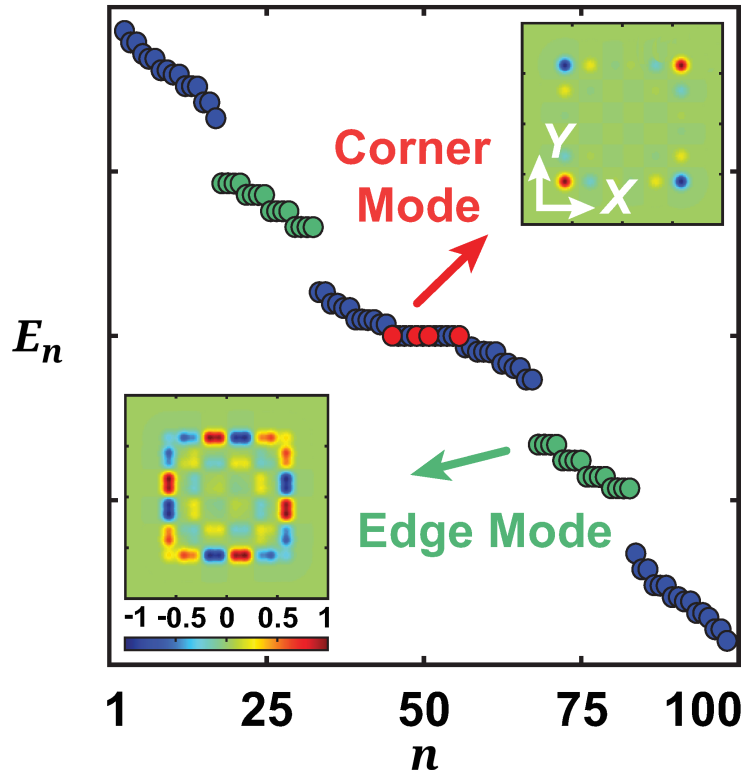


**Figure 3.3:** *Spectrum of a 2D SSH lattice.* The spectrum has the Bloch band structure. The bulk modes are colored blue. The dimerization parameter is  $c = -0.7 < 0$ , and, so, the lattice is topologically nontrivial. The topologically nontrivial states are shown in the insets. The edge modes are in the band gap and are colored green. The corner modes, in red, are in the continuum of the bulk states and have zero energy, i.e. they are BICs. Here, the calculation is done for  $10 \times 10$  lattice sites,  $t = 0.3$  and  $t' = 1.0$ .

those systems.

### 3.0.5 Chapter outline

In this thesis, we study a nonlinear photonic HOTI system and we study the role of nonlinearity in higher-order topological BICs. When nonlinearity is involved, it is often very hard, if not impossible, to calculate anything. Fortunately, we can employ numerical simulations. E.g., the eigenvalues of the system can be calculated numerically. In the experiment, and by using numerical simulations, we demonstrate that a low nonlinearity can induce *coupling between corner states and edge states* in a nontrivial 2D SSH lattice. We show that the coupling between the corner states and the edge states happens for both the self-focusing and the self-defocusing nonlinearity. We will also see that the system exhibits beating oscillations between various modes. Usually, it is expected that the corner states couple to the bulk when the nonlinearity

breaks the relevant symmetries. However, we show that the excitation of the corners leads to the beating between the corner BICs and the edge modes and not between the corners and the bulk. Surprisingly, even a self-defocusing nonlinearity does not favor the coupling to the bulk modes. We theoretically analyze the dynamical evolution of the nonlinear eigenvalue spectrum and show that the corner modes are robust in the process of beating between them and the edge modes. We also show that this beating is driven by a weak nonlinearity. As is the case with other topological states of matter, here too exists a topological invariant. Because we are working with a 2D HOTI, the relevant topological invariant is the Zak phase defined by the Eq. (1.16). Related to the Zak phase, via the Eq. (1.17) is the *polarization* of the system. We calculate the polarization of the system and show that the system can be tuned by the strength of the nonlinearity.

## 3.1 2D Su-Schrieffer–Heeger model

### 3.1.1 Continuous SSH model

The propagation of light in our HOTI system can be described by a Schrödinger like equation of the same form as the Eq. (2.3), with one important addition: Because we are now working with a nonlinear system, a nonlinear term needs to be added to the equation. A continuous nonlinear Schrödinger-like equation (NLSE), typically used for simulating a light field with amplitude  $\Psi_{x,y,z}$  propagating along the longitudinal  $z$ -direction of the photorefractive photonic lattice is given by [80]:

$$i\frac{\partial\Psi}{\partial z} + \frac{1}{2k} \left( \frac{\partial^2\Psi}{\partial x^2} + \frac{\partial^2\Psi}{\partial y^2} \right) - \Delta n \frac{\Psi}{1 + I_L + I_P} = 0, \quad (3.1)$$

where  $I_L(x,y)$  is the intensity of the beam required for writing the 2D SSH lattice in a nonlinear photorefractive crystal,  $I_P$  is the nonlinear contribution of the probe beam that is proportional to  $|\Psi(x,y,z)|^2$ .  $k$  is the wavenumber of the light in the medium, while  $\Delta n(x,y)$  is the linear refractive index change. The induced refractive index change that forms the linear photonic lattice depends on the spatial coordinates  $x$  and  $y$ , and it is uniform along the propagation axis. The propagation of the laser beam through the lattice is illustrated in Fig. 3.4. The nonlinearity can be self-focusing or self-defocusing, depending on the direction of the bias field relative to the crystalline optical axis, while its strength can be controlled by the bias field and the intensity of the beam [80, 141]. For the low power probe beams, i.e. those with small  $I_P$ , the nonlinearity is in the low saturable regime and approximately Kerr-like, i.e.  $\propto |\Psi|^2$ . Then, the NLSE is

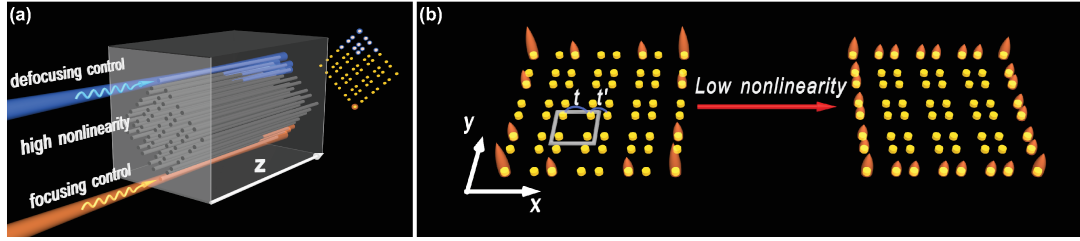


**Figure 3.4:** Illustration of the nonlinear control of a higher-order topological insulator. (a) Schematic of corner excitations in a 2D SSH photonic lattice under the action of high nonlinearity, where a focusing nonlinearity leads to the formation of corner solitons, while a defocusing nonlinearity leads to the radiation into the bulk/edge. (b) Illustration of coupling of, and beating between, corner and edge states under weak nonlinearity.

equivalent to the Gross–Pitaevskii equation that describes the interacting atomic Bose–Einstein condensates in the mean-field approximation [25]. Because of that, and even though we used a specific type of optical nonlinearity in our study, the concept and scheme of nonlinear control of HOTI corner modes developed here are expected to hold in other platforms beyond photonics.

### 3.1.2 Discrete model

The topological features of the 2D SSH lattice are more transparent in the discrete model in the *tight-binding approximation* (TBA). For the 2D SSH model, there are two different couplings between the lattice sites as is shown in Fig. 3.2 and Fig. 3.4(b). In general, they are not equal. One of them,  $t$ , is called the *intracell coupling* and the other,  $t'$  is called the *intercell coupling*. In particular, we will be very interested in how the system behaves for different ratios of  $t$  and  $t'$ . To that end, the *dimerization parameter*  $c = t - t'$  will be most useful because, as we will see, its value differentiates between the topologically trivial and nontrivial phases. The next-nearest-neighbor (NNN) coupling is negligible, so the Eq. (3.1) can be approximated with:

$$i \frac{\partial \psi_\alpha}{\partial z} + \sum_{\alpha'} [H_L]_{\alpha, \alpha'} \psi_{\alpha'} + E'_0 \frac{\gamma |\psi_\alpha|^2}{1 + \gamma |\psi_\alpha|^2} \psi_\alpha = 0. \quad (3.2)$$

where  $\psi_\alpha$  is the complex amplitude of the electric field at the site  $\alpha$  and  $H_L$  is the linear Hamiltonian of the 2D SSH model. The entries in the Hamiltonian matrix,  $[H_L]_{\alpha, \alpha'}$ , are either zero, when  $\alpha$  and  $\alpha'$  are not neighboring sites, or take the value of either the intracell coupling  $t$  or the intercell coupling  $t'$ . Both the normalized bias field  $E'_0$  and the nonlinear coefficient  $\gamma$  control the saturable nonlinearity, which corresponds to the nonlinear photorefractive crystal used in the experiment [80, 141].

### 3.1.3 Band structure in the SSH model

In the discrete model, the topological properties of the linear 2D SSH lattice are revealed in the linear eigenvalue spectrum:

$$H_L \varphi_{L,n} = -\beta_{L,n} \varphi_{L,n}, \quad (3.3)$$

where  $\beta_{L,n}$  is the linear spectrum and  $\varphi_{L,n}$  are the corresponding eigenstates. The eigenvalue spectrum is shown in Fig. 3.5. When the intracell coupling is weaker than the intercell coupling,

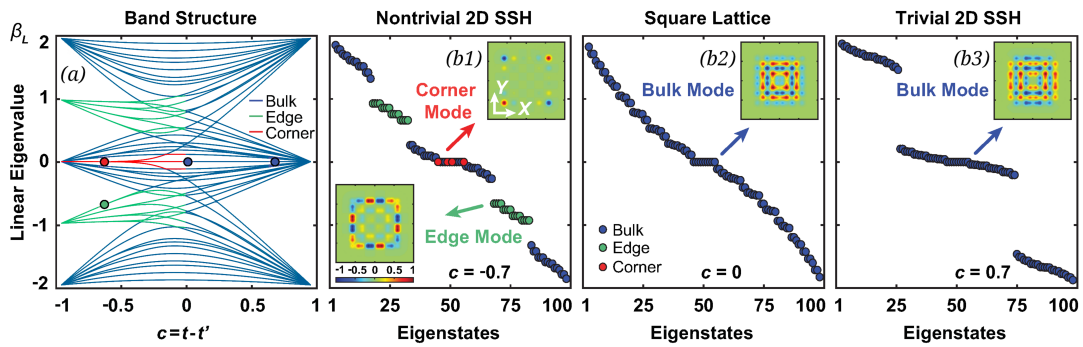


**Figure 3.5:** Linear 2D SSH band structure. (a) Calculated linear eigenvalues  $\beta_L$  of the 2D SSH lattice as a function of the dimerization parameter  $c = t - t'$ , where  $t, t' \in [0, 1]$ . The corner and edge states are highlighted with red and green colors in the highly topologically nontrivial regime. (b1)–(b3) Calculated band structures for the nontrivial ( $t = 0.3, t' = 1.0$ ), square ( $t = 0.5, t' = 0.5$ ), and trivial ( $t = 1.0, t' = 0.3$ ) lattices, show the topological phase transition as the dimerization parameter is tuned. The insets plot the selected mode profiles that correspond to the marked color points. A topological BIC with a characteristic corner-localized mode profile is shown in the upper-right inset of (b1), with zero amplitude in the nearest neighboring sites but nonzero amplitude, and an opposite phase, in the next-nearest-neighbor sites. The calculation is done for  $10 \times 10$  lattice sites.

i.e. when  $c < 0$ , the system is in the topologically nontrivial phase, and the band structure consists of characteristic edge and corner modes that can be seen in Fig. 3.5. In particular, in the middle of the band, there are four degenerated corner modes, shown in 3.5(b1), that correspond to the “zero-energy modes” in the condensed matter language. A typical structure of the corner modes is shown in the upper inset of Fig. 3.5, which clearly displays the features of the topological corner state, i.e. it is highly localized at the corner with zero amplitude in its nearest-neighbor sites but with nonzero out-of-phase amplitude in its NNN sites along the edges. Since these corner states are embedded in the continuum of the SSH lattice, as well as protected by the  $C_{4v}$  and chiral symmetries, they are topological BICs [56, 57]. For comparison, the trivial phase, manifested by vanishing polarizations, occurs when the intracell coupling is

stronger than the intercell coupling  $c > 0$ , which leads to the two mini-gaps that are formed only by the bulk modes shown in Fig. 3.5(b3). When the coupling strength is uniform across the whole lattice, i.e.  $c = 0$ , the lattice turns into a trivial square lattice with a gapless spectrum shown in Fig. 3.5(b2), which sets apart the topologically nontrivial and trivial regimes.

In the nonlinear regime, the eigenvalues are calculated from:

$$H_{\text{NL}}\varphi_{\text{NL},n} = -\beta_{\text{NL},n}(z)\varphi_{\text{NL},n}(z), \quad (3.4)$$

where the nonlinear Hamiltonian:

$$H_{\text{NL}} = H_{\text{L}} + V_{\text{NL}}, \quad (3.5)$$

contains both the linear part and the nonlinear potential that corresponds to the third term in Eq. (3.2). It is important to point out that the nonlinear eigenstates,  $\varphi_{\text{NL},n}(z)$ , and the nonlinear eigenvalues,  $\beta_{\text{NL},n}(z)$  are  $z$ -dependent because the nonlinear beam dynamics are generally not stationary.  $z$  is the normalized propagation distance that plays the role of time. We can use a general theoretical protocol developed recently in [122] to interpret the dynamics in nonlinear topological systems, where both inherited and emergent topological phenomena may arise.

### 3.1.4 Experimental realization of a 2D SSH lattice

In the experiments, we establish the nonlinear photonic HOTI platform by a site-to-site writing of the 2D SSH lattices in a photorefractive crystal, carried out with a continuous-wave (CW) laser [142]. The technique relies on writing the waveguides site by site in a 20-mm-long nonlinear photo-refractive crystal SBN:61 [143] with cerium doping—0.002% CeO<sub>2</sub>. In distinction from the femtosecond laser writing method developed for glass materials [44], the SSH lattices written in the crystal can be readily reconfigurable in terms of lattice spacing and boundary structures. The experimental set-up involves a low-power (up to 100 mW) laser beam with  $\lambda = 532 \text{ nm}$  to illuminate a spatial light modulator (SLM), which creates a quasi-non-diffracting writing beam with variable input positions. For the writing process, we use the modulated light beam, that is ordinarily polarized, with a self-focusing nonlinearity, but for probing, during the nonlinear control process, we employ instead an extraordinarily polarized Gaussian beam for lattice excitation with either a self-focusing or self-defocusing nonlinearity, implemented conveniently by switching the bias field direction [80, 141]. Because of the noninstantaneous photorefractive “memory” effect, all of the waveguides remain intact during the writing and the subsequent probing processes. For the specific SBN crystal we used, the written index structure

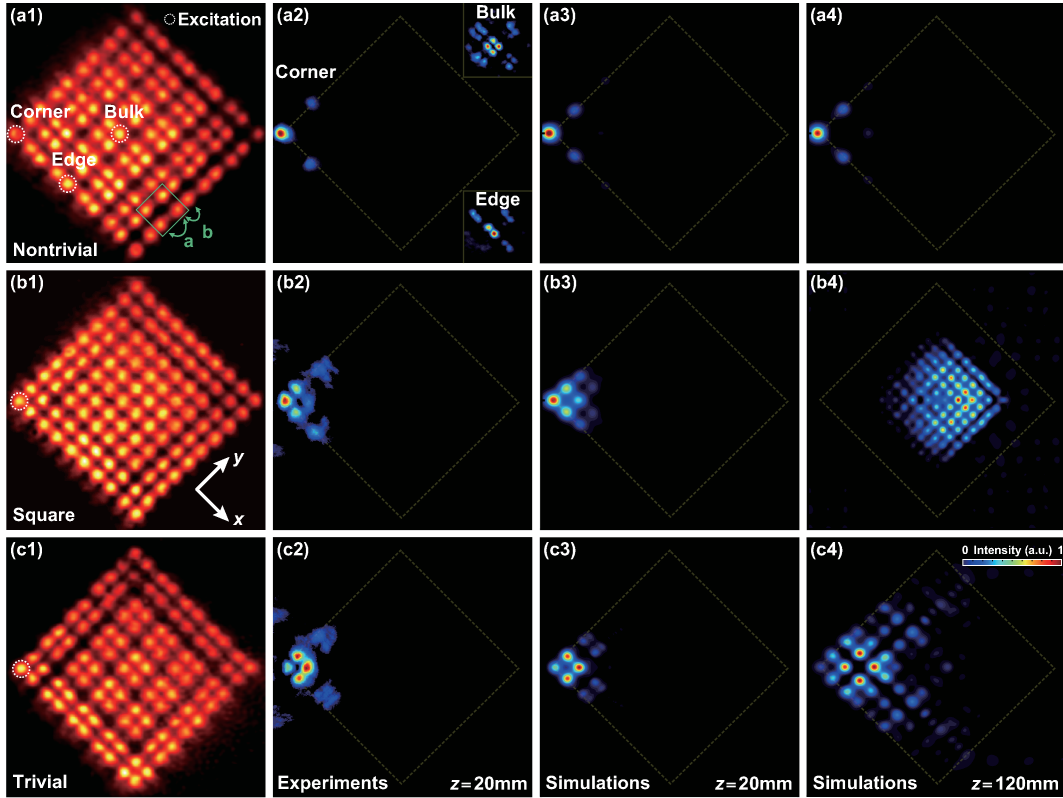


**Figure 3.6:** *Experimental realization and probing of a linear 2D photonic SSH lattices.* (a1)–(c1) Laser-written 2D SSH lattices tuned to the nontrivial, square, and trivial regimes at different dimerizations, where the dashed circles indicate the lattice sites for the corner, edge, and bulk excitations.  $a$  and  $b$  mark the waveguide distances for the weak and strong coupling bonds. (a2)–(c2) Experimental results for a linear output corresponding to the single-site excitations in (a1)–(c1), where the corner excitation in (a1) leads to a localized BIC with evident topological features: no light distribution appears in the nearest neighboring sites, but we observe a non-zero intensity in the next-nearest-neighbor sites along two edges. Discrete diffraction is observed for all other excitations. (a3)–(c3), (a4)–(c4) Numerical results corresponding to corner excitations in (a2)–(c2) obtained using the continuous model, where the propagation distance in (a3)–(c3) is 20 mm, which corresponds to the length of the crystal used in the experiments, and in (a4)–(c4) it is 120 mm, which corresponds to a longer propagation, for direct comparison. Experimental parameters:  $a = 31 \mu\text{m}$ ,  $b = 23 \mu\text{m}$ ; the bias field during the writing process is  $E'_0 = 130 \text{ kV m}^{-1}$ .

persists for several hours in the dark or in the presence of only a weak background illumination, but it can be readily erased with high-intensity white light and overwritten into another structure as needed. Through a multi-step writing approach, the SSH lattice can be reconfigured from a nontrivial to a trivial structure by controlling the lattice spacing between the strong and weak bonds [144]. A linear 2D SSH lattice obtained in the experiment is shown in Fig. 3.6. After the

writing process is complete, the whole lattice structure can be examined by sending a Gaussian beam into the crystal to probe the waveguides one by one, and then the superimposed outputs of the probe beam display the lattice structure as is shown in Fig. 3.6(a1)–(c1). We note that the written waveguides are all single mode since a multi-mode waveguide by optical induction typically requires the formation of spatial solitons in a highly nonlinear regime [145]. It should also be pointed out that, differently from the conventional method of multi-beam induction in a biased crystal [80, 141], here the lattices are written by a CW-laser beam all with a positive bias field [142], so for both trivial and nontrivial lattices, the index changes in all lattice sites follow the intensity distribution of the same writing beam, i.e. there is no “backbone lattice” [80, 141]. After the writing process is completed, the probe beam is used to excite the lattice, and it can undergo either linear propagation, when the bias is turned off, or experience a self-focusing, or self-defocusing, nonlinearity under a positive, or negative, bias field. Of course, the probe beam can locally change the index structure of the lattices due to its self-action during nonlinear propagation—the ingredient needed for the nonlinear control.

For direct comparison, the lattices are written into three different structures, a nontrivial SSH, a square, and a trivial SSH, as illustrated in the left panels of Fig. 3.6 by tuning the dimerization parameter, in accordance with Fig. 3.3(b1-b3), which is achieved by controlling the intracell and intercell waveguide distances in the experiment. We then excite the same corner site with a single Gaussian probe beam. Results obtained under a *linear* excitation are shown in Fig. 3.6, where the probe beam itself has no nonlinear self-action but evolves into a characteristic corner state with a non-zero intensity distribution at the two NNN sites along the edges as can be seen in Fig. 3.6(a2), which represents a typical topological BIC realized in the nontrivial SSH lattice. For all other cases of excitation, either at the edge and the bulk of the nontrivial lattices or at the same corner of the trivial lattices, the probe beam is not localized, but instead displays strong radiation into the bulk/edge as shown in Fig. 3.6(a2)–(c2). To simulate such linear corner excitation, we set  $I_p = 0$  in Eq. 3.1 and display the results obtained from numerical simulations for three different lattices in Fig. 3.6(a3)–(c3), (a4)–(c4), which agree well with our experimental observations.

## 3.2 Simulations in the discrete model

### 3.2.1 Self-focusing nonlinearity

The numerically calculated nonlinear eigenvalue spectrum in the case of self-focusing nonlinearity at  $z = 50$  for the nontrivial SSH lattice is plotted in Fig. 3.7, where two sets of edge modes

set apart the whole band like in the linear spectrum. However, under the action of nonlinearity,

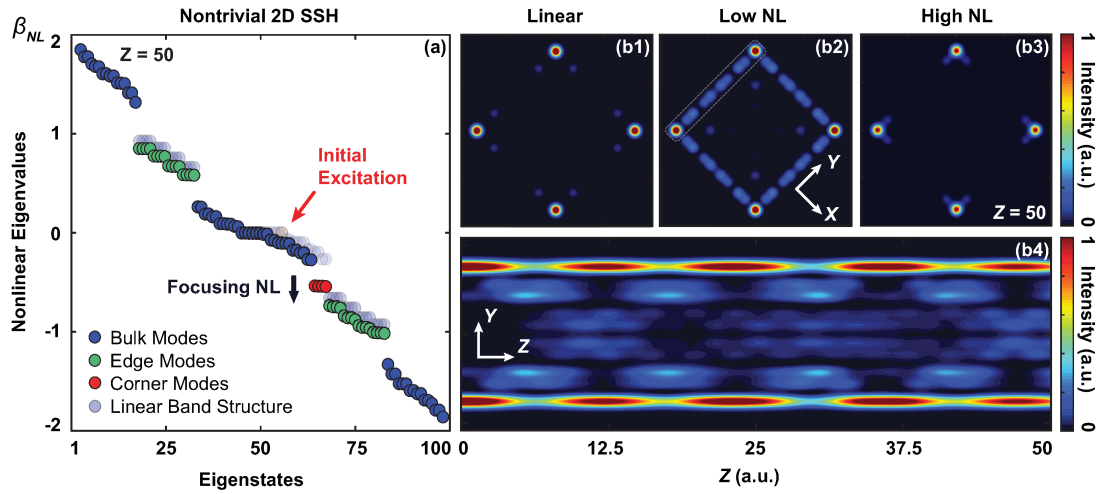


**Figure 3.7:** Calculated nonlinear band structure and corner state tuning under a self-focusing nonlinearity. (a) Calculated nonlinear eigenvalues  $\beta_{NL}$ , at  $z = 50$ , of the 2D SSH lattice for the nontrivial lattice using the discrete model, where the transparent dots are linear states superimposed for direct comparison. The black arrow shows that four corner states, marked with the red dots, undergo coupling and beating with lower edge states under low self-focusing nonlinearity, and the red arrow marks the initially excited corner state that sustains the topological feature under linear conditions as shown in (b1), without any light distribution in the nearest neighboring sites. Under a low focusing nonlinearity ( $E'_0 = 5$ ,  $\gamma = 1.1$ ), the corner state couples with the edge states (b2), and a beating oscillation occurs. This can be clearly seen from the side-view propagation in (b4), taken from the upper-left edge marked by a dashed line in (b2). Under a high focusing nonlinearity ( $E'_0 = 5$ ,  $\gamma = 3.1$ ), a localized semi-infinite gap discrete soliton forms at the corners, with light that is distributed in the nearest neighboring sites, as can be seen in (b3).

the spectrum exhibits a dynamical evolution during the propagation, while the corner modes are forced to couple with the lower edge states by a self-focusing nonlinearity. In other words, they are no longer stationary BICs but rather undergo periodic energy exchange with the edge modes. The robustness of the corner localized BICs in the central bulk band is evident, as they do not want to couple with the bulk modes even when they are driven in and out of the central bulk band via nonlinearity, which reflects the inherited topological nature of BICs. For the snapshot selected at  $z = 50$ , shown in Fig. 3.7(a), the whole spectrum is down-shifted from its linear position by the focusing nonlinearity, while the corner modes are approaching and coupling with the lower edge modes. This direction of the shift is reversed when a self-defocusing nonlinearity is employed. When the strength of nonlinearity is low, for  $E'_0 = 5$  and  $\gamma = 1.1$ , a representative corner mode excited by the focusing nonlinearity undergoes beating with the edge modes as can be seen in Fig. 3.7(b2) and 3.7(b4). Only at a sufficiently high nonlinearity, i.e.  $E'_0 = 5$  and  $\gamma = 3.5$ , it is “liberated” from the continuum and turns into a self-trapped

semi-infinite gap soliton shown in Fig. 3.7(b3). Such corner solitons, which are formed only in the strongly nonlinear regime with eigenvalues that reside beyond the Bloch band, have been explored previously in 2D square lattices [141, 146], but not in the context of HOTIs.

### 3.2.2 Self-defocusing nonlinearity

The numerically calculated nonlinear eigenvalue spectrum in the discrete model is shown in Fig. 3.8.

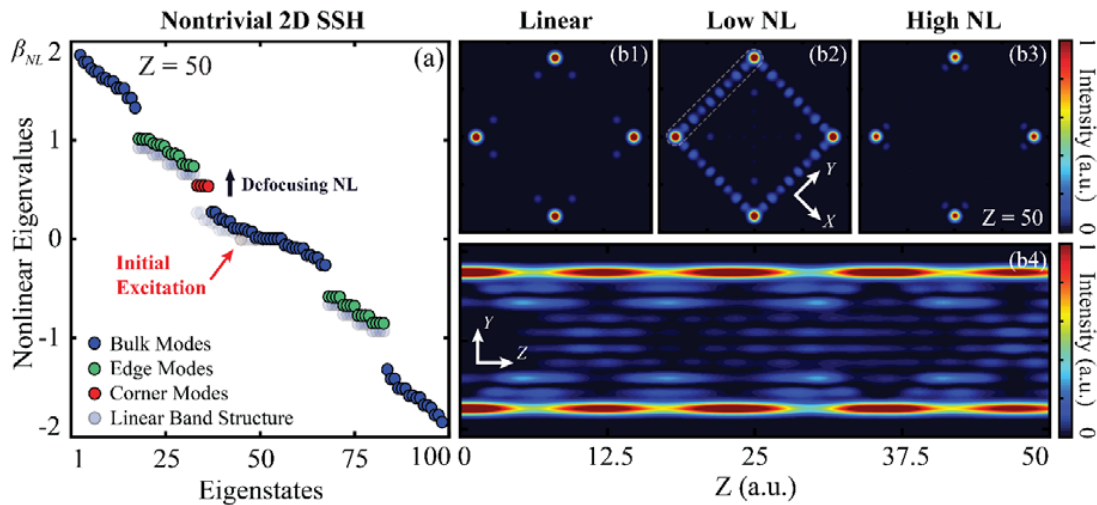


**Figure 3.8:** Calculated nonlinear band structure and corner mode tuning under a self-defocusing nonlinearity. (a) Calculated nonlinear eigenvalues  $\beta_N$  for the nontrivial 2D SSH lattice using the discrete model taken at  $z = 50$ . The transparent dots are the linear eigenvalues that are plotted here for direct comparison. The black arrow points out that the four corner states, marked by the red dots, undergo coupling and beating with the upper edge states under a low nonlinearity. The red arrow marks the initially excited corner mode, which possesses the topological features in the linear case, without any light distribution in the nearest neighboring sites as is shown in (b1). Under a low self-defocusing nonlinearity ( $E'_0 = -5$ ,  $\gamma = 1.1$ ), the corner state couples with the edge modes (b2) and the beating oscillations occur, as can be clearly seen from the side-view propagation in (b4), where we plot the intensity profile of the upper-left edge marked by a dashed line in (b2). Under a high defocusing nonlinearity ( $E'_0 = -5$ ,  $\gamma = 1.1$ ), a corner-localized soliton-like pattern emerges (b3), which is quite different from the linear topological corner state shown in (b1). This can be inferred by looking at the nearest neighboring sites: the localization in this case is driven by nonlinearity, rather than topology.

The numerical simulations are performed via the discrete NLSE model of Eq. (3.2). In the *linear* regime, where  $E'_0 = 0$ , the nontrivial band structure is stationary, i.e., it is independent of the dimensionless propagation distance  $z$ , and it exhibits three main bands associated with extended bulk modes, plus the two sets of edge modes that reside in the mini-gaps. Additionally,

it also displays four corner states with eigenvalues equal to zero represented by the red dots in Fig. 3.8(a), which are embedded in the middle bulk band in the continuum. Because of this, they are the topological bound states in the continuum. Without loss of generality, the leftmost corner mode of the linear band structure is excited initially to test the effect of the nonlinearity. In the *nonlinear* regime where  $E'_0 \neq 0$ , the spectrum evolves dynamically during the propagation due to the action of the defocusing nonlinearity. The edge states remain close to their linear positions. In contrast, the nonlinear corner states move away from the middle band by experiencing an upward shift, eventually leading to the interaction and the beating with the edge states in the upper band at a low nonlinearity. A snapshot of the nonlinear spectral evolution is retrieved at the distance  $Z = 50$  for a low self-defocusing nonlinearity with  $E'_0 = -5$  and  $\gamma = 1.1$  showing the whole spectrum shifted up from its linear position and the corner states approaching the upper edge states. The beating and the energy exchange taking place between the edge states and the corner states can be unveiled by looking at the transversal and longitudinal intensity distributions of the output beam in Fig. 3.8(b2) and in Fig. 3.8(b4), which significantly deviates from the stable output profile of the corresponding linear corner state in Fig. 3.8(b1). Counterintuitively, the robustness of these corner localized BICs is also preserved for the defocusing nonlinearity: Similar to the self-focusing case, they do not couple with the bulk modes when moving in and out of the central bulk band. For a sufficiently high defocusing nonlinearity, i.e.  $E'_0 = -5$  and  $\gamma = 3.5$ , the corner states are driven away from the continuum band, forming soliton-like nonlinear mode patterns. A typical example is shown in Fig. 3.8(b3). These results, calculated using the discrete model under a self-defocusing nonlinearity are nearly identical to those obtained under a self-focusing nonlinearity, which might be related to the chiral symmetry of the underlying linear system. However, it is worth mentioning that, in general, the results obtained from the discrete and the continuous models tend to deviate in the highly nonlinear defocusing regime as we will see later. We note that here, the convention used for calculating the eigenvalues is such that the self-focusing pushes the eigenvalues downwards, as was seen in Fig. 3.7, whereas the self-defocusing moves them upwards as can be seen in Fig. 3.8, to keep the analogy with condensed matter systems. In optics, this, nonlinearity-driven, up- and down-shifting directions could be reversed depending on how we define the propagation constant and plot the eigenvalue spectrum. More specifically, Eq. (3.2) reads

$$i \frac{\partial \psi}{\partial z} + H_{NL} \psi = 0. \quad (3.6)$$

By using the condensed matter sign convention in the phase exponent  $\psi = \varphi_{NL,n} \exp(-i\beta_{NL,n}z)$ ,

we obtain the eigenvalue spectrum given by Eq. (3.3).

### 3.2.3 Beating between corner modes and edge modes

In previous sections, we have mentioned the beating between the corner states and the edge states in our 2D SSH lattice under the action of nonlinearity. Here we will look more closely at the beating between these states. We can start with the linear BIC profile shown in Fig. 3.3(b1) for the discrete model, where there seems to be some background distribution inside the topological structure for the corner state. This is because the lattice structure is not large enough and as such, the “tails” of the corner modes seem to extend over the lattice structure. To show that this is not due to coupling with the bulk modes, which should not occur for the true BICs, we recalculated the corner state and plot its profile in Fig. 3.9 with a doubled lattice size, which comes out to  $20 \times 20$  sites. The linear envelope in the logarithmic scale in Fig.

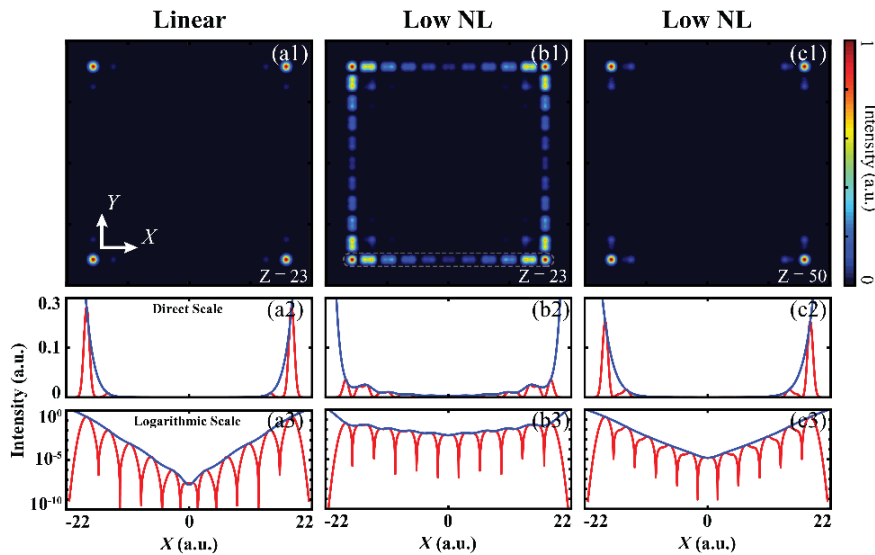


**Figure 3.9:** *Localization of corner states.* Intensity plots of a corner mode in both the (a) linear ( $E'_0 = 0$ ) and the (b)-(c) weakly nonlinear regimes ( $E'_0 = \pm 5$ ,  $\gamma = 1.1$ ). The results were obtained using parameters corresponding to Fig. 3.5 and Fig. 3.7, but with a double-sized ( $20 \times 20$ ) 2D SSH lattice structure. In the nonlinear regime, the corner mode undergoes periodic oscillation between a mixed corner/edge state (b) at  $z = 23$  and an isolated corner state (c) at  $z = 50$ , with no radiation into the bulk. Top panels are transverse intensity patterns, while the bottom panels are corresponding intensity profiles in direct and logarithmic scales. The linear envelope in the logarithmic scale proves the exponential localization of the corner modes.

3.9 shows the exponential localization of the corner modes. For the beating oscillation induced by nonlinearity and described in Fig. 3.7, we also performe the calculation for the nonlinear

corner modes within a larger lattice. Snapshots are plotted in Fig. 3.9(b) at  $Z = 23$ , and Fig. 3.9(c) at  $Z = 50$ . At  $Z = 23$ , the corner state couples with an edge state; the intensity does not exhibit an exponential decay along the edges, yet there is no radiation into the bulk. At  $Z = 50$ , the corner state tends to restore its topological BIC feature, as clearly seen from the intensity plots in Fig. 3.9(c3). This beating process goes back and forth periodically. It occurs for both the self-focusing and the self-defocusing nonlinearities, but it cannot occur in the topologically trivial structure. Strictly speaking, the nonlinear corner modes are no longer stationary BICs as they are in the linear regime, but they undergo periodic coupling with the edge states without dissipating into the bulk, indicating the inherited topological nature of the corner states, even under nonlinear action.

### 3.3 Numerical methods for the continuous model

#### 3.3.1 Beam propagation simulation

The evolution of a light beam propagating in a photonic lattice can be obtained by numerically solving Eq. (3.1). The propagation is done using the split-step Fourier technique, also referred to as the beam propagation method (BPM). The 2D SSH lattice structure has four lattice sites per unit cell, as can be seen in Fig. 3.2, which gives us:

$$I_L(x, y) = \sum_{s=1}^4 \sum_{i=0}^{N/4-1} \sum_{j=0}^{N/4-1} I_{L0} \exp\left(-\frac{(x - a_{sij})^2}{w_0^2/2} - \frac{(y - b_{sij})^2}{w_0^2/2}\right), \quad (3.7)$$

where:

$$(a_{1ij}, b_{1ij}) = (iT, jT), \quad (3.8)$$

$$(a_{2ij}, b_{2ij}) = (a + iT, jT), \quad (3.9)$$

$$(a_{3ij}, b_{3ij}) = (iT, a + jT), \quad (3.10)$$

$$(a_{4ij}, b_{4ij}) = (a + iT, a + jT). \quad (3.11)$$

$T = a + b$  is the lattice period, and  $a$  and  $b$  are the spacing between the lattice sites for the weak and the strong bonds that correspond to the intracell and the intercell coupling in Fig. 3.2, respectively. The total number of unit cells is  $N^2/4$ , where  $w_0$  is a scaling factor and  $I_{L0}$  is the lattice magnitude. In the experiments, depending on the relative values of  $a$  and  $b$ , the photonic lattice can be reconfigured into a simple square lattice for  $a = T/2$ , a nontrivial SSH lattice for  $a > T/2$  and a trivial SSH lattice for  $a < T/2$ . We numerically excite only one corner, the left

one in Fig. 3.6, with a Gaussian beam and perform BPM simulations for subsequent dynamics under linear and nonlinear conditions. Linear propagation results obtained with different lattice parameters are illustrated in Fig. 3.6(a3–c3) and Fig. 3.6(a4–c4). For the nonlinear regime, i.e. for  $I_P \neq 0$ , the simulations are performed for both the self-focusing and the self-defocusing nonlinearities in the nontrivial SSH lattice, and the results obtained at low and high nonlinearity are in good agreement with experimental observations.

### 3.3.2 Long-range propagation of BICs

To see the *beating* between the corner states and the edge states, under the action of nonlinearity, more clearly, in Fig. 3.10, we show numerical simulation results for long-distance propagation of the states in the 2D SSH lattice using the continuous model. In the linear regime, a corner state remains localized without coupling to the edge or bulk states. To match our experimental conditions, we launch a single beam into the waveguide in the corner, so we cannot say that the whole corner state is excited, but rather a large portion of it. Clearly, even for a long-distance propagation, most energy of the probe beam remains localized in the excited corner site. The weak oscillation of the intensity happens because we do not excite the exact corner state, but just one corner. In the right panel of Fig. 3.10, a weak self-focusing nonlinearity is applied, where the corner mode undergoes periodic intensity oscillations due to the beating with the edge state. The period of such beating oscillation is nearly 20 cm, much longer than the crystal length used

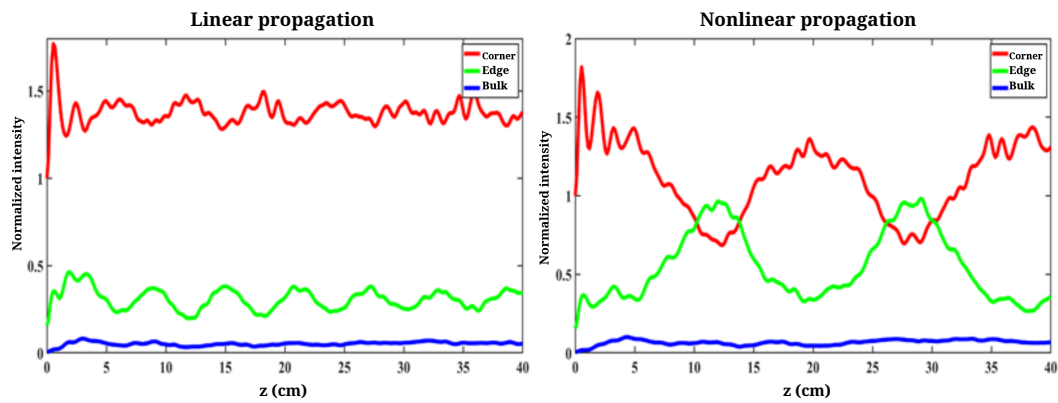


**Figure 3.10:** Numerical simulation of the long-distance propagation of the states in a photonic HOTI. On the left: linear regime, where the corner mode remains localized without the coupling between the edge and the bulk modes. On the right: weakly, self-focusing, nonlinear regime, where the average power in the corner sites undergoes a periodic oscillation due to the beating with the edge mode, but not with the bulk mode. The parameters used are:  $a = 31 \mu\text{m}$ ,  $b = 23 \mu\text{m}$ ,  $I_{L0} = 0.5$ ,  $w_0 = 15.75 \mu\text{m}$ .

in our experiments (which is only 20 mm). Interestingly, this kind of beating oscillation occurs

even under a weak self-defocusing nonlinearity, although the defocusing nonlinearity speeds up the oscillation due to enhanced diffraction and coupling to the edge modes.

## 3.4 Nonlinear control of HOTIs

### 3.4.1 Nonlinear control of HOTIs in the experiment

So far, we have seen that the topological properties of the nonlinear 2D SSH lattice depend on the nonlinearity itself. One of the phenomena is the beating between the corner states and the edge states. The beating does not happen in the linear system, only in the nonlinear system. It is, also, of great interest to see how the strength of the nonlinearity affects the topological properties of our system and how can we use the nonlinearity to control the system. In this section, we discuss the nonlinear control of HOTI corner states that was seen in the Fig. 3.8 and the Fig. 3.7. Measurements of the output intensity profile of the probe beam under a corner excitation of the nontrivial lattice with both self-focusing and self-defocusing nonlinearities after a 20 mm propagation are shown in Fig. 3.11. The linear output of the topological corner state is plotted for reference in Fig. 3.11(a). At a low nonlinearity, a direct comparison with the linear output shows that the state localized in the corner differs in this case from the topological corner state, because now the energy goes to the second nearest neighbor and even to the fourth sites along the edges as can be seen in Fig. 3.11(b) and Fig. 3.11(e). This is because of the nonlinearity-induced coupling between the corner states and the edge states. In the experiments, because the propagation distance set by the crystal length is typically smaller than the beating period, we cannot observe the distinct beating oscillation between the corner states and the edge states that is numerically shown in Fig. 3.7(b4). At a high self-focusing nonlinearity, the probe beam is localized again in the corner, forming a self-trapped semi-infinite gap corner soliton [141, 146] as shown in Fig. 3.11(c), also in agreement with what is illustrated in Fig. 3.7(b3). On the other hand, at a high defocusing nonlinearity, the corner excitation leads to strong spreading of the energy into the bulk as well as into the edges as can be seen in Fig. 3.11(f) due to the nonlinear mode beating involving the bulk states in the higher band. These experimental results are corroborated by our numerical simulations based on the NLSE in the Eq. (3.1).

### 3.4.2 Simulation of nonlinear control of HOTI

To corroborate the experimental observations related to nonlinear control of the HOTIs presented in Fig. 3.11, we perform numerical simulations via the split-step Fourier transform

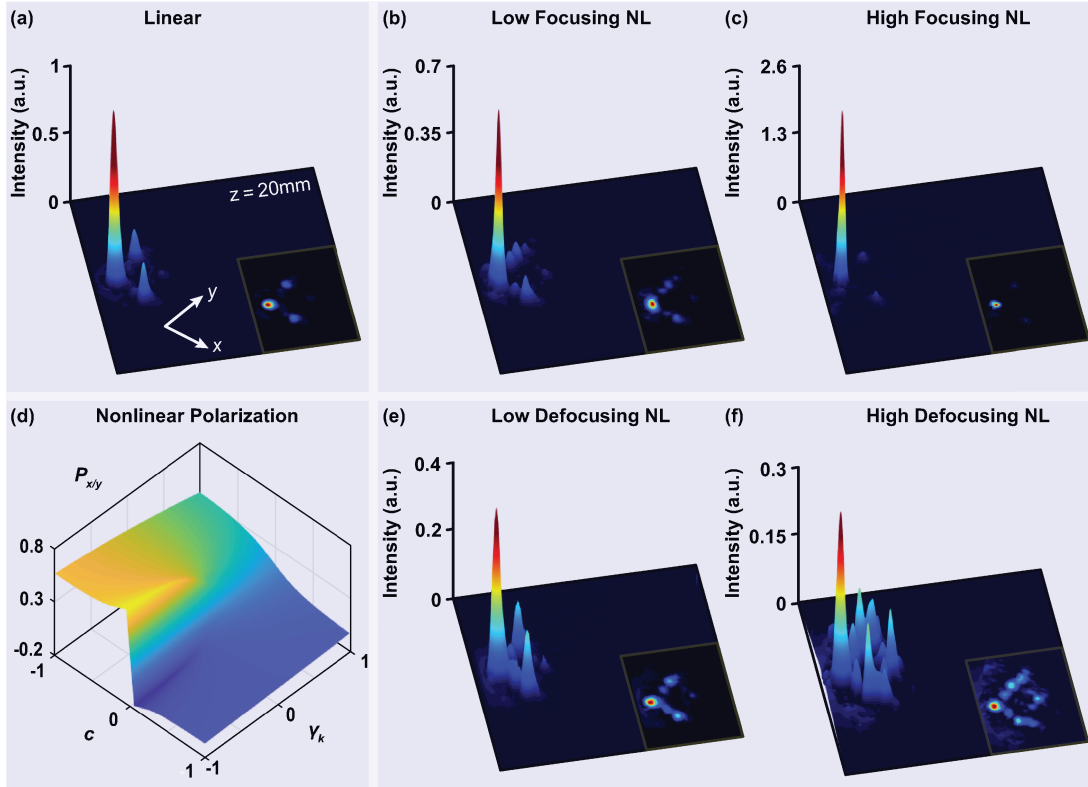


**Figure 3.11:** *Experimental demonstration of the nonlinear control of a higher-order topological insulator.* (a) A 3D view of a typical linear corner state experimentally observed in a nontrivial lattice. (b), (c) Nonlinear self-focusing leads to (b) the coupling into the edges (non-zero intensity along the edge sites compared to the linear case) when the nonlinearity is low and to (c) a highly localized corner soliton when the nonlinearity is high. (d) Plot of the calculated nonlinear polarization as a function of the nonlinear control parameter  $\gamma$  as well as the dimerization parameter  $c$ . Characteristic jump in the bulk polarization shows that the topological phase transition extends beyond the linear regime ( $\gamma = 0$ ) because of the inherited topology in the nonlinear regime. (e), (f) Experimental results of the nonlinear control with a low and high self-defocusing nonlinearity. Under a high defocusing nonlinearity, the energy spreads dramatically to both the edge and the bulk (f). For the focusing (defocusing) case, the bias field is  $E'_0 = 160\text{kVm}^{-1}$  ( $E'_0 = -80\text{kVm}^{-1}$ ), and the average power of the probe beam is about  $15\text{nW}$  ( $70\text{nW}$ ) for the low (high) nonlinearity.

method, applied to the continuous paraxial nonlinear Schrödinger-like equation given by Eq. (3.1).  $\Psi(x, y, z)$  is the electric field envelope of the probe beam, whose intensity is  $I_p$ .  $I_L = I_L(x, y)$  is the intensity of the linear 2D SSH lattice. Here  $x$  and  $y$  are the transversal coordinates, while  $z$  is the propagation distance. Furthermore,  $k$  is the wavenumber of the light in the medium, while  $\Delta n$  is the linear refractive index change determined by the bias field  $E'_0$  via  $\Delta n = kn_e^2 r_{33} E'_0 / 2$ , where  $n_e = 2.35$  and  $r_{33} = 280\text{pmV}^{-1}$  are, respectively, the bulk refractive index and the electro-optic coefficient for extraordinarily polarized light in the photorefractive SBN:61 crystal. In

principle, the overall index potential,  $\Delta n/(1 + I_L + I_P)$ , depends on the intensities of both the lattice-writing and the probing beams, as well as the bias field  $E'_0$ . Here we assume that the lattice index potential is set only by  $E'_0$ , and simply let  $I_P = \eta|\psi(x, y, z)|^2$  to control the nonlinearity induced by the probe beam. In the continuous model, we use the parameter  $\eta$  to address the nonlinearity, as opposed to  $\gamma$  in the discrete model, because they are, in general, not equal. However, they are equivalent, and can be made equal by a proper choice of parameters. Therefore, for the linear case,  $\eta = 0$ . For a positive value of  $\eta$ , the nonlinearity is self-focusing, while for the negative value it is self-defocusing. This can properly simulate the experimental situation in the low saturation regime. Numerical results for a 20mm-long propagation, i.e. for the crystal length used in the experiments, obtained from simulations with Eq. (3.1) are presented in Fig. 3.12 for different conditions, corresponding to the experimental results presented in Fig. 3.11. Fig. 3.12 also illustrates the output intensity profiles of the probe beam under a single corner excitation for a 2D SSH nontrivial lattice. Parameters in simulations are taken corresponding to the experimental setup. The 2D SSH lattice structure is defined with  $I_L$  in Eq. (3.1). For the nontrivial lattice, the intra-cell and the inter-cell distances are taken as  $a = 31 \mu\text{m}$  and  $b = 23 \mu\text{m}$ , the linear potential depth is  $I_L = 0.5$ , and the scaling factor is  $w_0 = 15.75 \mu\text{m}$ . The intensity pattern of such a nontrivial lattice is illustrated in Fig. 3.12(d). The probe beam has a Gaussian profile with dimensions comparable to that of a lattice site. For simulations, we take  $\Delta n = 2.36 \times 10^{-4}k/n_e$  for both the linear case and the nonlinear defocusing case and  $\Delta n = 2.9 \times 10^{-4}k/n_e$  for the nonlinear focusing case. Fig. 3.12(a) illustrates the output probe beam with the characteristic features of the topological corner state under the linear condition  $\eta = 0$ . For the low focusing nonlinearity,  $\eta = 0.03$  and the low defocusing  $\eta = -0.05$  nonlinearity, the localized corner state differs from that of the topological linear system because the beam energy spreads in the nearest neighbor sites along the two edges as can be seen in Fig. 3.12(b) and Fig. 3.12(e). This is due to the coupling between the corner states and the edge states induced by the nonlinearity. However, at a high self-focusing nonlinearity  $\eta = 0.15$ , the probe beam localizes again at the corner site of the lattice, but its intensity pattern does not have the features of a topological corner state. In fact, it forms a self-trapped semi-infinite gap corner soliton as can be seen in Fig. 3.12(c). In contrast, at a high defocusing nonlinearity,  $\eta = 0.15$ , the corner excitation leads to a strong spreading of the energy into both the bulk and the edges, as shown in Fig. 3.12(f). These numerical results are in good agreement with the experimental observations shown in Fig. 3.11.

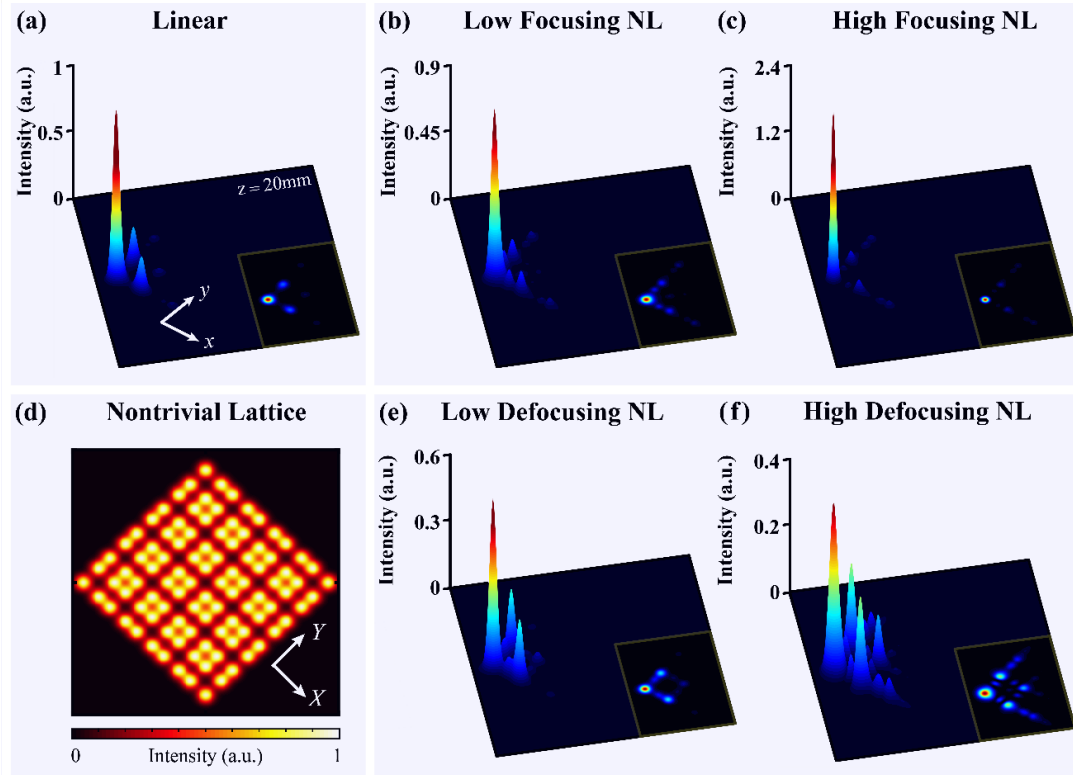


**Figure 3.12:** Numerical simulation of the nonlinear control of a photonic higher-order topological insulator. (a) A 3D-view of a linear corner state after a 20 mm-long propagation through a nontrivial 2D SSH lattice. (b, c) Nonlinear self-focusing leads to (b) the coupling of the corner mode to the edges (non-zero intensity in the edge sites compared to the linear case) when the nonlinearity is low, and (c) a highly localized corner soliton when the nonlinearity is high. (d) Transversal intensity distribution of the 2D SSH photonic lattice used in simulations. (e, f) Nonlinear output under a self-defocusing nonlinearity that corresponds to (b), (c), that shows strong energy spreading into both the edge and the bulk sites at a high strength of the nonlinearity. Parameters are:  $a = 31 \mu\text{m}$ ,  $b = 23 \mu\text{m}$ ,  $I_{L0} = 0.5$ ,  $w_0 = 15.75 \mu\text{m}$ .

### 3.4.3 Polarization calculation

To characterize the topological properties of the 2D SSH lattices, we calculate the topological invariant based on the 2D polarization, which is defined for an infinite periodic system as [100, 101]:

$$P_i = -\frac{1}{(2\pi)^2} \iint dk_x dk_y \text{Tr}[A_i(k_x, k_y)], \quad (3.12)$$

where  $i = x, y$  and:

$$(A_i)_{mn}(\mathbf{k}) = i \langle u_m(\mathbf{k}) | \partial_{k_i} | u_n(\mathbf{k}) \rangle \quad (3.13)$$

is the the Berry connection, and  $u_m(\mathbf{k})$  is the eigenmode in the  $m$ -th band. The 2D polarization is directly related to the 2D Zak phase:

$$Z_i = 2\pi P_i. \quad (3.14)$$

One can readily calculate the polarization in the linear regime, which yields [147]:

$$P_x = P_y = \frac{1}{2} \text{ for } c < 0, \quad (3.15)$$

$$P_x = P_y = 0 \text{ for } c > 0. \quad (3.16)$$

In order to test whether the signature of the topological phase transition at  $c = 0$  is still present in the nonlinear regime, we calculate the nonlinear polarization by employing Eq. 3.12 for the following modified Hamiltonian applied to the 2D SSH lattices [147]:

$$H = \begin{pmatrix} \gamma_k & t + t' \exp(-ik_x) & t + t' \exp(-ik_y) & 0 \\ t + t' \exp(ik_x) & 0 & 0 & t + t' \exp(-ik_y) \\ t + t' \exp(ik_y) & 0 & 0 & t + t' \exp(-ik_x) \\ 0 & t + t' \exp(ik_y) & t + t' \exp(ik_x) & 0 \end{pmatrix}, \quad (3.17)$$

where  $\gamma_k$  accounts for the nonlinearity strength, and its sign manifests the difference between the self-focusing and the self-defocusing nonlinearities. This Hamiltonian corresponds to the excitation of one out of the four lattice sites in all the unit cells and changing its on-site potential via the employed nonlinearity. Calculated results for the nonlinear polarization are plotted in Fig. 3.11(d), as a function of the dimerization parameter  $c = t - t'$ . The nonlinearity  $\gamma_k$  breaks the symmetry protection of the two distinct topological phases. However, we can still use polarization calculations to quantify the notion that the weakly nonlinear system can inherit topological properties from the linear system. More specifically, in Fig. 3.13 we plot the nonlinear polarization as a function of the nonlinearity  $\gamma_k$  for several values of the parameter  $c$ , which are chosen in both the trivial and nontrivial regime. We observe that the polarization slightly deviates from the linear case, where  $\gamma_k = 0$ , i.e., from  $P_x = P_y = 1/2$  when  $c < 0$ , and from  $P_x = P_y = 0$  for  $c > 0$ . However, we also notice that the deviation is such that, for weak nonlinearities, i.e. for small  $|\gamma_k|$ , it grows only linearly with the nonlinearity parameter  $\gamma_k$ . In other words, if we imagine nonlinearity as a small perturbation of the corresponding linear system, we see that the characteristic topological features of the linear system, e.g. a sudden jump in the polarization will be inherited in the nonlinear system as well.

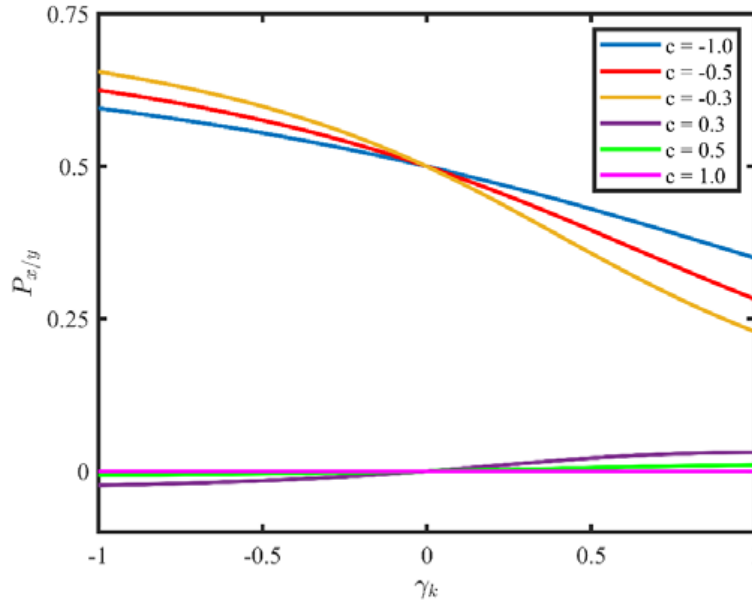


**Figure 3.13:** Polarization of the nonlinear 2D SSH system as a function of nonlinearity. The polarization  $P_x = P_y$  of the nonlinear system depends on the strength of the nonlinearity parameter  $\gamma_k$ . For the linear systems, where  $\gamma_k = 0$ , we know that  $P_x = P_y = 1/2$  in the nontrivial regime, for which  $c = 0$ , and  $P_x = P_y = 0$  in the trivial regime, for which  $c > 0$ . For weak nonlinearities, the deviation of the nonlinear polarization from this result increases linearly with the strength of the nonlinearity parameter  $\gamma_k$ .

### 3.5 Chapter conclusion

The concept of topologically protected higher-order BICs, which is explored here under the action of nonlinearity, is somewhat an oxymoron. If two states are close in energy, or, in the language of optics, the propagation constants are close, then it should be easy to couple these states. In a nonlinear HOTI system, topology is involved in the dynamics, and, so, for the system studied here, this common sense is questioned. In our theoretical simulations and experiments, we have found that topological higher-order BICs, which are corner states of our nonlinear 2D SSH lattice, dominantly couple to the edge states rather than bulk states. This happens despite the fact that the corner-localized BICs are embedded in the continuum of the bulk states, and gapped from the edge states, as is clearly illustrated in Fig. 3.5(b1). A weak self-focusing or self-defocusing nonlinearity, for practically all excitations employed here, breaks the chiral symmetry and the crystalline symmetry of the lattice. The only exception is the excitation in Fig. 3.7, which preserves the  $C_{4v}$  symmetry. By breaking these symmetries, nonlinearity, in principle, allows the corner states to couple with the bulk states of the continuum in which they are embedded [56]. However, the overlap with the edge states induced by the nonlinearity is obviously much larger, which leads to the dominant coupling between the corner states and

the edge states. It should be noted that this behavior depends, also somewhat unintuitively, on the dimerization parameter  $c$ . If its magnitude increases, on the highly topologically nontrivial side, the gap between the topological corner BICs and the edge states increases as can be seen in Fig. 3.5(a), yet the dominant corner–edge coupling persists as opposed to the corner–bulk coupling. A feature of interest for technological applications is the possibility to nonlinearly couple two corners; such coupling was proposed with exciton–polariton corner modes [127]. From the simulations presented in Fig. 3.7, it follows that such coupling should be possible in our lattice. Namely, if one excites a single corner, the initial state is then a superposition of four corner states that will beat. Another view of the dynamics is that the nonlinearity will enable coupling to the edge states and then to the adjacent corner. This type of dynamics is verified in our numerical simulation under proper initial conditions. It should be noted that, for our experiment, the longest crystal we can possibly obtain has a length of only 20 mm, which corresponds to only a few coupling lengths between adjacent waveguides, a much smaller value than the beating oscillation period which is around 200 mm long along the propagation direction as can be seen in Fig. 3.10. Therefore, it is not possible to experimentally observe the beating dynamics presented in Fig. 3.7 within the length of the nonlinear crystal. However, by using longer samples with different lengths, or by using different platforms with stronger coupling, such beating oscillations should be observed.

The distinction between the discrete and the continuous models under large nonlinearities merits further discussion. The continuous NLSE of Eq. (3.1) offers a quantitatively better description of the experiment than the discrete model in Eq. (3.2) under the tight-binding approximation. However, it is well known when the two models start to deviate. For a linear lattice that is sufficiently deep, the discrete model is a good approximation of the dynamics; the parameters of the linear lattice employed here are in this regime. When the nonlinearity is weak, the lattice will not be strongly perturbed, and the discrete model is still a good approximation. However, for a large self-defocusing nonlinearity, the whole lattice structure at the excitation can be strongly deformed. For example, if a corner gets excited, a large self-defocusing nonlinearity significantly molds the corner area and enables coupling between the NNN sites and changes the nearest-neighbor coupling as well, which is not captured by the discrete model of Eq. (3.2). In contrast, for a large self-focusing nonlinearity, the whole lattice structure is preserved despite the deep potential at the excitation site. In particular, we found that the discrete model is still qualitatively accurate for the presented self-focusing dynamics. In general, for a weak nonlinearity and practically any excitation, the symmetries responsible for the nontrivial topology of the 2D SSH model are broken [130]. However, in a weakly nonlinear system, the topological properties can persist as they are inherited from the corresponding linear system

[122]. This is the origin of the weak nonlinear coupling between the corner and the bulk modes discussed above. The fact that the topological properties are inherited is quantified and illustrated in Fig. 3.11(d), showing the bulk polarizations  $P_x$  and  $P_y$ , that are related to the 2D Zak phase, as a function of the parameter  $c$  and the strength of the nonlinearity  $\gamma_k$ . The nonlinear system that corresponds to Fig. 3.11(d) is a 2D SSH lattice with one out of four lattice sites in all unit cells excited, i.e., its on-site refractive index is changed in comparison to the other three sites in the unit cell. Even though this is a specific nonlinear excitation, it serves well to quantify how the topological feature is preserved after nonlinearity is introduced. It is well known that, for the linear 2D SSH lattice, the polarizations are topologically quantized;  $P_i = 1/2$  for  $c < 0$ , and  $P_i = 0$  otherwise [147]. In the nonlinear case, the symmetry and topological protection are, strictly speaking, broken. However, there is a sharp jump in the polarization as  $c$  crosses zero, which is inherited from the topological phase transition occurring in the underlying linear system. We see that the jump, that indicates this phase transition, is preserved in the nonlinear system as well. We expect that such inherited nonlinear topological properties exist also in HOTIs of the third- or even higher-order that form in synthetic dimensions.

Finally, the ongoing debate about the use of breathing Kagome lattices for illustrating HOTI states merits further discussion, especially with respect to the work in [138]. First, our work focuses on the topological BICs and their tunability by nonlinearity in a 2D SSH lattice, but such states do not exist in the Kagome lattice studied in [138], which clearly distinguishes the two independent studies [129, 130]. Second, there is a fundamental difference between topological crystalline insulators with chiral symmetry, such as the 2D SSH structure used in our work, that have a  $C_{4v}$  symmetry and those that do not have such an even-fold rotational symmetry [139, 140], such as the Kagome lattices. As demonstrated recently, even though chiral symmetry is insufficient, on its own, to stabilize corner modes against strong perturbations, the additional presence of the fourfold rotational symmetry exhibited in the 2D SSH lattices does offer topological protection and further entails the formation of the topological BICs [56, 57]. Moreover, it has been argued that the observed corner states in the breathing Kagome lattices [102, 106, 104] may not be a manifestation of the HOTI characteristics [139, 140] as they simply lack the complete symmetry protection. Such comparison and argument will stimulate further interest in topological photonics [148].

In conclusion, here we have provided the theoretical and the experimental study of the nonlinear control of topological BICs in HOTIs. Understanding the nonlinear topological phases is not only of fundamental interest but it may also be crucial for the development of photonic devices based on topological corner modes, including HOTI lasers.



# Chapter 4

## Thesis summary

The central theme of this thesis is topology. A discussion that so often starts with a joke about a donut and a coffee cup, soon turns into the discussion about one of the richest areas of physics and mathematics in modern times. It all started in the solid-state physics with the discovery of topological insulators [11, 12, 13]. The topological insulators are materials that are insulating in the bulk, but support conductive states on their boundaries. To study the properties of the topological phases of matter, a language was developed, one of Berry connections, Berry Curvatures, Berry phases, Chern numbers and others [2, 3, 4], that gives mathematical meaning to observed physical phenomena. In this context, the study of the topological phases of matter revolves around the search for symmetries that the system may possess and ways to break them. A broken symmetry leads to a topological phase transition characterized by topological invariants. Various topological invariants, such as the Chern number, the winding number or the Zak phase [4, 10, 32] are a signature of the topological properties of materials and the study of topology revolves about identifying and calculating them for a given system.

In the solid-state systems, the topology was studied in the context of the Bloch band theory. In order to move to other areas of physics, crucial was the observation that the topological band structure is a common property of waves propagating through a periodic medium [35]. A realistic proposal for a photonic crystal that supports topological states was realized soon after [37, 38]. With it, the field of topological photonics was born.

In this thesis we work with photonic lattices. Photonic lattices are obtained by sending laser light through a photorefractive crystal whose index of refraction varies periodically and enables the formation of the lattice pattern. Because they are relatively easy to work with, we use them as a tool to study topological properties of matter. This thesis is split into two parts. The first part covers our research into topological properties of matter in the momentum space and our research into how these topological properties can be mapped from the momentum space to the

real space [47]. The second part covers our research into higher order topological insulators (HOTIs) with bound states in the continuum (BICs) and our research into how the HOTIs with BICs can be controlled by nonlinearity [149].

In the first part of this thesis, we use a 2D honeycomb lattice and a 2D Lieb lattice for the study of the mapping of topological properties from the momentum space to the real space. Both of them exhibit the Bloch band structure in the momentum space. The special feature of both of these lattices is that their bands in the momentum space touch at certain points called the Dirac-like points [59, 4, 46]. The Dirac-like points are topological singularities in the momentum space. Another feature of both those lattices is that their structure can be broken down into sublattices. The honeycomb lattice has two sublattices, while the Lieb lattice has three sublattices. Because of the sublattice structure, a degree of freedom called the pseudospin emerges. The pseudospin satisfies the same algebra as the traditional electron spin. Because the honeycomb lattice has two sublattices, it is a pseudospin-1/2 system, which means that it has two pseudospin states. The Lieb lattice, with its three sublattices, is a pseudospin-1 system, with three pseudospin states. In the experiments, with a properly designed excitation of the pseudospin components in the vicinity of the Dirac-like points, we can map topological singularities from the momentum space to the real space. The experiments show us that, if we excite one of the pseudospin components, the topological charge in the other, unexcited components maps from the momentum space to the real space. The observed topological charge conversion follows the rule  $l \mapsto l + 2s$ , where  $l$  is the topological charge and  $s$  is the pseudospin. In the theoretical section, we show that there are three ways to explain the topological charge conversion, i.e. the mapping. The first way is the kinematical approach via the conservation of total angular momentum. Because the pseudospin components are excited by laser beams carrying topological charge with which orbital angular momentum can be associated, there happens a pseudospin-orbit interaction. We show that the total angular momentum is conserved and this leads us to the before-mentioned rule for the topological charge conversion. The second approach that we take to explain the mapping is one involving the dynamics of the system. We write down the Hamiltonian, find its eigenenergies and eigenstates and expand the initial excitation in the basis of these eigenstates. After a bit of math, we show that the output beam in the real space can be written in a form that contains the pseudospin eigenstates and that there is additional charge in the unexcited pseudospin component that the beam picked up because of the topological singularity in the momentum space. This approach shows us that the topological charge conversion rule involving the pseudospin holds. The third way we explain the mapping is via topology. For both lattices, we calculate a topological invariant called the Berry phase winding, denoted by  $w$ . We show that the Berry phase winding is  $w = 1$  for the honeycomb lattice and  $w = 2$  for the

Lieb lattice. This recasts the topological charge conversion rule  $l \mapsto l + 2s$  into a form that contains the Berry phase winding  $l \mapsto l \pm w$ . We also show that the Berry phase winding is equal to the maximum difference between the topological charges in the pseudospin components in the momentum space for a general Hamiltonian with any pseudospin. Crucially, we also show that there are systems where the same mapping, explained by the topological approach, and by the Berry phase winding, happens, but where the total angular momentum is not conserved or where there are no conical intersections that are a characteristic of the Dirac-like systems. Because the mapping of topological singularities is fundamentally a topological process, it makes sense to look for it in other systems with topological singularities. Consequently, we give a theoretical proposal for how to exploit this mapping in a 3D system to obtain a Weyl monopole [85] in the real space. The Weyl lattice is a 3D lattice that has a topological singularity in the momentum space and we show that, by employing our theory, it is possible to map this singularity from the momentum space to the real space and that the resulting wavefunction will have a topological charge in the real space that is identical to the charge of a synthetic Weyl monopole.

In the second part of the thesis, we study the higher order topological insulators on a photonic 2D SSH lattice. A traditional topological insulator has a bulk that is insulating, and unidirectional edge states that are conductive. In addition to the bulk states, and to the edge states, the higher order topological insulators also support topologically protected corner states [24, 25, 26, 27, 28]. The choice of a 2D SSH lattice, which is a second-order topological insulator is very much deliberate; we use it because its corner states are also the bound states in the continuum [55, 56, 57]. The BICs appear, as their name suggest, in the continuum of the bulk states in the energy spectrum and not in the band gap. Corner states that are also BICs are, then, especially interesting because they are not in the band gap, but are still topologically protected. With the topological protection, of course, come symmetries. The 2D SSH lattice possesses the chiral symmetry and the rotational symmetry. To test the topological properties, we aim to break those symmetries, and the way to do it is by using nonlinearity. The experiment is performed on a 2D SSH lattice that is realized in a photorefractive crystal. Initially, we excite one corner of the lattice. A probe beam locally changes the index structure of the lattice which gives rise to the nonlinearity. Because the corner states of the 2D SSH lattice are BICs, one could expect that they would couple to the bulk states during the propagation of the beam. But, contrary to this expectation, we show, in the experiment, and in the numerical simulations that the corner states couple to the edge states, and not the bulk states. This coupling happens for both the self-focusing and the self-defocusing nonlinearity. To explain this phenomena, we perform a theoretical analysis in the continuous and the discrete 2D SSH model. In the continuous model, the beam propagation method (BPM) is used to simulate the propagation of the laser

beam by numerically solving the nonlinear Schrödinger equation. By using this model, we are able to show the periodic beating between the corner states and the edge states, and that there is no coupling with the bulk states. The discrete model relies on the tight-binding approximation (TBA), where the intracell coupling  $t$  and intercell coupling  $t'$  model the strength of the bonds between neighboring lattice sites. A dimerization parameter  $c = t - t'$  is introduced. For  $c < 0$ , the lattice is topologically nontrivial and it exhibits the corner modes and the edge modes. For  $c > 0$  it is trivial. Both the linear and nonlinear eigenvalues are calculated in the discrete model. Using the discrete model, we show that the corner modes couple to the edge modes under the action of both the focusing and the defocusing nonlinearity in the topologically nontrivial,  $c < 0$ , regime. The nonlinear corner states are, strictly speaking, no longer stationary BICs as in the linear regime. But crucially, they do undergo periodic coupling with the edge states and not the bulk states. This indicates that they have inherited the topological nature of the corner modes in the linear regime. To characterize the topological properties, we calculate the polarization of the system, which is related to a topological invariant; the Zak phase [32]. In the linear system, and in the topologically trivial case, where  $c > 0$ , the polarization is  $P_x = P_y = 0$ . In the nontrivial,  $c < 0$ , case, the polarization is  $P_x = P_y = 1/2$ , i.e. there is a sudden jump in polarization because of the topological phase transition. For the nonlinear system, we calculate the polarization in the TBA approximation and show that it can be controlled by the strength of the nonlinearity. We also show that the sudden jump in polarization persists, i.e. that it is inherited from the linear system, which confirms the earlier statement that the topological properties of the nonlinear system are inherited from the linear system.

This work on the mapping of topological properties of photonic lattices has both fundamental and practical significance. The momentum to real space mapping of topological singularities broadens our fundamental understanding of topological processes, while the nonlinear control of HOTIs that are also BICs opens up some interesting avenues for potential applications via the coupling of topological corner and edge states.

# Poglavlje 5

## Prošireni sažetak

**Ključne riječi:** *topologija, topološka fotonika, fotoničke rešetke, topološki izolatori, topološki izolatori višeg reda, vezana stanja u kontinuumu, Berryjeva faza, Zakova faza, namotaji Berryjeve faze, Chernov broj, polarizacija, Diracove točke, pseudospin, nelinearnost*

### 5.1 Uvod

Jedna od najvažnijih zadaća fizike je proučavati agregatnih stanja materije. Kod istraživanja stanja materije, iliti faza materije, često nas ne zanimaju detalji sustava kojeg proučavamo, već njegova globalna svojstva. Grana fizike koja se bavi proučavanjem globalnih svojstava objekata zove se *topologija*. Topologiju se može vrlo jednostavno objasniti na primjeru šalice i krafne. Šalicu možemo kontinuirano deformirati u krafnu. Točno jedna rupa koju imaju i šalice i krafna je *topološko svojstvo* koje je očuvano tijekom *kontinuirane deformacije* šalice u krafnu. Dakle, šalice i krafna imaju istu *topologiju*.

Istraživanje topoloških faza materije počelo je u fizici čvrstog stanja otkrićem cjelobrojnog kvantnog Hallovog efekta [11, 12]. Eksperimenti se provode u *realnom prostoru*, a topološka svojstva proučavaju se u *impulsnom prostoru* pa je potencijalno vrlo zanimljivo proučavati realni i impulsni prostor i vezu među njima u kontekstu topologije. Fizika čvrstog stanja najčešće se bavi periodičkim sustavima. Kod periodičkih sustava, energetski spektar u impulsnom prostoru ima strukturu Blochovih vrpca [1]. Naravno, topologiju ne moramo nužno proučavati u čvrsto-stanjskim sustavima. Haldane i Raghupathy pokazali su da je struktura Blochovih vrpca zajednička svim periodičkim sustavima [35] i to je otvorilo put prema istraživanju topologije u periodičkim *fotoničkim sustavima* [37, 38, 39, 40, 41]. Mi ovdje proučavamo topološka svojstva u *fotoničkim rešetkama*.

### 5.1.1 Topološka fotonika

Kada laserska svjetlost prođe kroz 3D fotorefraktivni kristal, na izlazu dobijemo zraku koja se propagira u jednom dobro definiranom smjeru, koji označimo sa  $z$ , i koja tvori uzorak rešetke u  $x - y$  ravnini okomitoj na smjer propagacije. Topološka fotonika počiva na činjenici da je ponašanje laserske svjetlosti opisano paraksijalnom valnom jednačjom [42, 43, 44, 45]:

$$i \frac{\partial \Psi(x, y, z)}{\partial z} = -\frac{1}{2k_0} \nabla^2 \Psi(x, y, z) - \frac{k_0 \Delta n(x, y)}{n_0} \Psi(x, y, z) = H \Psi(x, y, z), \quad (5.1)$$

koja ima isti oblika kao i Schrödingerova jednačba. U tom slučaju,  $z$  koordinata igra ulogu vremena, a  $x$  i  $y$  su prostorne koordinate.  $k_0$  je valni vektor,  $n_0$  je indeks loma pozadinskog medija, a  $\Delta n(x, y)$  je inducirani indeks loma koji formira rešetku u  $x - y$  ravnini. Hamiltonijan  $H$  u jedn. (5.1), najčešće je efektivni hamiltonijan koji opisuje fotoničku rešetku koju proučavamo i koji dobijemo Fourierovim transformatom u impulsni prostor. Budući da su fotoničke rešetke periodičke, energijski spektar ima strukturu Blochovih vrpca u impulsnom prostoru. Između Blochovih vrpca može, ali i ne mora, postojati energijski procjep. Ta dva slučaja; sa i bez procjepa, odgovaraju dvjema različitim topološkim fazama. Ako energijski procjep postoji, sustav je izolator, a ako je razmak zatvoren, sustav podržava vodljiva stanja. Najzanimljiviji su sustavi koji imaju obje faze. Takvi sustavi zovu se *topološki izolatori* [14]. Topološki izolatori su izolatori u svojoj unutrašnjosti, ali imaju vodljiva stanja na svojim rubovima. Postojanje izolatora u unutrašnjosti i vodljivih rubnih stanja implicira da se energijski procjep negdje zatvorio i da su se pojavila vodljiva stanja koja imaju energije unutar energijskog procjepa. Topološka svojstva takvih sustava u impulsnom prostoru proučavamo koristeći alate poput *Berryjeve veze*, *Berryjeve zakrivljenosti*, *Berryjeve faze* [2, 3], *Chernovog broja* [4] i sličnih topoloških invarijanti. Topološke invarijante, poput Chernovog broja, korisne su za klasifikaciju materijala na topološki trivijalne, tj. one koji nemaju topološki zaštićene faze poput rubnih stanja, i na topološki netrivialne, tj. one koji imaju topološki zaštićena stanja. Npr, topološke izolatore moguće je opisati korespondencijom između unutrašnjosti i granice. Ako unutrašnji dio s obje strane granice ima dva različita Chernova broja, tj. ako je slomljena simetrija prostorne inverzije, sustav je topološki netrivialan. Chernov broj računa se u impulsnom prostoru:

$$C_n = \frac{1}{2\pi} \oint_{\partial S} \mathcal{A}_n(\mathbf{k}) \cdot d\mathbf{k} = \frac{1}{2\pi} (\gamma - \gamma'), \quad (5.2)$$

preko integrala Berryjeve veze  $\mathcal{A}_n(\mathbf{k}) = i \langle u_{n,\mathbf{k}} | \nabla_{\mathbf{k}} | u_{n,\mathbf{k}} \rangle$ , po rubu Brillouinove zone  $\partial S$ , koja se dobije iz Blochovih stanja  $|u_{n,\mathbf{k}}\rangle$ , gdje  $n$  označava Blochovu vrpcu. Chernov broj povezan je s razlikom Berryjevih faza  $\gamma - \gamma'$  s obje strane granice. Budući da je da je ta razlika faza cjelobro-

jni umnožak od  $2\pi$ , Chernov broj je cijeli broj. Chernov broj je, slavno, povezan s vodljivošću u cjelobrojnom kvantnom Hallovom efektu [13]. Dakle, topologija u impulsnom prostoru ima opazive posljedice u realnom prostoru.

U prvom dijelu ovog rada proučavamo topološka svojstva 2D ftoničkih grafenskih i Liebovih rešetki koje imaju *topološke singularitete* u impulsnom prostoru. Ti singulariteti mogu se preslikati iz impulsnog u realni prostor. To preslikavanje moguće je objasniti očuvanjem ukupnog angularnog momenta, dugodosežnom dinamičkom propagacijom i namotajima Berryjeve faze. Od ta tri pristupa, fundamentalan je topološki, s namotajima Berryjeve faze.

Osim tradicionalnih topoloških izolatora, koji imaju *unutrašnja stanja* i *rubna stanja*, zanimaju nas i izolatori višeg reda (HOTI) i njima se bavimo u drugom dijelu ovog rada. HOTI, osim unutrašnjih i rubnih stanja imaju i topološka *kutna stanja* [24, 27, 28, 26]. Sustav s kojim radimo je ftonička 2D SSH rešetka čija su kutna stanja također i vezana stanja u kontinuumu (BIC) unutrašnjih stanja. Kada u sustavu uključimo nelinearnost, moglo bi se očekivati da će se pomiješati unutrašnja stanja i kutna stanja, koja su u kontinuumu unutrašnjih stanja, jer imaju slične energije. Međutim, u ovom radu pokazano je da se kutna stanja vežu s rubnim stanjima, a ne s unutrašnjim stanjima; i za samo-fokusirajuću i za samo-defokusirajuću nelinearnost. Također, izračunata je i polarizacija sustava koja je povezana s topološkom invarijantom sustava koja se zove Zakova faza i pokazano je da je polarizaciju moguće kontrolirati pomoću nelinearnosti.

## 5.2 Preslikavanje topoloških singulariteta iz impulsnog u realni prostor

Rad predstavljen u ovom odjeljku objavljen je u:

- X. Liu, S. Xia, E. Jajtić, D. Song, D. Li, L. Tang, D. Leykam, J. Xu, H. Buljan & Z. Chen, Universal momentum-to-real-space mapping of topological singularities. *Nat Commun* **11**, 1586 (2020).

### 5.2.1 Topološki singulariteti u ftoničkim rešetkama

Da bismo pokazali preslikavanje topoloških svojstava, koristimo ftoničku grafensku [45, 58] i Liebovu rešetku [46]. Grafenska rešetka oblika je heksagonalne rešetke i može se podijeliti na dvije trokutaste podrešetke [42, 74]. Liebova rešetka je kvadratna rešetka s tri podrešetke. Njihova podstruktura ima važne implikacije za njihova fizikalna i topološka svojstva. Naime,

grafensku rešetku opisuje  $2 \times 2$  hamiltonijan jer ona ima dvije podrešetke. Slično tome, hamiltonijan Liebove rešetke je  $3 \times 3$  jer ona ima tri podrešetke. U oba slučaja, hamiltonijan ima oblik  $H = \kappa \mathbf{S} \cdot \mathbf{k}$ , gdje  $\kappa$  ovisi o detaljima rešetke,  $\mathbf{k}$  je kristalni impuls, a  $\mathbf{S}$  je stupanj slobode koji se zove *pseudospin* i koji se pojavi zbog podstrukture rešetke [45]. Pseudospin zadovoljava algebru tradicionalnog spina. U slučaju grafenske rešetke, pseudospin su  $2 \times 2$  matrice koje odgovaraju Paulijevim matricama pa onda fotonička grafenska rešetka ima pseudospin  $1/2$ . U slučaju Liebove rešetke, matrice pseudospina su  $3 \times 3$  matrice pa Liebova rešetka ima pseudospin 1. Kod obje rešetke, energijski spektar ima Blochove vrpce u impulsnom prostoru; grafenska ima dvije, a Liebova tri. U oba slučaja, vrpce se dotiču u točkama koje se zovu Diracove točke. Diracove točke su topološki singulariteti u impulsnom prostoru [59, 4].

Da bismo ostvarili preslikavanje tih topoloških singulariteta iz impulsnog u realni prostor, koristimo se sljedećom idejom: Laserskom zrakom, koja je optički vrtlog i koja nosi *topološki naboj*  $l$ , pobudimo podrešetku čije svojstveno stanje ima topološki naboj 0, i onda na izlazu detektiramo koliki je topološki naboj nakon propagacije zrake. U slučaju fotoničke grafenske rešetke, na izlazu dobijemo topološki naboj 2, a u slučaju Liebove rešetke, na izlazu dobijemo topološki naboj 3. Dakle, došlo je do konverzije topološkog naboja prema pravilu:

$$l \mapsto l + 2s, \quad (5.3)$$

gdje je  $l$  topološki naboj, a  $s$  pseudospin odgovarajuće fotoničke rešetke. Tu konverziju možemo objasniti na tri načina; kinematikom, dugodosežnom dinamikom i topologijom.

## 5.2.2 Kinematika i dinamika preslikavanja topoloških naboja iz impulsnog u realni prostor

Kinematičko objašnjenje preslikavanja počiva na očuvanju ukupnog angularnog momenta. Budući da hamiltonijan ima oblik  $H = \kappa \mathbf{S} \cdot \mathbf{k}$ , za očekivati je da će u sustavu biti pseudospin-orbit interakcije pa onda ima i smisla pogledati što se događa s ukupnim angularnim momentom. U ovom radu, pokazano je da  $[H, J_z] = 0$ , tj. da hamiltonijan komutira sa z-komponentom ukupnog angularnog momenta  $\mathbf{J} = \mathbf{L} + \mathbf{S}$ . Budući da se sva dinamika odvija u z-smjeru, to znači da je ukupni angularni moment očuvan i da vrijedi relacija  $l + s = l' + s'$ , gdje su  $l$  i  $s$  orbitalni angularni moment, koji odgovara topološko naboju, i pseudospin komponente koja je pobuđena na ulazu, a  $l'$  i  $s'$  su orbitalni angularni moment i pseudospin na izlazu. S time možemo izračunati topološki naboj na izlazu  $l'$  za obje rešetke. Npr. za fotoničku grafensku rešetku pokazano je u odjeljku 2.3 da, ako na ulazu imamo  $l = 1$  i pobudimo  $s = 1/2$ , na izlazu dobijemo tu istu komponentu pseudospina, ali i komponentu koju nismo pobudili sa  $s' = -1/2$  i  $l' = 2$  što se slaže s pravilom

iz jedn. (5.3). Slično je i za Liebovu rešetku gdje, nakon pobude komponente  $s = 1$  s  $l = 1$ , na izlazu imamo i komponentu sa  $s' = -1$  i  $l' = 3$ , što se slaže s istim pravilom. Kinematika nam objašnjava što se u sustavu događa; pobudimo jednu od komponenti pseudospina, a onda se topološki naboj iz druge, nepobuđene komponente, preslika iz impulsnog u realni prostor. Dinamika će nam reći kako se to dogodi.

Ideja iza dinamičkog objašnjenja je sljedeća: Riješimo paraksijalnu valnu jednadžbu (5.1) tako da uzmemo početno pobuđenje, razvijemo ga u bazi svojstvenih stanja odgovarajuće rešetke i evoluiramo s propagacijskim konstantama koje su svojstvene energije hamiltonijana. Početno pobuđenje opisano je valnom funkcijom koja, u impulsnom prostoru, ima oblik vrtloga s topološkim nabojem  $l$ . Svojstveno stanje koje pobudimo ima topološki naboj 0. Međutim, osim tog jednog, pobuđenog, u impulsnom prostoru postoji još svojstvenih stanja s topološkim nabojima  $l \neq 0$  koja nismo pobudili i koja također imaju oblik vrtloga zbog Diracove točke koja je topološki singularitet u impulsnom prostoru. U odjeljku 2.4 pokazano je da se, tijekom propagacije, ti topološki naboji u nepobuđenim komponentama preslikaju iz impulsnog prostora u realni prostor i da vrijedi pravilo (5.3).

### 5.2.3 Topologija preslikavanja singulariteta iz impulsnog u realni prostor

Da bismo dobili fundamentalnu sliku preslikavanja singulariteta iz impulsnog prostora u realni prostor, moramo proučiti topologiju sustava. U impulsnom prostoru, i grafenska i Liebova rešetka imaju Diracove točke koje su topološki singulariteti. Je li topologija trivijalna ili netrivijalna u blizini Diracove točke, reći će nam topološke invarijante, ako postoje, naravno. Da bismo otkrili postoje li, računamo Berryjevu fazu oko Diracove točke. U odjeljku 2.5 pokazano je da je Berryjeva faza jednaka  $w\pi$ , gdje je  $w = 1$  za grafensku rešetku i  $w = 2$  za Liebovu rešetku.  $w$  je topološka invarijanta koja se zove *namotaji Berryjeve faze* i netrivijalna je i za grafensku i za Liebovu rešetku. Također, pokazano je da su namotaji Berryjeve faze jednaki maksimalnoj razlici topoloških nabojâ u komponentama pseudospina u impulsnom prostoru. Dakle, preslikavanje topološkog singulariteta iz impulsnog prostora možemo, umjesto pravilom (5.3) opisati pravilom:

$$l \mapsto l \pm w. \quad (5.4)$$

Osim toga, pokazano je i da postoje sustavi u kojim pravilo (5.3) sa pseudospinom ne vrijedi, ali preslikavanje topoloških singulariteta se i dalje događa po pravilu (5.4). Jedan od takvih sustava su rastegnute rešetke. U rastegnutim rešetkama ukupni angularni moment nije očuvan pa pravilo sa pseudospinom ne vrijedi, ali preslikavanje se i dalje događa i prati pravilo s namota-

jima Berryjeve faze. Idući primjer su hamiltonijani slični hamiltonijanu koji opisuje grafensku i Liebovu rešetku, ali čije energije nemaju stožast oblik u blizini Diracove točke. Kod njih ukupni angularni moment također nije očuvan, ali vrtlozi kod svojstvenih stanja u impulsnom prostoru su slični vrtlozima kod grafenskih i Liebovih rešetki, samo s multiplicitetom  $m$ . U tom slučaju, preslikavanje se i dalje događa i prati pravilo (5.4) s namotajima Berryjeve faze s  $w = m$ . Još jedan primjer je hamiltonijan oblika  $H = k\sigma_z$ , gdje svojstvena stanja jesu spinori i u sustavu ima pseudospina, ali nema preslikavanja topoloških singulariteta iz impulsnog u realni prostor jer hamiltonijan komutira sa  $\sigma_z$  pa onda ni nema transfera energije između komponenti pseudospina. U tom slučaju i dalje vrijedi pravilo (5.4) jer su namotaji Berryjeve faze  $w = 0$ . Dakle, fundamentalna slika preslikavanja topoloških singulariteta iz impulsnog u realni prostor je topološka i karakterizirana je namotajima Berryjeve faze.

Razvijena teorija vrijedi općenito za sve hamiltonijane oblika  $H = \mathbf{S} \cdot \mathbf{k}$ , a ne nužno samo za 2D sustave. Zbog toga možemo dati prijedlog za 3D sustav. Weylov hamiltonijan  $H = \sigma_x k_x + \sigma_y k_y + \sigma_z k_z$  realiziran je eksperimentalno u čvrstostanjskim i optičkim sustavima [48, 49] i ima sintetički magnetski monopol u impulsnom prostoru [85]. Koristeći našu teoriju, u principu je moguće preslikati taj monopol iz impulsnog u realni prostor.

## 5.3 Nelinearni topološki izolatori višeg reda

Rad predstavljen u ovom odjeljku objavljen je u:

- Z. Hu, D. Bongiovanni, D. Jukić, E. Jajtić, S. Xia, D. Song, J. Xu, R. Morandotti, H. Buljan & Z. Chen, Nonlinear control of photonic higher-order topological bound states in the continuum. *Light Sci Appl* **10**, 164 (2021).

### 5.3.1 Topološki izolatori višeg reda

Tradicionalni topološki izolatori imaju unutrašnjost koja je izolator i vodljiva rubna stanja koja su topološki zaštićena. Kod njih, lokalizirana topološka stanja imaju dimenziju za 1 manju od unutrašnjih stanja pa za te izolatore kažemo da su *topološki izolatori prvog reda*. Općenito, moguće je da topološki izolatori imaju topološki zaštićena lokalizirana stanja čija je dimenzija različita od dimenzije unutrašnjosti za 2 ili više. Takve izolatore zovemo *topološkim izolatorima višeg reda*. Na primjer, 2D topološki izolator, koji ima unutrašnjost koja je 2-dimenzionalna, i rubna stanja, koja su 1-dimenzionalna, može imati i kutna stanja, koja su 0-dimenzionalna [4, 116]. Topološki izolatori višeg reda ostvareni su u raznim čvrstostanjskim, elektroničkim akustičkim i ftoničkim sustavima [94, 95, 96, 97, 98].

Kod topoloških izolatora, lokalizirana topološka stanja uglavnom se nalaze u energijskom procjepu između Blochovih vrpca. Međutim, kod topoloških izolatora višeg reda mogu se pojaviti i vezana topološka stanja čije se energije nalaze u kontinuumu energija unutrašnjih stanja [55, 56, 57]. Jedan od primjera topoloških izolatora višeg reda s *vezanim stanjima u kontinuumu* je 2D SSH rešetka. 2D SSH rešetka je kvadratna rešetka koja ima dvije, općenito različite, jakosti veza među prvim susjednim atomima: *Unutar-ćelijsko* vezanje koju označavamo s  $t$ , i *među-ćelijsko* vezanje označavamo s  $t'$ . Korisno je uvesti *dimerizacijski parametar*  $c = t - t'$ . Za  $c < 0$ , rešetka je u topološki netrivialnoj fazi, a za  $c > 0$  je u topološki trivialnoj fazi. 2D SSH rešetka, osim izolatorskih unutrašnjih stanja, ima i lokalizirana rubna i kutna stanja. Ta stanja topološki su zaštićena kiralnom i  $C_{4v}$  rotacijskom simetrijom. Da bismo inducirali topološke fazne prijelaze, moramo te simetrije slomiti. Jedan od načina na koje ih možemo slomiti je pomoću nelinearnosti [126, 127, 128]. Budući da su kutna stanja 2D SSH rešetke u kontinuumu unutrašnjih stanja, za očekivati je da će se kutna stanja vezati na unutrašnja stanja pod utjecajem nelinearnosti. Međutim, u ovom radu pokazano je da se kutna stanja vežu na rubna stanja, a ne na unutrašnja stanja, i za samo-fokusirajuću i za samo-defokusirajuću nelinearnost. Eksperiment kojim je to pokazano napravljen je na fotoničkoj 2D SSH rešetci, a teorija koja opisuje vezanje napravljena je za kontinuirani i diskretni 2D SSH model.

### 5.3.2 Fotonička 2D SSH rešetka

2D fotoničku rešetku dobijemo propagacijom laserske svjetlosti kroz nelinearni fotorefraktivni kristal [142]. Propagacija svjetlosti u tom je slučaju opisana kontinuiranom nelinearnom Schrödingerovom jednačbom [80] koju je za diskretni 2D SSH model moguće aproksimirati s:

$$i \frac{\partial \psi_\alpha}{\partial Z} + \sum_{\alpha'} [H_L]_{\alpha, \alpha'} \psi_{\alpha'} + E'_0 \frac{\gamma |\psi_\alpha|^2}{1 + \gamma |\psi_\alpha|^2} \psi_\alpha = 0, \quad (5.5)$$

gdje je  $\psi_\alpha$  kompleksna amplituda električnog polja na poziciji  $\alpha$  u rešetci,  $[H_L]_{\alpha, \alpha'}$  je matrični element linearnog hamiltonijana  $H_L$  2D SSH modela,  $E'_0$  je pozadinsko električno polje, a  $\gamma$  je jakost nelinearnosti. Za  $\gamma > 0$ , nelinearnost je samodefokusirajuća, a za  $\gamma < 0$ , nelinearnost je samofokusirajuća. Koristeći hamiltonijan koji odgovara diskretnoj jedn. (5.5), možemo naći spektar svojstvenih energija 2D SSH rešetke i onda raditi simulacije propagacije laserske svjetlosti kroz rešetku. U linearnom slučaju, u spektru imamo unutrašnja stanja koja tvore vrpce, rubna stanja u energijskom procjepu i kutna stanja koja su vezana stanja u kontinuumu unutrašnjih stanja. Kada uključimo nelinearnost,  $\gamma \neq 0$ , i pobudimo jedan od kuteva rešetke,

kutna stanja se pomaknu u energijski procjep i vežu se na rubna stanja. Vežanje na rubna stanja, a ne na unutrašnja stanja dogodi se i za samo-fokusirajuću i za samo-defokusirajuću nelinearnost. Činjenica da se topološka kutna stanja vežu na topološka rubna stanja, a ne na unutrašnja stanja, govori nam da nelinearni topološki izolatori višeg reda nasljeđuju topološka svojstva od linearnog sistema. Osim same činjenice da se kutna stanja vežu na rubna stanja, tijekom propagacije možemo vidjeti i da se događaju oscilacije između kutnih i rubnih stanja, bez radijacije u unutrašnjost izolatora.

Osim simulacija u diskretnom modelu, možemo raditi i simulacije s kontinuiranim modelom, BPM metodom. BPM metoda svodi se na numeričko rješavanje nelinearne Schrödingerove jednadžbe. Za početnu pobudu izabrana je laserka zraka gausijanskog profila i pobuđen je jedan kut rešetke. Nakon dugodosežne propagacije, vidimo da dolazi do oscilacija između kutnih stanja i rubnih stanja, bez radijacije u unutrašnjost; isto kao i u diskretnom modelu.

### 5.3.3 Nelinearna kontrola topoloških izolatora višeg reda

Vežanje topoloških kutnih i rubnih stanja u 2D SSH rešetci pokazano je i eksperimentalno u odjeljku 3.4. Fotonička rešetka napravljena je upisivanjem valovoda u nelinearni fotorefraktivni kristal SBN:61 dugačak 20 mm. Početna pobuda je zraka gausijanskog profila i pobuđen je jedan kut rešetke. Ideja je vidjeti kako se sutav ponaša za različite snage i predznake nelinearnosti  $\gamma$ . U slučaju slabe samo-fokusirajuće i samo-defokusirajuće nelinearnosti, kutna stanja vežu se na rubna stanja. Ako je samo-fokusirajuća nelinearnost jaka, dolazi do pojave jako lokaliziranih kutnih solitona. Ako je pak samo-defokusirajuća nelinearnost jaka, zbog jake deformacije rešetke, dolazi do radijacije kutnih stanja i u rub i u unutrašnjost. Iz tih rezultata vidljivo je da je sistem moguće kontrolirati snagom nelinearnosti i da nelinearni sistem nasljeđuje topološka svojstva linearnog sistema.

Da bismo opažene pojave stavili u kontekst topologije, računamo topološke invarijante sistema. Za 2D SSH rešetku, relevantna topološka invarijanta je *polarizacija*  $P_i$ ,  $i = x, y$  koja je povezana sa Zakovom fazom  $Z_i = 2\pi P_i$ . Polarizacija je dana integralom Berryjeve konekcije:

$$P_i = -\frac{1}{(2\pi)^2} \iint dk_x dk_y \text{Tr}[A_i(k_x, k_y)], \quad (5.6)$$

gdje je  $(A_i)_{mn}(\mathbf{k}) = i\langle u_m(\mathbf{k}) | \partial_{k_i} | u_n(\mathbf{k}) \rangle$ , a  $u_m(\mathbf{k})$  je svojstveno stanje  $m$ -te energijske vrpce. Polarizacija linearnog sistema je  $P_x = P_y = 1/2$  za  $c < 0$ , tj. kada je dimerizacijski parametar manji od 0, sistem je u *topološki netrivialnoj fazi*. U slučaju  $c > 0$ , polarizacija je  $P_x = P_y = 0$ , tj. sistem je u *topološki trivialnoj fazi*. Kada je nelinearnost  $\gamma \neq 0$ , isti račun moguće je ponoviti numerički. Nelinearnost slomi simetriju koja je odgovorna za zaštitu dvaju različitih

topoloških faza. Međutim, mi možemo iskoristiti polarizaciju da pokažemo da nelinearni sustav nasljeđuje topološka svojstva od linearnog sistema. Naime, kada izračunamo i nacrtamo polarizaciju u nelinearnom režimu kao funkciju nelinearnosti  $\gamma$  i dimerizacijskog parametra  $c$ , vidimo da se ona samo malo mijenja u odnosu na vrijednosti polarizacije u linearnom sustavu, gdje je  $P_x = P_y = 1/2$  za  $c < 0$  i  $P_x = P_y = 0$  za  $c > 0$ . Također, pokazali smo da ta devijacija, za slabu nelinearnost raste linearno s porastom nelinearnosti  $\gamma$ . Dakle, ako zamislimo nelinearnost kao malu perturbaciju linearnog sistema, nagli skok polarizacije s 0 na  $1/2$  kod  $c = 0$  bit će, kod nelinearnog sistema, naslijeđen od linearnog sistema. Drugim riječima; nelinearni sustav, u kojem su simetrije slomljene, naslijedi topološka svojstva od linearnog sustava ako je nelinearnost slaba, tj. ako je nelinearnost mala perturbacija, unatoč tome što su simetrije slomljene.

## 5.4 Zaključak

U ovom radu proučavamo topološka svojstva fotoničkih rešetki. U prvom dijelu bavimo se preslikavanjem topoloških singulariteta iz impulsnog u realni prostor. U drugom dijelu, bavimo se nelinearnim topološkim izolatorima višeg reda i nasljeđivanjem topoloških svojstava od linearnog sistema.

Preslikavanje topoloških singulariteta iz impulsnog u realni prostor demonstriramo u 2D fotoničkim grafenskim i Liebovim rešetkama. U energijskom spektru u impulsnom prostoru, obje rešetke imaju strukturu Blochovih vrpce koje se dotiču u Diracovim točkama. Diracove točke su singulariteti u impulsnom prostoru. Pobuđivanjem modova u blizini Diracove točke pokazali smo da se topološki singularitet preslika iz impulsnog u realni prostor. Taj fenomen možemo objasniti na tri načina. Prvi način je kinematički, pomoću očuvanja orbitalnog angularnog momenta. Naime, hamiltonijan za obje rešetke ima oblik  $H = \kappa \mathbf{S} \cdot \mathbf{k}$  što sugerira da je moguća pseudospin-orbit interakcija. Taj hamiltonijan komutira s operatorom ukupnog angularnog momenta pa je ukupni angularnim moment očuvan. To nam omogućuje da izračunamo topološki naboj na izlazu iz poznatih vrijednosti pseudospina i topološkog naboja na ulazu. Rezultat je konzistentan s preslikavanjem topološkog naboja iz impulsnog u realni prostor. Drugi način objašnjenja preslikavanja je pomoću dinamičke propagacije početnog pobuđenja. Početno pobuđenje razvijemo u bazi svojstvenih stanja hamiltonijana i evoluiramo ga s propagacijskim konstantama koje su svojstvene energije hamiltonijana. Rezultat je moguće raspisati po komponentama pseudospina koje u impulsnom prostoru imaju različite topološke naboje koji se preslikaju iz impulsnog prostora u realni prostor tijekom propagacije. Treći način objašnjenja preslikavanja je pomoću topologije. Za obje rešetke izračunali smo Berryjevu fazu i dobili smo da je jednaka  $w\pi$ , gdje su namotaji Berryjeve faze  $w = 1$  za grafensku rešetku i  $w = 2$

za Liebovu rešetku. Pokazali smo i da su namotaji Berryjeve faze jednaki maksimalnoj razlici topoloških naboja u komponentama pseudospina u impulsnom prostoru. Također, pokazali smo da postoje sustavi, poput rastegnutih rešetki, u kojima ukupni angularni moment nije očuvan, kao i sustavi u kojima objašnjenje sa pseudospinom ne funkcionira, ali u kojima se preslikavanje i dalje događa i može se objasniti topologijom. Dakle, topološka slika preslikavanja je fundamentalna i vrijedi za općenito za sustave koji imaju topološke singularitete u impulsnom prostoru. To nam je omogućilo da damo prijedlog za preslikavanje 3D Weylovog sintetičkog monopola iz impulsnog u realni prostor.

Nelinearnu kontrolu topoloških izolatora višeg reda demonstrirali smo na 2D fotoničkoj SSH rešetci. 2D SSH rešetka ima unutrašnjost koja je izolator, topološka rubna stanja i topološka kutna stanja koja su vezana stanja u kontinuumu unutrašnjih stanja. Budući da se kutna stanja nalaze u kontinuumu unutrašnjih stanja, za očekivati je da će se pod utjecajem nelinearnosti kutna stanja vezati na unutrašnja stanja. Međutim, demonstrirali smo da se, za slabu nelinearnost, kutna stanja vežu na rubna stanja, a ne na unutrašnja stanja. To sugerira da je nelinearni sustav naslijedio topološka svojstva od linearnog sistema. Eksperiment je proveden u fotoničkoj 2D SSH rešetci i pokazao je da se kutna stanja uistinu vežu na rubna stanja u slučaju slabe nelinearnosti. To je potvrđeno i numeričkim simulacijama. Osim samog vezanja, demonstrirali smo i da postoje oscilacije između kutnih i rubnih stanja tijekom propagacije laserske svjetlosti kroz rešetku. Topologija koja je u pozadini nelinearne kontrole topoloških izolatora višeg reda otkrivena je računanjem polarizacije sistema. Naime, kod topoloških izolatora drugog reda, poput 2D SSH rešetke, polarizacija je topološka invarijanta povezana sa Zakovom fazom. 2D SSH rešetka ima dvije topološke faze koje su karakterizirane dimerizacijskim parametrom  $c$ .  $c < 0$  odgovara topološki netrivialnoj fazi i polarizaciji  $P_x = P_y = 1/2$ , dok  $c > 0$  odgovara topološki trivialnoj fazi s polarizacijom  $P_x = P_y = 0$ . Računanjem polarizacije za nelinearni sistem, pokazali samo da i dalje postoji oštri skok u polarizaciji oko  $c = 0$  i da je devijacija od linearnog slučaja mala za slabu nelinearnost i da raste linearno sa snagom nelinearnosti. Drugim riječima, ako zamislimo nelinearnost kao malu perturbaciju linearnog sistema, nagli skok u polarizaciji onda je nasljeđe linearnog sistema.

Ukratko, u ovom radu istraživali smo preslikavanja topoloških svojstava fotoničkih rešetki. Preslikavanje topoloških singulariteta iz impulsnog u realni prostor od fundamentalne je važnosti za razumijevanje topologije, dok je nelinearna kontrola topoloških izolatora višeg reda zanimljiva za potencijalne primjene kod koji je važna mogućnost vezanja raznih topološki zaštićenih vodljivih stanja.

# Bibliography

- [1] Neil W Ashcroft, N David Mermin, et al. *Solid state physics*. 1976.
- [2] Michael Victor Berry. “Quantal phase factors accompanying adiabatic changes”. *Proceedings of the Royal Society of London. A. Mathematical and Physical Sciences* 392.1802 (1984), pp. 45–57.
- [3] S. Pancharatnam. “Generalized theory of interference, and its applications”. *Proceedings of the Indian Academy of Sciences - Section A* 44.5 (1956), pp. 247–262.
- [4] Tomoki Ozawa et al. “Topological photonics”. *Rev. Mod. Phys.* 91 (1 2019), p. 015006.
- [5] Jean Dalibard et al. “Colloquium: Artificial gauge potentials for neutral atoms”. *Rev. Mod. Phys.* 83 (4 2011), pp. 1523–1543.
- [6] Mahito Kohmoto. “Topological invariant and the quantization of the Hall conductance”. *Annals of Physics* 160.2 (1985), pp. 343–354.
- [7] J. E. Avron, R. Seiler, and B. Simon. “Homotopy and Quantization in Condensed Matter Physics”. *Phys. Rev. Lett.* 51 (1 1983), pp. 51–53.
- [8] Qian Niu, D. J. Thouless, and Yong-Shi Wu. “Quantized Hall conductance as a topological invariant”. *Phys. Rev. B* 31 (6 1985), pp. 3372–3377.
- [9] M. A. Armstrong. *Basic Topology*. Springer New York, 1983.
- [10] Joseph P.S. Kung and Chung-Chun Yang. “Complex Analysis”. *Encyclopedia of Physical Science and Technology (Third Edition)*. Ed. by Robert A. Meyers. Third Edition. New York: Academic Press, 2003, pp. 443–454.
- [11] K. v. Klitzing, G. Dorda, and M. Pepper. “New Method for High-Accuracy Determination of the Fine-Structure Constant Based on Quantized Hall Resistance”. *Phys. Rev. Lett.* 45 (6 1980), pp. 494–497.
- [12] Klaus von Klitzing. “The quantized Hall effect”. *Rev. Mod. Phys.* 58 (3 1986), pp. 519–531.
- [13] D. J. Thouless et al. “Quantized Hall Conductance in a Two-Dimensional Periodic Potential”. *Phys. Rev. Lett.* 49 (6 1982), pp. 405–408.
- [14] Mordechai Segev and Miguel A. Bandres. “Topological photonics: Where do we go from here?” *Nanophotonics* 10.1 (2021), pp. 425–434.
- [15] R. Jackiw and C. Rebbi. “Solitons with fermion number  $\frac{1}{2}$ ”. *Phys. Rev. D* 13 (12 1976), pp. 3398–3409.

- [16] Xiao-Liang Qi, Yong-Shi Wu, and Shou-Cheng Zhang. “Topological quantization of the spin Hall effect in two-dimensional paramagnetic semiconductors”. *Phys. Rev. B* 74 (8 2006), p. 085308.
- [17] B. I. Halperin. “Quantized Hall conductance, current-carrying edge states, and the existence of extended states in a two-dimensional disordered potential”. *Phys. Rev. B* 25 (4 1982), pp. 2185–2190.
- [18] A. H. MacDonald. “Quantized Hall effect and edge currents”. *Phys. Rev. B* 29 (4 1984), pp. 1616–1619.
- [19] M. Büttiker. “Absence of backscattering in the quantum Hall effect in multiprobe conductors”. *Phys. Rev. B* 38 (14 1988), pp. 9375–9389.
- [20] C. L. Kane and E. J. Mele. “Quantum Spin Hall Effect in Graphene”. *Phys. Rev. Lett.* 95 (22 2005), p. 226801.
- [21] B. Andrei Bernevig, Taylor L. Hughes, and Shou-Cheng Zhang. “Quantum Spin Hall Effect and Topological Phase Transition in HgTe Quantum Wells”. *Science* 314.5806 (4 2006), pp. 1757–1761.
- [22] M. Z. Hasan and C. L. Kane. “Colloquium: Topological insulators”. *Rev. Mod. Phys.* 82 (4 2010), pp. 3045–3067.
- [23] Xiao-Liang Qi and Shou-Cheng Zhang. “Topological insulators and superconductors”. *Rev. Mod. Phys.* 83 (4 2011), pp. 1057–1110.
- [24] Wladimir A. Benalcazar, B. Andrei Bernevig, and Taylor L. Hughes. “Quantized electric multipole insulators”. *Science* 357.6346 (4 2017), pp. 61–66.
- [25] N. R. Cooper, J. Dalibard, and I. B. Spielman. “Topological bands for ultracold atoms”. *Rev. Mod. Phys.* 91 (1 2019), p. 015005.
- [26] Wladimir A. Benalcazar, B. Andrei Bernevig, and Taylor L. Hughes. “Electric multipole moments, topological multipole moment pumping, and chiral hinge states in crystalline insulators”. *Phys. Rev. B* 96 (24 2017), p. 245115.
- [27] Josias Langbehn et al. “Reflection-Symmetric Second-Order Topological Insulators and Superconductors”. *Phys. Rev. Lett.* 119 (24 2017), p. 246401.
- [28] Frank Schindler et al. “Higher-order topological insulators”. *Science Advances* 4.6 (4 2018), eaat0346.
- [29] Marc Serra-Garcia et al. “Observation of a phononic quadrupole topological insulator”. *Nature* 555.7696 (4 2018), pp. 342–345.
- [30] Christopher W. Peterson et al. “A quantized microwave quadrupole insulator with topologically protected corner states”. *Nature* 555.7696 (4 2018), pp. 346–350.
- [31] Stefan Imhof et al. “Topoelectrical-circuit realization of topological corner modes”. *Nature Physics* 14.9 (4 2018), pp. 925–929.
- [32] Raffaele Resta. “Macroscopic polarization in crystalline dielectrics: the geometric phase approach”. *Reviews of Modern Physics* 66.3 (4 1994), pp. 899–915.

- [33] Bi-Ye Xie et al. “Second-order photonic topological insulator with corner states”. *Phys. Rev. B* 98 (20 2018), p. 205147.
- [34] Feng Liu and Katsunori Wakabayashi. “Novel Topological Phase with a Zero Berry Curvature”. *Phys. Rev. Lett.* 118 (7 2017), p. 076803.
- [35] F. D. M. Haldane and S. Raghu. “Possible Realization of Directional Optical Waveguides in Photonic Crystals with Broken Time-Reversal Symmetry”. *Phys. Rev. Lett.* 100 (1 2008), p. 013904.
- [36] S. Raghu and F. D. M. Haldane. “Analogues of quantum-Hall-effect edge states in photonic crystals”. *Phys. Rev. A* 78 (3 2008), p. 033834.
- [37] Zheng Wang et al. “Reflection-Free One-Way Edge Modes in a Gyromagnetic Photonic Crystal”. *Phys. Rev. Lett.* 100 (1 2008), p. 013905.
- [38] Zheng Wang et al. “Observation of unidirectional backscattering-immune topological electromagnetic states”. *Nature* 461.7265 (4 2009), pp. 772–775.
- [39] Mohammad Hafezi et al. “Robust optical delay lines with topological protection”. *Nature Physics* 7.11 (4 2011), pp. 907–912.
- [40] And I. Carusotto. “Artificial gauge field for photons in coupled cavity arrays”. *Phys. Rev. A* 84 (4 2011), p. 043804.
- [41] Alexander B. Khanikaev et al. “Photonic topological insulators”. *Nature Materials* 12.3 (4 2013), pp. 233–239.
- [42] Or Peleg et al. “Conical Diffraction and Gap Solitons in Honeycomb Photonic Lattices”. *Phys. Rev. Lett.* 98 (10 2007), p. 103901.
- [43] Alexander Szameit and Stefan Nolte. “Discrete optics in femtosecond-laser-written photonic structures”. *Journal of Physics B: Atomic, Molecular and Optical Physics* 43.16 (4 2010), p. 163001.
- [44] Mikael C. Rechtsman et al. “Photonic Floquet topological insulators”. *Nature* 496.7444 (4 2013), pp. 196–200.
- [45] Daohong Song et al. “Unveiling pseudospin and angular momentum in photonic graphene”. *Nature Communications* 6.1 (4 2015), p. 6272.
- [46] Falko Diebel et al. “Conical Diffraction and Composite Lieb Bosons in Photonic Lattices”. *Phys. Rev. Lett.* 116 (18 2016), p. 183902.
- [47] Xiuying Liu et al. “Universal momentum-to-real-space mapping of topological singularities”. *Nature Communications* 11.1 (4 2020), p. 1586.
- [48] Ling Lu et al. “Experimental observation of Weyl points”. *Science* 349.6248 (4 2015), pp. 622–624.
- [49] Su-Yang Xu et al. “Discovery of a Weyl fermion semimetal and topological Fermi arcs”. *Science* 349.6248 (4 2015), pp. 613–617.
- [50] B. Q. Lv et al. “Experimental Discovery of Weyl Semimetal TaAs”. *Phys. Rev. X* 5 (3 2015), p. 031013.

- [51] W. P. Su, J. R. Schrieffer, and A. J. Heeger. “Solitons in Polyacetylene”. *Phys. Rev. Lett.* 42 (25 1979), pp. 1698–1701.
- [52] S. Barišić, J. Labbé, and J. Friedel. “Tight Binding and Transition-Metal Superconductivity”. *Physical Review Letters* 25.14 (4 1970), pp. 919–922.
- [53] S. Barišić. “Rigid-Atom Electron-Phonon Coupling in the Tight-Binding Approximation.I”. *Physical Review B* 5.3 (4 1972), pp. 932–941.
- [54] S. Barišić. “Self-Consistent Electron-Phonon Coupling in the Tight-Binding Approximation. II”. *Physical Review B* 5.3 (4 1972), pp. 941–951.
- [55] Ze-Guo Chen et al. “Corner states in a second-order acoustic topological insulator as bound states in the continuum”. *Phys. Rev. B* 100 (7 2019), p. 075120.
- [56] Wladimir A. Benalcazar and Alexander Cerjan. “Bound states in the continuum of higher-order topological insulators”. *Phys. Rev. B* 101 (16 2020), p. 161116.
- [57] Alexander Cerjan et al. “Observation of a Higher-Order Topological Bound State in the Continuum”. *Phys. Rev. Lett.* 125 (21 2020), p. 213901.
- [58] Jian-Long Liu, Wei-Min Ye, and Shuang Zhang. “Pseudospin-induced chirality with staggered optical graphene”. *Light: Science & Applications* 5.8 (4 2016), e16094–e16094.
- [59] P. R. Wallace. “The Band Theory of Graphite”. *Phys. Rev.* 71 (9 1947), pp. 622–634.
- [60] K.Y. Bliokh et al. “Theory and applications of free-electron vortex states”. *Physics Reports* 690 (4 2017). Theory and applications of free-electron vortex states, pp. 1–70.
- [61] K. Y. Bliokh et al. “Spin–orbit interactions of light”. *Nature Photonics* 9.12 (4 2015), pp. 796–808.
- [62] Gabriel Biener et al. “Formation of helical beams by use of Pancharatnam–Berry phase optical elements”. *Opt. Lett.* 27.21 (4 2002), pp. 1875–1877.
- [63] L. Marrucci, C. Manzo, and D. Paparo. “Optical Spin-to-Orbital Angular Momentum Conversion in Inhomogeneous Anisotropic Media”. *Phys. Rev. Lett.* 96 (16 2006), p. 163905.
- [64] Ebrahim Karimi et al. “Generating optical orbital angular momentum at visible wavelengths using a plasmonic metasurface”. *Light: Science & Applications* 3.5 (4 2014), e167–e167.
- [65] Konstantin Y. Bliokh et al. “Geometrodynamics of spinning light”. *Nature Photonics* 2.12 (4 2008), pp. 748–753.
- [66] Shubo Wang, Guancong Ma, and Che Ting Chan. “Topological transport of sound mediated by spin-redirection geometric phase”. *Science Advances* 4.2 (4 2018), eaaq1475.
- [67] Konstantin Y. Bliokh, Daria Smirnova, and Franco Nori. “Quantum spin Hall effect of light”. *Science* 348.6242 (4 2015), pp. 1448–1451.
- [68] Matthew Mecklenburg and B. C. Regan. “Spin and the Honeycomb Lattice: Lessons from Graphene”. *Phys. Rev. Lett.* 106 (11 2011), p. 116803.
- [69] Xiaodong Xu et al. “Spin and pseudospins in layered transition metal dichalcogenides”. *Nature Physics* 10.5 (4 2014), pp. 343–350.

- [70] Zhaoyang Zhang et al. “Particlelike Behavior of Topological Defects in Linear Wave Packets in Photonic Graphene”. *Phys. Rev. Lett.* 122 (23 2019), p. 233905.
- [71] K. S. Novoselov et al. “Two-dimensional gas of massless Dirac fermions in graphene”. *Nature* 438.7065 (4 2005), pp. 197–200.
- [72] Yuanbo Zhang et al. “Experimental observation of the quantum Hall effect and Berry’s phase in graphene”. *Nature* 438.7065 (4 2005), pp. 201–204.
- [73] A. H. Castro Neto et al. “The electronic properties of graphene”. *Rev. Mod. Phys.* 81 (1 2009), pp. 109–162.
- [74] Antonino Flachi and Vincenzo Vitagliano. “Symmetry breaking and lattice kirigami: Finite temperature effects”. *Phys. Rev. D* 99 (12 2019), p. 125010.
- [75] Mikhail I. Katsnelson. *Graphene: Carbon in Two Dimensions*. Vol. 84. Cambridge University Press, 2012, p. 043804.
- [76] L. Duca et al. “An Aharonov-Bohm interferometer for determining Bloch band topology”. *Science* 347.6219 (4 2015), pp. 288–292.
- [77] L. Allen et al. “Orbital angular momentum of light and the transformation of Laguerre-Gaussian laser modes”. *Phys. Rev. A* 45 (11 1992), pp. 8185–8189.
- [78] Daniel Leykam, Omri Bahat-Treidel, and Anton S. Desyatnikov. “Pseudospin and non-linear conical diffraction in Lieb lattices”. *Phys. Rev. A* 86 (3 2012), p. 031805.
- [79] Shiqiang Xia et al. “Demonstration of flat-band image transmission in optically induced Lieb photonic lattices”. *Opt. Lett.* 41.7 (4 2016), pp. 1435–1438.
- [80] Nikos K. Efremidis et al. “Discrete solitons in photorefractive optically induced photonic lattices”. *Phys. Rev. E* 66 (4 2002), p. 046602.
- [81] I.V. Basistiy et al. “Optics of light beams with screw dislocations”. *Optics Communications* 103.5 (4 1993), pp. 422–428.
- [82] Vitor M. Pereira, A. H. Castro Neto, and N. M. R. Peres. “Tight-binding approach to uniaxial strain in graphene”. *Phys. Rev. B* 80 (4 2009), p. 045401.
- [83] Mikael C. Rechtsman et al. “Strain-induced pseudomagnetic field and photonic Landau levels in dielectric structures”. *Nature Photonics* 7.2 (4 2013), pp. 153–158.
- [84] M. Milićević et al. “Type-III and Tilted Dirac Cones Emerging from Flat Bands in Photonic Orbital Graphene”. *Physical Review X* 9.3 (4 2019), p. 031010.
- [85] Tena Dubček et al. “Weyl Points in Three-Dimensional Optical Lattices: Synthetic Magnetic Monopoles in Momentum Space”. *Physical Review Letters* 114.22 (4 2015), p. 225301.
- [86] Armand Béché et al. “Magnetic monopole field exposed by electrons”. *Nature Physics* 10.1 (4 2014), pp. 26–29.
- [87] A. E. Leanhardt et al. “Imprinting Vortices in a Bose-Einstein Condensate using Topological Phases”. *Phys. Rev. Lett.* 89 (19 2002), p. 190403.

- [88] Todd Van Mechelen and Zubin Jacob. “Photonic Dirac monopoles and skyrmions: spin-1 quantization”. *Opt. Mater. Express* 9.1 (4 2019), pp. 95–111.
- [89] Mark R. Dennis et al. “Isolated optical vortex knots”. *Nature Physics* 6.2 (4 2010), pp. 118–121.
- [90] Emilio Pisanty et al. “Knotting fractional-order knots with the polarization state of light”. *Nature Photonics* 13.8 (4 2019), pp. 569–574.
- [91] Qinghui Yan et al. “Experimental discovery of nodal chains”. *Nature Physics* 14.5 (4 2018), pp. 461–464.
- [92] Qian Lin et al. “Photonic Weyl point in a two-dimensional resonator lattice with a synthetic frequency dimension”. *Nature Communications* 7.1 (4 2016), p. 13731.
- [93] Eran Lustig et al. “Photonic topological insulator in synthetic dimensions”. *Nature* 567.7748 (4 2019), pp. 356–360.
- [94] M. Hafezi et al. “Imaging topological edge states in silicon photonics”. *Nature Photonics* 7.12 (4 2013), pp. 1001–1005.
- [95] Josias Langbehn et al. “Reflection-Symmetric Second-Order Topological Insulators and Superconductors”. *Phys. Rev. Lett.* 119 (24 2017), p. 246401.
- [96] Marc Serra-Garcia et al. “Observation of a phononic quadrupole topological insulator”. *Nature* 555.7696 (4 2018), pp. 342–345.
- [97] Christopher W. Peterson et al. “A quantized microwave quadrupole insulator with topologically protected corner states”. *Nature* 555.7696 (4 2018), pp. 346–350.
- [98] Stefan Imhof et al. “Topoelectrical-circuit realization of topological corner modes”. *Nature Physics* 14.9 (4 2018), pp. 925–929.
- [99] Jiho Noh et al. “Topological protection of photonic mid-gap defect modes”. *Nature Photonics* 12.7 (4 2018), pp. 408–415.
- [100] Xiao-Dong Chen et al. “Direct Observation of Corner States in Second-Order Topological Photonic Crystal Slabs”. *Phys. Rev. Lett.* 122 (23 2019), p. 233902.
- [101] Bi-Ye Xie et al. “Visualization of Higher-Order Topological Insulating Phases in Two-Dimensional Dielectric Photonic Crystals”. *Phys. Rev. Lett.* 122 (23 2019), p. 233903.
- [102] Ashraf El Hassan et al. “Corner states of light in photonic waveguides”. *Nature Photonics* 13.10 (4 2019), pp. 697–700.
- [103] Sunil Mittal et al. “Photonic quadrupole topological phases”. *Nature Photonics* 13.10 (4 2019), pp. 692–696.
- [104] Haoran Xue et al. “Acoustic higher-order topological insulator on a kagome lattice”. *Nature Materials* 18.2 (4 2019), pp. 108–112.
- [105] Ha-Reem Kim et al. “Multipolar lasing modes from topological corner states”. *Nature Communications* 11.1 (4 2020), p. 5758.
- [106] Xiang Ni et al. “Observation of higher-order topological acoustic states protected by generalized chiral symmetry”. *Nature Materials* 18.2 (4 2019), pp. 113–120.

- [107] Tao Liu et al. “Second-Order Topological Phases in Non-Hermitian Systems”. *Phys. Rev. Lett.* 122 (7 2019), p. 076801.
- [108] Shuo Liu et al. “Octupole corner state in a three-dimensional topological circuit”. *Light: Science & Applications* 9.1 (4 2020), p. 145.
- [109] Avik Dutt et al. “Higher-order topological insulators in synthetic dimensions”. *Light: Science & Applications* 9.1 (4 2020), p. 131.
- [110] Bing Liu et al. “Higher-Order Band Topology in Twisted Moiré Superlattice”. *Phys. Rev. Lett.* 126 (6 2021), p. 066401.
- [111] Yang Liu et al. “Bulk–disclination correspondence in topological crystalline insulators”. *Nature* 589.7842 (4 2021), pp. 381–385.
- [112] Chen-Hsuan Hsu et al. “Majorana Kramers Pairs in Higher-Order Topological Insulators”. *Phys. Rev. Lett.* 121 (19 2018), p. 196801.
- [113] Tudor E. Pahomi, Manfred Sigrist, and Alexey A. Soluyanov. “Braiding Majorana corner modes in a second-order topological superconductor”. *Phys. Rev. Research* 2 (3 2020), p. 032068.
- [114] Yasutomo Ota et al. “Photonic crystal nanocavity based on a topological corner state”. *Optica* 6.6 (4 2019), pp. 786–789.
- [115] Weixuan Zhang et al. “Low-threshold topological nanolasers based on the second-order corner state”. *Light: Science & Applications* 9.1 (4 2020), p. 109.
- [116] Minkyung Kim and Junsuk Rho. “Topological edge and corner states in a two-dimensional photonic Su-Schrieffer-Heeger lattice”. *Nanophotonics* 9.10 (4 2020), pp. 3227–3234.
- [117] Daria Smirnova et al. “Nonlinear topological photonics”. *Applied Physics Reviews* 7.2 (4 2020), p. 021306.
- [118] Yaakov Lumer et al. “Self-Localized States in Photonic Topological Insulators”. *Phys. Rev. Lett.* 111 (24 2013), p. 243905.
- [119] Daniel Leykam and Y. D. Chong. “Edge Solitons in Nonlinear-Photonic Topological Insulators”. *Phys. Rev. Lett.* 117 (14 2016), p. 143901.
- [120] Yakir Hadad, Alexander B. Khanikaev, and Andrea Alù. “Self-induced topological transitions and edge states supported by nonlinear staggered potentials”. *Phys. Rev. B* 93 (15 2016), p. 155112.
- [121] Sergey Kruk et al. “Nonlinear light generation in topological nanostructures”. *Nature Nanotechnology* 14.2 (4 2019), pp. 126–130.
- [122] Shiqi Xia et al. “Nontrivial coupling of light into a defect: the interplay of nonlinearity and topology”. *Light: Science & Applications* 9.1 (4 2020), p. 147.
- [123] Lukas J. Maczewsky et al. “Nonlinearity-induced photonic topological insulator”. *Science* 370.6517 (4 2020), pp. 701–704.
- [124] Shiqi Xia et al. “Nonlinear tuning of PT symmetry and non-Hermitian topological states”. *Science* 372.6537 (4 2021), pp. 72–76.

- [125] Seababrat Mukherjee and Mikael C. Rechtsman. “Observation of Floquet solitons in a topological bandgap”. *Science* 368.6493 (4 2020), pp. 856–859.
- [126] R. Banerjee, S. Mandal, and T. C. H. Liew. “Coupling between Exciton-Polariton Corner Modes through Edge States”. *Phys. Rev. Lett.* 124 (6 2020), p. 063901.
- [127] R. Banerjee, S. Mandal, and T. C. H. Liew. “Coupling between Exciton-Polariton Corner Modes through Edge States”. *Phys. Rev. Lett.* 124 (6 2020), p. 063901.
- [128] Yiqi Zhang et al. “Nonlinear higher-order polariton topological insulator”. *Opt. Lett.* 45.17 (4 2020), pp. 4710–4713.
- [129] M. S. Kirsch et al. “Observation of nonlinear corner states in a higher-order photonic topological insulator”. *Conference on Lasers and Electro-Optics*. Vol. 84. Optica Publishing Group, 2021, FTh4H.2.
- [130] Zhichan Hu et al. “Nonlinearity-induced transition of topological corner states”. *Conference on Lasers and Electro-Optics*. Vol. 84. Optica Publishing Group, 2021, FTh4H.4.
- [131] Sergey S. Kruk et al. “Nonlinear Imaging of Nanoscale Topological Corner States”. *Nano Letters* 21.11 (4 2021). PMID: 34008406, pp. 4592–4597.
- [132] Bo Zhen et al. “Topological Nature of Optical Bound States in the Continuum”. *Phys. Rev. Lett.* 113 (25 2014), p. 257401.
- [133] Chia Wei Hsu et al. “Bound states in the continuum”. *Nature Reviews Materials* 1.9 (4 2016), p. 16048.
- [134] Kirill Koshelev et al. “Nonradiating photonics with resonant dielectric nanostructures”. *Nanophotonics* 8.5 (4 2019), pp. 725–745.
- [135] Yonatan Plotnik et al. “Experimental Observation of Optical Bound States in the Continuum”. *Phys. Rev. Lett.* 107 (18 2011), p. 183901.
- [136] Chia Wei Hsu et al. “Observation of trapped light within the radiation continuum”. *Nature* 499.7457 (4 2013), pp. 188–191.
- [137] Mengyao Li et al. “Higher-order topological states in photonic kagome crystals with long-range interactions”. *Nature Photonics* 14.2 (4 2020), pp. 89–94.
- [138] Marco S. Kirsch et al. “Nonlinear second-order photonic topological insulators”. *Nature Physics* 17.9 (4 2021), pp. 995–1000.
- [139] Guido van Miert and Carmine Ortix. “On the topological immunity of corner states in two-dimensional crystalline insulators”. *npj Quantum Materials* 5.1 (4 2020), p. 63.
- [140] Minwoo Jung, Yang Yu, and Gennady Shvets. “Exact higher-order bulk-boundary correspondence of corner-localized states”. *Phys. Rev. B* 104 (19 2021), p. 195437.
- [141] Xiaosheng Wang et al. “Observation of Two-Dimensional Surface Solitons”. *Phys. Rev. Lett.* 98 (12 2007), p. 123903.
- [142] Shiqi Xia et al. “Unconventional Flatband Line States in Photonic Lieb Lattices”. *Phys. Rev. Lett.* 121 (26 2018), p. 263902.

- 
- [143] R.R. Monchamp, G.B. Mihalik, and L.A. Franks. “Octagonal crystals of strontium barium niobate (SBN: 61)”. *Journal of Crystal Growth* 140.3 (4 1994), pp. 439–440.
- [144] Natalia Malkova et al. “Observation of optical Shockley-like surface states in photonic superlattices”. *Opt. Lett.* 34.11 (4 2009), pp. 1633–1635.
- [145] Ming feng Shih et al. “Waveguides induced by photorefractive screening solitons”. *J. Opt. Soc. Am. B* 14.11 (4 1997), pp. 3091–3101.
- [146] A. Szameit et al. “Observation of Two-Dimensional Surface Solitons in Asymmetric Waveguide Arrays”. *Phys. Rev. Lett.* 98 (17 2007), p. 173903.
- [147] Daichi Obana, Feng Liu, and Katsunori Wakabayashi. “Topological edge states in the Su-Schrieffer-Heeger model”. *Phys. Rev. B* 100 (7 2019), p. 075437.
- [148] Zhigang Chen and Mordechai Segev. “Highlighting photonics: looking into the next decade”. *eLight* 1.1 (4 2021), p. 2.
- [149] Zhichan Hu et al. “Nonlinear control of photonic higher-order topological bound states in the continuum”. *Light: Science & Applications* 10.1 (4 2021), p. 164.



# Supervisor information

Prof. **Hrvoje Buljan** is a full professor of physics at the University of Zagreb, Croatia, and a visiting professor at Nankai University, China. He defended his doctoral thesis at the University of Zagreb in 2002. After he spent two years as a postdoctoral fellow at the Technion, Israel, he was appointed as faculty at the University of Zagreb. He is a theoretical physicist with interests in optics and photonics (nonlinear and topological photonics, graphene nanophotonics) and ultracold atomic gases (interacting quantum systems). He published 83 papers in refereed journals and has 5100 citations in Google Scholar. He received the Annual Croatian State Award for Science in 2010, and Andrija Mohorovičić award as an outstanding scientists and teacher at the University of Zagreb in 2019. He mentored 5 PhD thesis and more than 30 diploma thesis. Hrvoje Buljan served as a Chairman of the Department of Physics (2014-2016), and as Vice Dean for Science (2016-2018) at the Faculty of Science, University of Zagreb. He leads the Center of Excellence for Quantum and Complex Systems in Zagreb (2015-2025), which involves 80 theoretical physicists and mathematicians and receives funding from the European Union.



# Curriculum vitae

**Emma Jajtić** was born on 4 July 1993 in Zabok, Croatia. In 2018, she obtained her master's degree in physics from the Faculty of Science, University of Zagreb, Croatia. From 2018 until date, she has stayed as a research and a teaching assistant at the Department of Physics in the group of prof. Hrvoje Buljan. Her main interests and the area of research are topology and photonics, and she has co-authored 2 papers published in Nature Research journals. She participated in 2 international conferences; TPB 2019 in Tianjin, China and CLEO 2020 in San Jose, USA. In 2020, she received the 'Successful young scientist award' from the Faculty of Science, University of Zagreb.



# List of publications

- X. Liu, S. Xia, E. Jajtić, D. Song, D. Li, L. Tang, D. Leykam, J. Xu, H. Buljan & Z. Chen, Universal momentum-to-real-space mapping of topological singularities. *Nat Commun* **11**, 1586 (2020).
- Z. Hu, D. Bongiovanni, D. Jukić, E. Jajtić, S. Xia, D. Song, J. Xu, R. Morandotti, H. Buljan & Z. Chen Nonlinear control of photonic higher-order topological bound states in the continuum. *Light Sci Appl* **10**, 164 (2021).